Economic Geology, v. 102, pp. 1233–1267

Multistage Sedimentary and Metamorphic Origin of Pyrite and Gold in the Giant Sukhoi Log Deposit, Lena Gold Province, Russia

Ross R. Large,†

CODES, ARC Centre of Excellence in Ore Deposits, University of Tasmania, Private Bag 79, Hobart, Tasmania, Australia 7001

Valeriy V. Maslennikov,

Institute of Mineralogy, Russian Academy of Science, Urals Branch, Miass, Russia

François Robert,

Barrick Gold Corporation, 161 Bay St., P.O. Box 212, Toronto, Canada M5J 2S1

Leonid V. Danyushevsky, and Zhaoshan Chang

CODES, ARC Centre of Excellence in Ore Deposits, University of Tasmania, Private Bag 79, Hobart, Tasmania, Australia 7001

Abstract

Gold mineralization at Sukhoi Log in eastern Siberia is hosted in a deformed Neoproterozoic organic-bearing and pyritic black shale and siltstone sequence that is folded into a tight overturned anticline. The deposit contains about 30 million ounces of gold at an average grade of 2.0 g/t Au and is one of the largest known undeveloped gold resources. The high-grade gold zone forms a gently dipping tabular body in the core of the anticline. The best gold grades occur in narrow, bedding-parallel pyrite-quartz veinlets that have been folded during the main deformation event. Lower grade gold is associated with disseminated pyrite developed in and around the high-grade core of the deposit.

Detailed paragenetic studies of the mineralization and host rocks have defined six stages of pyrite development in the carbonaceous sediments. The two earliest forms of pyrite, termed py_1 and py_2, are commonly developed in stratiform layers of micron-sized crystals, framboids and fine euhedra, which are interpreted as synsedimentary to early diagenetic in origin. Coarser grained, bedding-parallel aggregates of inclusion-rich pyrite, termed py_3, contain inclusions of arsenopyrite, native gold and gold tellurides and are interpreted to form during late diagenesis and earliest deformation. Coarse euhedral pyrite, py_4, overgrows the earlier pyrite (py_1, py_2, and py_3), and the slaty cleavage developed in the host rocks, indicating a syndeformation timing. Late-stage, inclusion-free pyrite, py_5, overgrows and replaces earlier sulfides and is considered to be syn- to late deformation.

Laser-ablation inductively coupled plasma mass spectrometry (LA-ICPMS) analyses of the various pyrite types indicate that the synsedimentary py_1 contains the highest levels of invisible gold, varying from 0.4 to 12.1 ppm, with a mean of 3.22 ppm Au, and 1,900 ppm As. Py_1 is also enriched in a suite of trace elements (Mo, Sb, Ni, Co, Se, Te, Ag, Cu, Pb, Zn, Mn, Ba, Cr, U, V), which are similar to those concentrated by organic processes in euxinic sedimentary environments. Later generations of pyrite, from py_2 to py_5, including pyrite in bedding-parallel pyrite-quartz veinlets, contain progressively lower contents of invisible gold and most other trace elements. However, this metamorphic and postmetamorphic pyrite contains microinclusions of free gold, arsenopyrite, pyrrhotite, sphalerite, and chalcopyrite. The paragenetic, textural, and chemical relationships at Sukhoi Log suggest that gold was clearly initially introduced prior to cleavage development, accompanying sedimentation of the organic-rich shales and fixed during diagenesis within the structure of diagenetic arsenian pyrite. Subsequently, accompanying deformation, gold was liberated from recrystallized diagenetic pyrite to become concentrated as free gold and gold tellurides within metamorphic pyrite and folded bedding-parallel pyrite-quartz veinlets.

Two key processes are considered vital to the formation of the Sukhoi Log deposit: original synsedimentary and early diagenetic concentration of gold, dissolved within arsenian pyrite in organic-rich black shales, and metamorphic processes that liberated gold from the early forms of arsenian pyrite, to be concentrated as free gold, and gold tellurides within late diagenetic and metamorphic pyrite and associated pyrite-quartz veinlets in the core of an overturned anticline. These ore-forming processes are unlikely to be unique to Sukhoi Log; other black-shale and turbidite-hosted deposits that occur in rifted continental margin environments, which have undergone collision and basin inversion, may form by similar processes.

Introduction

Sukhoi Log is a world-class sediment-hosted gold deposit, containing over 30 million ounces (Moz) of gold at an average grade of 2 to 2.5 g/t Au (Distler et al., 2004; Wood and Popov, 2006). The deposit is located in the Lena gold province, a major alluvial gold district, on the eastern margin of the Siberian craton, 850 km northeast of Irkutsk (Fig. 1), which has yielded over 1,000 metric tons (t) of gold from placers since 1846 (Benevolskiy, 2002). The main deposit, which does not crop out, was discovered in the early 1960s by drilling

† Corresponding author: e-mail, Ross.Large@utas.edu.au

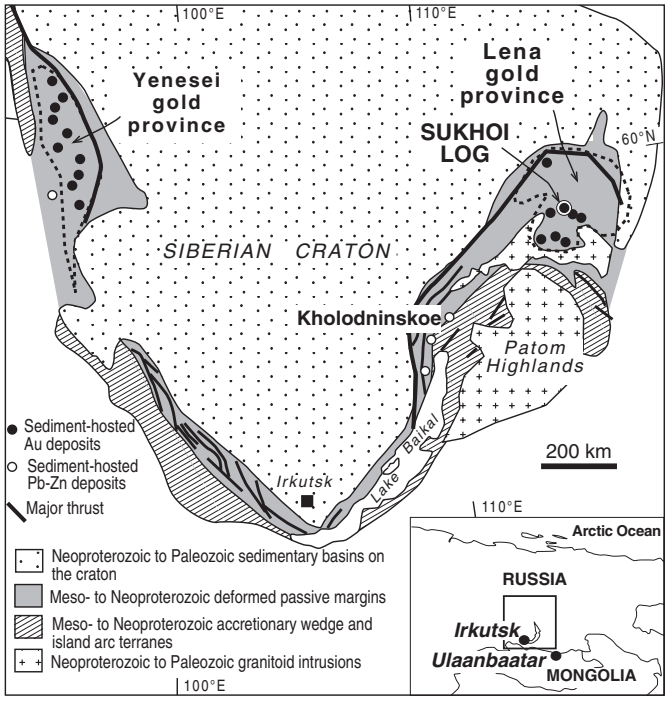

FIG. 1. Setting of Sukhoi Log and the Lena gold province on the eastern margin of the Siberian craton (after Buryak and Khmelevskaya, 1997; Yakubchuk et al., 2005).

below minor surface quartz veins to intersect disseminated pyrite-gold mineralization in black shales at depth (Buryak, 1964,1967; Buryak and Khmelevskaya, 1997). Drilling through the 1970s delineated the large disseminated pyrite-gold resource (Yakubchuk et al., 2005). The Sukhoi Log deposit remains undeveloped, although a small open-cut mine, Zapadnoe, at the western end of the main deposit, commenced operations in 2005.

The Sukhoi Log deposit consists of disseminated pyrite and bedding-parallel pyrite-quartz veinlets with minor crosscutting quartz veins, hosted in Neoproterozoic black carbonaceous shales and siltstones within the axial zone of an inclined, tight to near-isoclinal anticline. There has been considerable debate about the origin and timing of gold mineralization at Sukhoi Log (Yakubuchuk et al., 2005). Buryak (1982) and Buryak and Khemelevskaia (1997) proposed that gold was initially introduced by sedimentary exhalative processes and concentrated in arsenic-bearing pyrite within the fine-grained Neoproterozoic carbonaceous sediments. During subsequent metamorphism, gold was mobilized from the arsenian pyrite in the sedimentary rocks, concentrated by metamorphic fluids, and deposited in anticlinal structural traps (Buryak, 1982). Distler et al. (2004) undertook mineralogical, fluid inclusion, and isotopic research and combined this with regional geophysical analysis to conclude that granites, which intruded over the period from 460 to 320 Ma, were the source of the gold in Sukhoi Log. Other workers (e.g., Goldfarb et al., 2001) group Sukhoi Log into the class of orogenic gold deposits and consider that the gold was introduced from a deep source during orogenesis, and deposited in favorable structural sites within organic-rich trap rocks.

In this paper we present data on the textures, paragenesis, and trace element geochemistry of the various stages of pyrite and veining within the deposit, supported by detailed underground observations made by one of us in 1998 when the Number 2 drive was rehabilitated for due diligence purposes (F. Robert, unpub. report for Barrick Gold Corp., 1998, 24 p.). We conclude that the results support an early introduction of gold prior to folding of the host rocks, and possibly during sedimentation and diagenesis, followed by pyrite recrystallization and gold redistribution during deformation and metamorphism, similar to that proposed by Buryak (1982). Various platinum group minerals have been reported from Sukhoi Log (e.g., Distler et al., 2004), however no attempt was made in this study to verify their presence, and no PGE were detected during our LA-ICPMS study of the sulfides.

Regional Geologic Setting

The Lena gold province occurs within the Patom Highlands orogen (Fig. 1), a deformed Neoproterozoic passive margin sequence that accumulated as a 15- to 20-km-thick clastic-carbonate sequence on the southern margin of the Siberian craton (Distler et al., 2004; Yakubchuk et al., 2005). In addition to gold deposits, the passive margin sequence contains SEDEX-style base metal deposits in the southwest portion of the Patom Highlands (e.g., Kholodniskoe; Smirnov, 1997) and Ni-PGE mineralization in the Dovyren ultramafic complex (Konnikov, 1986). Kholodniskoe is a strata-bound Zn-Pb-Ag deposit hosted in Neoproterozoic garnet-quartz-biotite-muscovite schists and marbles about 500 km southwest of Sukhoi Log (Fig. 1; Distanov et al., 1982).

Sukhoi Log occurs in a complexly folded clastic-carbonate succession of Proterozoic age that comprises the Bodaibo trough (Kuz'min et al., 2006), surrounded on three sides by flat-lying Paleozoic and younger cover of the Siberian platform (Figs. 1, 2; Wood and Popov, 2006). The Neoproterozoic Patom Group is the principal sequence in the Bodaibo trough, representing continental margin shelf, slope, and basinal facies (Kazakevich, 1971). The Patom Group is comprised of three subgroups (Wood and Popov, 2006): (1) the lower Ballaganakh Subgroup (1,500–2,800 m) consists of a sandstone-shale sequence overlain by a thick limestone sequence; (2) the middle Kadalikan Subgroup (900–1500 m) consists of black shales, siltstones, and sandstones overlain by limestones and dolomites containing algal remains; and (3) the upper Bodaibo Subgroup (>2,200 m) is dominated by fine clastic, calcareous, and carbonaceous shales. Sukhoi Log is hosted by the Khomolkho Formation (Fig. 3), a 400- to 800-m-thick unit of carbonaceous shales, siltstones, and minor sandstones, in the middle Kadalikan Subgroup, (Distler, et al., 2004; Wood and Popov, 2006). Sukhoi Log occurs in a tight anticline of the Khomolkho Formation developed on the southern limb of a regional anticline (Fig. 3). Vysochaisky, which consists of disseminated pyrite-gold mineralization similar to that at Sukhoi Log (Buryak and Khemelevskaia, 1997), occurs in the Khomolkho Formation on the northern limb of the regional anticline (Fig. 3).

Buryak (1982) and Yakubchuk et al. (2005) define three main styles of sediment-hosted gold mineralization in the Lena gold province; Au-bearing quartz veins, disseminated Au sulfide (pyrite), and disseminated Au pyrrhotite. Sukhoi

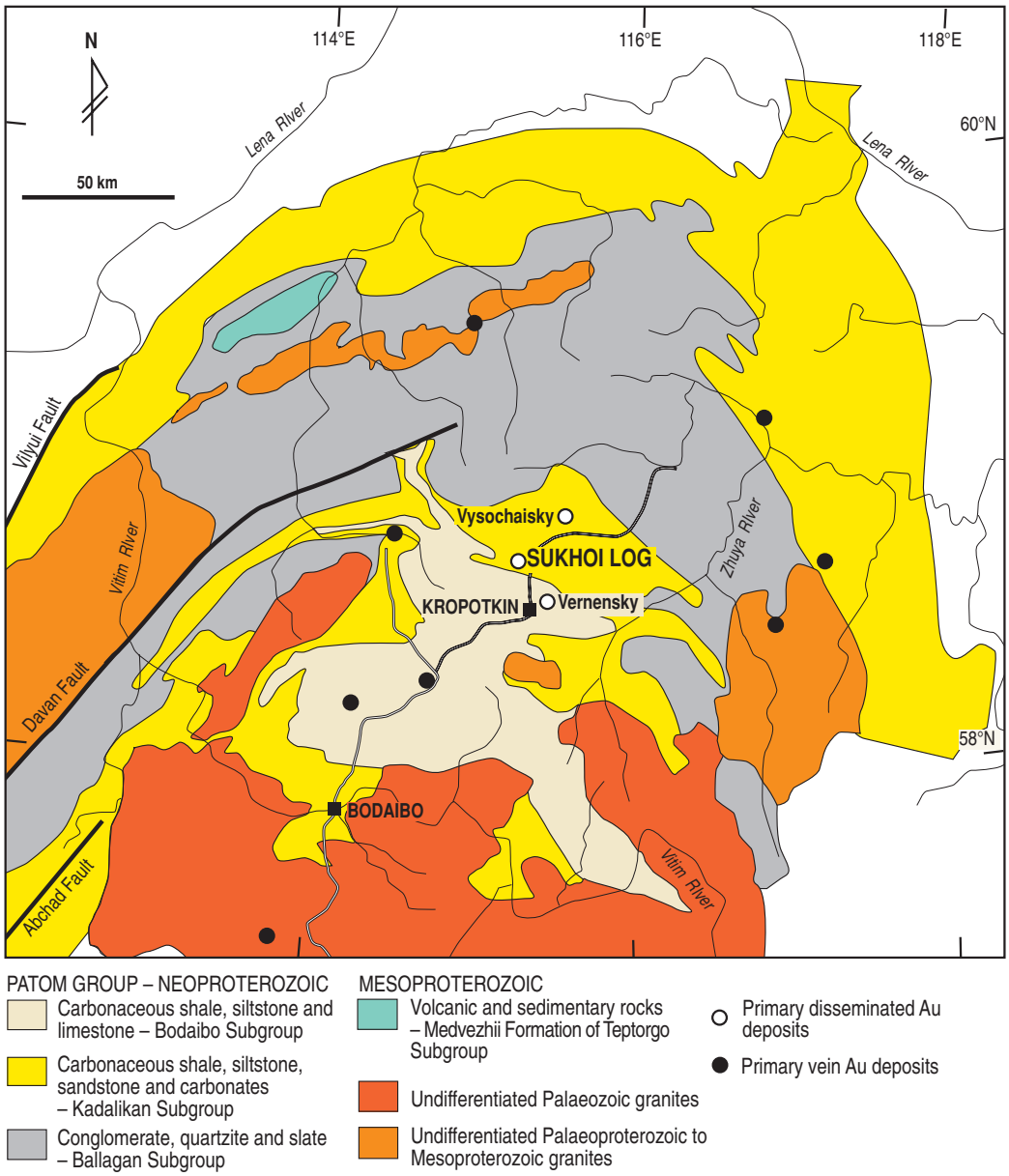

FIG. 2. Geology of the Lena gold province, showing the position of Sukhoi Log and some other bedrock gold deposits and prospects (modified from Wood and Popov, 2006).

Log is of the disseminated gold-pyrite type. About 60 Au-bearing quartz vein occurrences, 40 disseminated gold-pyrite occurrences, and 30 gold-pyrrhotite occurrences have been reported in the central part of the Lena gold province (Buryak, 1982; Yakubchuk et al., 2005, fig. 5). Over 80 percent of these gold occurrences occur in the black-shale– dominated facies of the Kadalikan and Bodaibo Subgroups of the Patom Group, particularly in the Khomolkho Formation and are constrained to several west-northwest–east-southeast–striking subparallel belts, approximately 10 to 30 km apart, corresponding to linear anticlinal folds and related thrust faults (Yakubchuk et al., 2005). The metamorphic grade in the central part of the Lena gold province surrounding Sukhoi Log and hosting other disseminated Au pyrite occurrences is chlorite-sericite subfacies of the greenschist facies. In contrast, the disseminated Au pyrrhotite mineralization in the gold province is typically hosted in higher metamorphic facies, either biotite-chlorite subfacies or epidote-amphibolite facies (Buryak and Khmelevskaya, 1997).

Recent LA-ICPMS geochronological studies (Scott et al., 2007) on detrital zircons in the mineralized siltstones and sandstones of the Khomolkho Formation at Sukhoi Log indicate a maximum sedimentation age of 600 Ma, which is significantly younger than the previous estimates of around 700 to 800 Ma (Distler et al., 2004; Kuz'min et al., 2006). The main phase of metamorphism in the Bodaibo trough has been dated at 516 ± 22 Ma (Laverov et al., 2000a, b; Distler et al., 2004). Recent U-Th-Pb LA-ICPMS dating of metamorphic

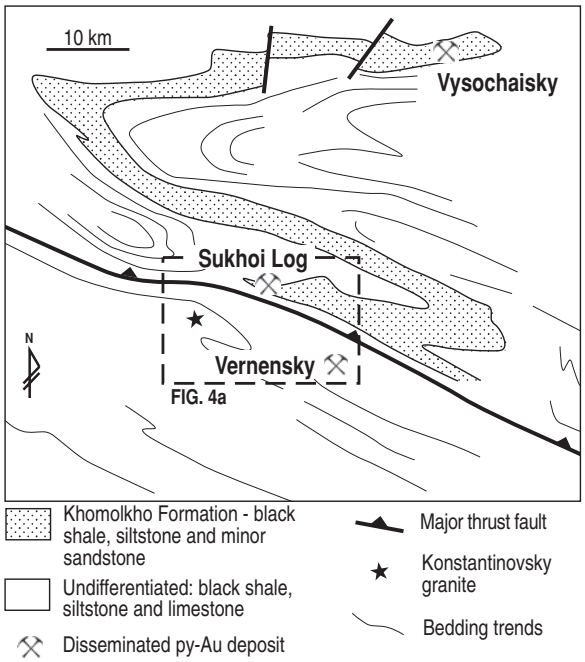

FIG. 3. Distribution of the Khomolkho Formation carbonaceous shales and siltstones that host the Sukhoi Log deposit, in the central portion of the Lena gold province. The outcrop pattern of the Khomolkho Formation and bedding trend lines are interpreted from satellite images.

monazites has returned a similar age of 516 ± 10 Ma (Scott et al., 2007). Subsequent to folding and metamorphism, the Patom Group was intruded by early Paleozoic granites. The main granite batholiths 75 km southwest and 100 km southeast of Sukhoi Log (Fig. 2) have been dated by the zircon U-Pb method at 354 ± 12 to 320 ± 10 Ma, whereas the small Konstantinovsky granite stock, 6 km to the southwest of Sukhoi Log (Figs. 3, 4), has a zircon U-Pb age of 290 ± 20 Ma (Neymark et al., 1995; Larin et al., 1997).

Geology and Structure of the Deposit

The Sukhoi Log deposit is hosted by black shales, mudstones, and minor siltstones of the Khomolko Formation, which form a thinly bedded distal turbidite sequence. Significantly, no intrusive rocks have been observed within or adjacent to the deposit. The host sedimentary rocks have been deformed into a series of south-verging folds and associated thrust faults (Figs. 3, 4). The deposit occurs in the core of the very tight, south-verging Sukhoi Log anticline, which is located in the hanging wall of a south-verging thrust fault. The anticline plunges gently to the west-northwest and its axial surface dips 20° to 30° north-northeast (Fig. 4b).

The host rocks are overprinted by a variably but generally strongly developed axial planar cleavage (Fig. 4c). Fold hinge areas are characterized by well-preserved bedding and variably developed pressure-solution cleavage (Fig. 5a-c), whereas fold limb areas are marked by subparallelism of bedding and cleavage planes (Fig. 5b-d, f). Facing directions from graded bedding and the absence of preserved earlier cleavage planes in mesoscopic fold hinges are consistent with the host rocks having been affected by a single folding event, at least in the vicinity of the deposit. However, an overprinting crenulation cleavage has been observed locally. A number of thrust faults, subparallel to cleavage, are also present and display variable offsets of the folded beds (Fig. 5a, c).

The mineralized zone forms a gently dipping tabular body, parallel to the axial plane of the fold (Fig. 4b). The zone extends in excess of 2,000 m along strike and 700 m downdip. Asymmetry of mesoscopic folds, younging directions from graded beds, and bedding-cleavage relationships within and around the mineralized zone (Fig. 4c) indicate that the deposit is generally but not strictly located along the axial surface of the south-verging anticline. The envelope of the deposit is thus discordant to stratigraphic units and spans a stratigraphic interval of nearly 1 km (Fig. 4a, b).

In detail, however, mineralization is not uniformly distributed within the deposit-scale envelope along the axial plane of the fold. Ore zones are best developed and thickest in two black shale units (Khomolho hm1 and 3), reflecting a second-order stratigraphic control of mineralization (Wood and Popov, 2006). In addition, gold mineralization forms "wings" that extend along specific units away from the axial surface of the fold and define crescent-shaped bodies with a strong strata-bound component. This distribution pattern of mineralization is therefore one of stacked strata-bound zones linked by discordant zones and defines an overall deposit-scale folded Christmas tree geometry.

Nature and Styles of Pyrite and Gold Mineralization and Alteration

The Sukhoi Log deposit is essentially a disseminated gold-bearing pyrite deposit in carbonaceous shales and siltstones, with a number of distinct structural and textural styles of mineralization. The boundaries of the deposit are defined by Au grade and overall abundance of pyrite, rather than by any clear lithologic change. Within the deposit the pyrite content varies from 2 to 10 wt percent, averaging 2.5 to 4 wt percent, whereas outside the deposit, the pyrite content is commonly less than 2 wt percent. The highest gold grades (>2 g/t mean) are concentrated within the general hinge zone of the fold, where pyrite-quartz veinlets are more abundant (Distler et al., 2004). Elevated gold grades are also developed within thickened black shale units where they intersect the anticlinal hinge (Fig. 4b; Wood and Popov, 2006). The higher grade core of the deposit is surrounded by a halo of siderite porphyroblasts and disseminated pyrite with lower gold grades, ranging from 0.1 to 2 ppm Au.

As observed underground, the higher grade core of the deposit is mainly characterized by an abundance of folded, cm-scale bedding-parallel pyrite-quartz veinlets (Figs. 4c, 5a-c), as well as disseminated pyrite, pyrite nodules, and quartz-pyrite aggregates (Fig. 5d). Based on our observations from underground exposures, on nine diamond drill holes throughout the deposit, and on descriptions from Distler et al. (2004) and Wood and Popov (2006), five main styles of mineralization can be defined. Their key textural and structural characteristics are described below. Of these five, the first two account for the bulk of the gold mineralization

Pyrite-quartz veinlets and aggregates

The dominant feature of the higher grade mineralization is the presence of folded pyrite-quartz veinlets. These veinlets

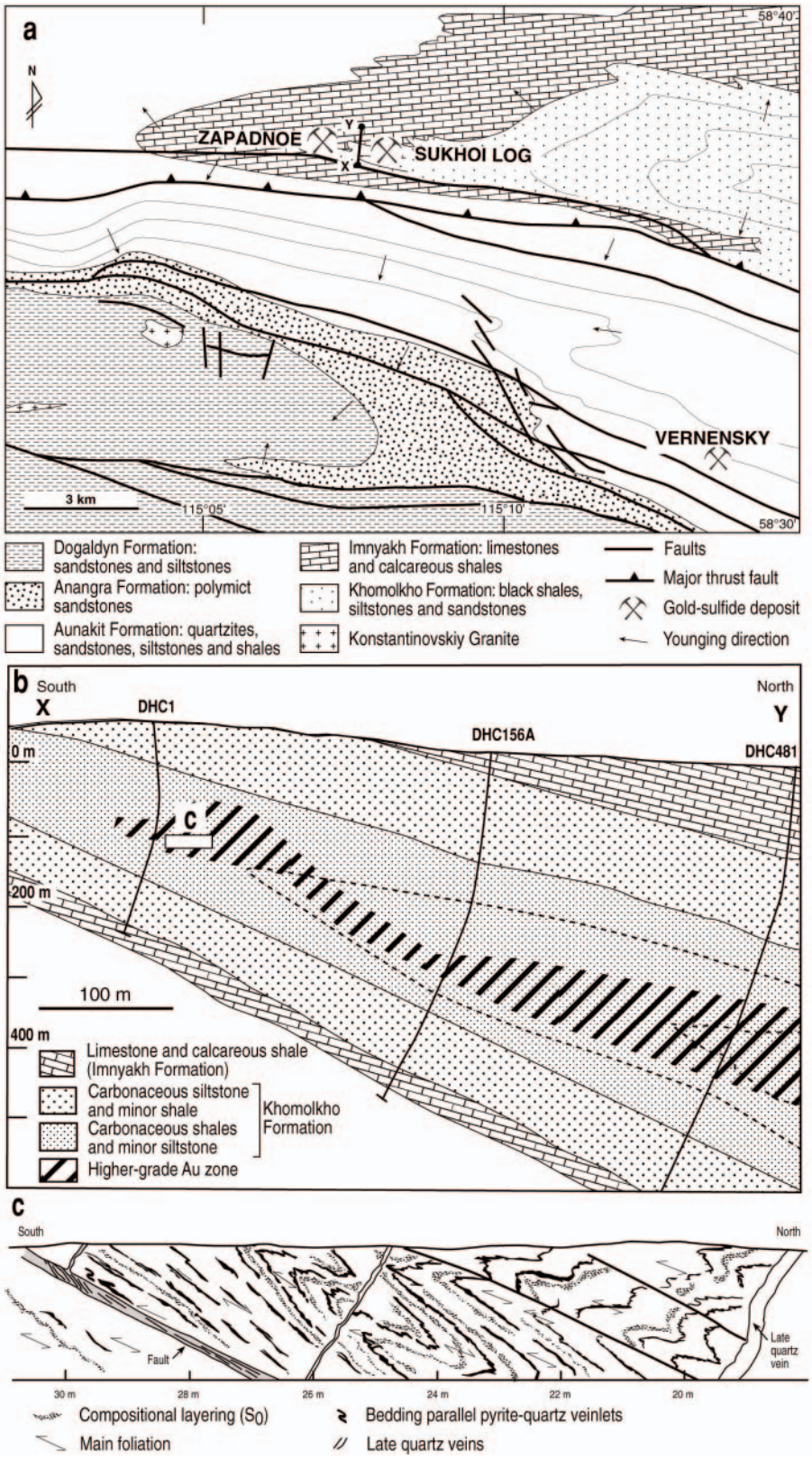

FIG. 4. a. Local surface geology of the environs of Sukhoi Log (modified from Buryak and Khmelevskaya, 1997). b. Schematic cross section AB of geology of the Sukhoi Log deposit (modified from Wood and Popov, 2006), showing the extrapolated position of three of the drill holes sampled in this study. c. Sketch map of the west wall of a representative underground crosscut to the deposit, showing the geometric relationships between bedding, bedding-parallel quartz-pyrite veinlets, cleavage, and quartz veins (F. Robert, unpub. report for Barrick Gold Corp., 1998, 24 p.).

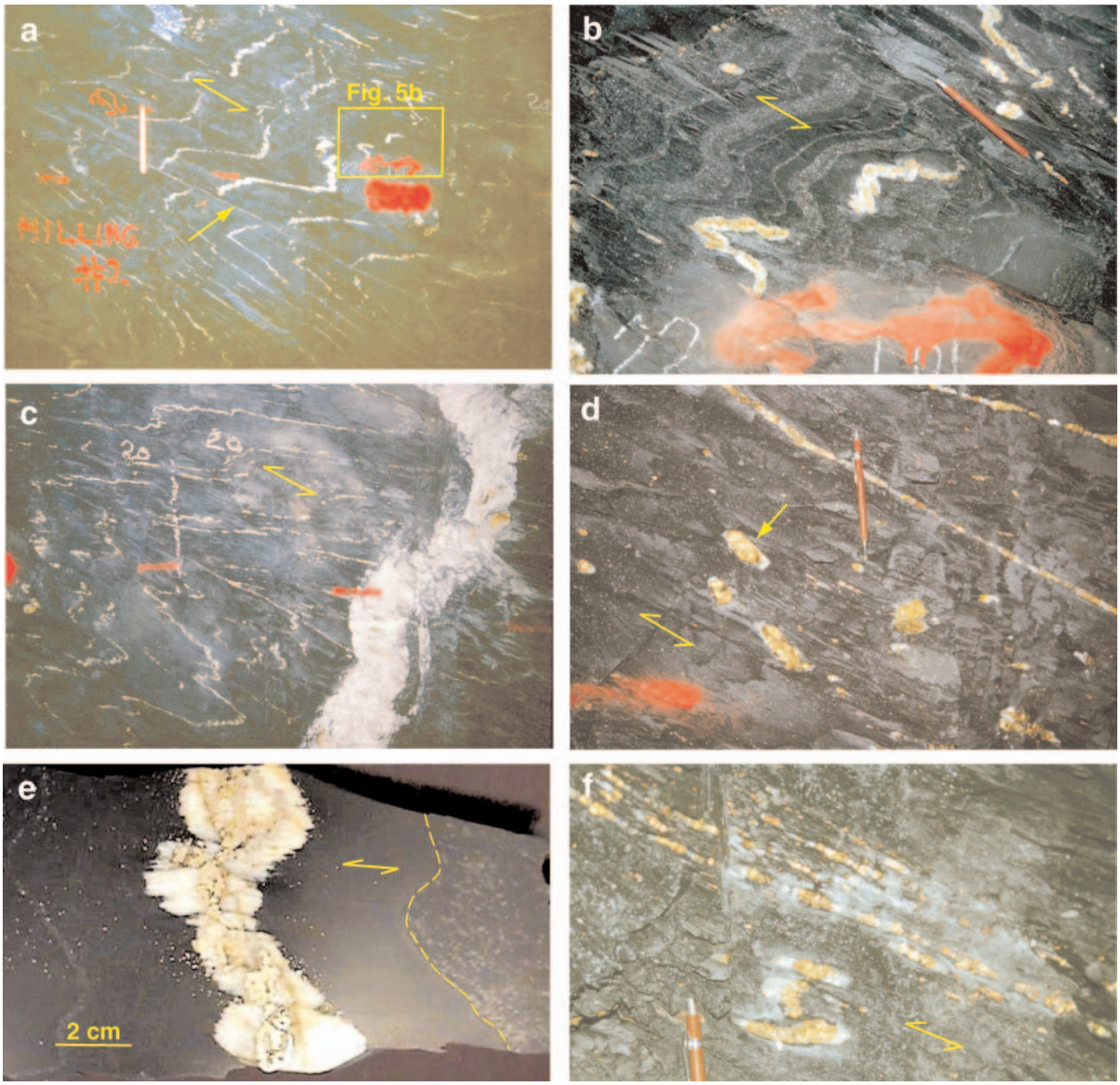

FIG. 5. Mesoscopic features of mineralization in crosscut 39, Sukhoi Log, all views looking west, except for (e). a. General view of folded gold-bearing pyrite-quartz veinlets, showing significant boudinage on the limbs of the central mesoscopic fold. Arrow points to a cleavage-parallel discontinuity, also filled with quartz-pyrite. Red stick is 15 cm long. b. Close-up view of area indicated in (a), showing folded beds in the hinge of a mesoscopic fold and buckled and discontinuous bedding-parallel pyrite-quartz veinlets. Note the stripy axial planar pressure-solution cleavage (pencil for scale). c. Folded bedding-parallel pyrite-quartz veinlets cut by a late milky white quartz vein cutting opposing limbs of folds. d. Close-up view of pyrite aggregates with quartz pressure shadows (arrow), and pyrite-quartz veinlets subparallel to cleavage (behind the pencil; pencil for scale). e. Detail of a bedding-parallel pyrite-quartz layer, showing the fibrous quartz fringing a central pyrite layer and parallel to cleavage (bedding surface indicated by white dashed line). f. Detail of pyrite-quartz segregations separated by pressure-solution seams (arrow) that were likely part of a folded bedding-parallel veinlet. Note the cleavage-parallel pyrite-quartz veinlets in which pyrite grains are separated by fibrous quartz parallel to cleavage (top right half of photograph).

are 2 to 3 cm thick, on average, and contain 30 to 50 vol percent pyrite (Figs. 5b, e, f, 6a). Analysis of 22 hand samples of these pyrite-quartz veinlets gave a median concentration of 27.5 ppm Au (Barrick Gold Corporation, unpub. data). Buryak and Khmelevskaya (1997) reported a grade variation of 0.1 to 360 ppm with an average of 65 ppm Au for the folded pyrite-quartz veinlets. Coarse pyrite euhedra (0.5–2 cm) typically form a central band within the veins, fringed by beards of fibrous quartz oriented parallel to the cleavage plane (Figs. 5b, e, 6a). Unlike typical fracture-filling veins, these veinlets have irregular walls and thicknesses, reflecting variations in the length of the fringing quartz fibers (Fig. 5e). The pyrite-quartz veinlets are parallel to bedding and mimic the folded sedimentary beds (Fig. 4c). This relationship is particularly clear in the hinges of mesoscopic folds (Figs. 5a-c, e, 6a). These relationships suggest that the quartz-pyrite veinlets

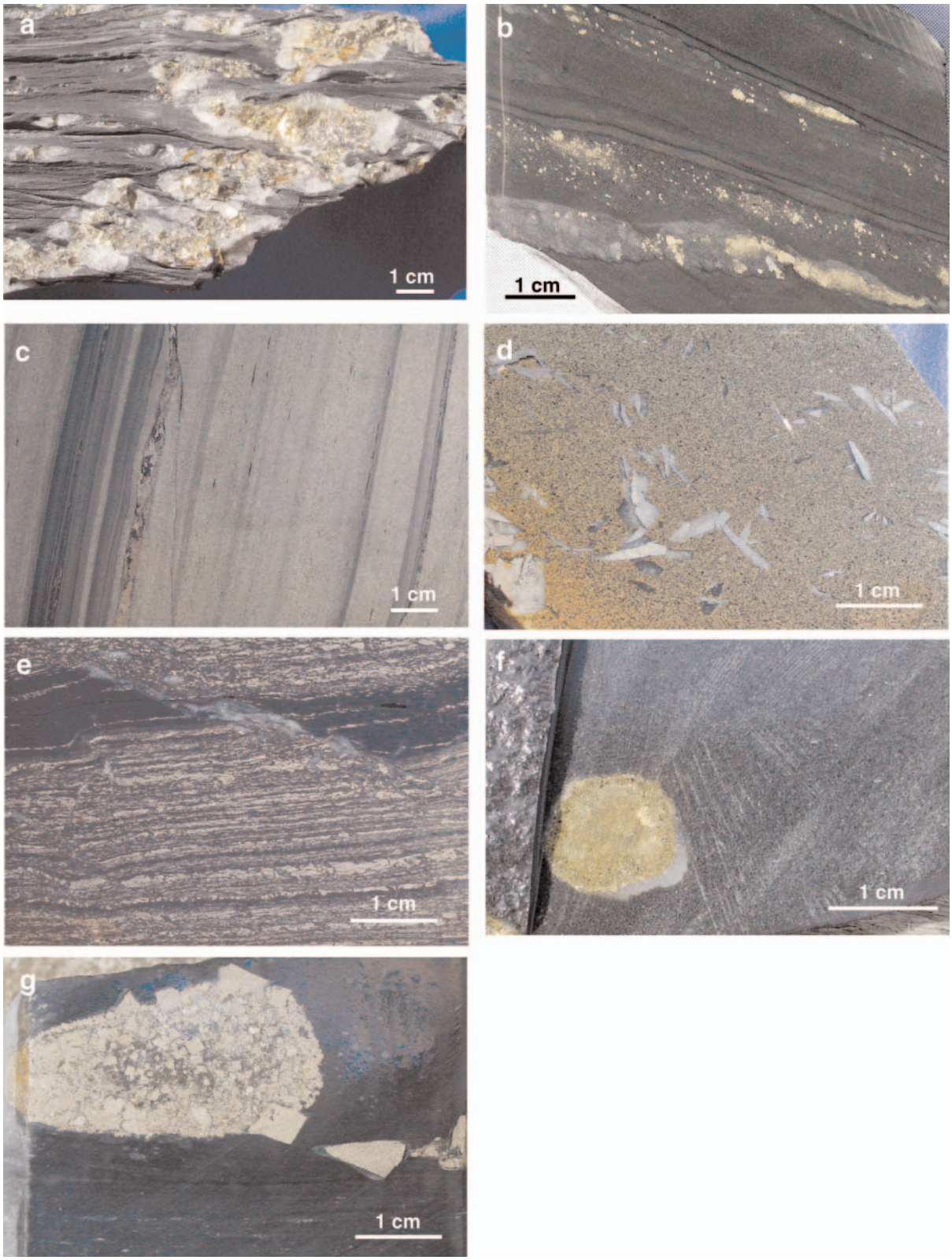

FIG. 6. The main styles of sulfide mineralization at Sukhoi Log. a. Folded gold-bearing pyrite-quartz veinlet in gray, shale showing intense stripy cleavage. b. Bedding-parallel bands of disseminated pyrite in black shale (py_1, py_2, and py_3). c. Very fine grained stratiform semimassive pyrite in black shale (py_1). d. Coarse disseminated arsenopyrite in sideritic siltstone. e. Laminated bedding-parallel pyrrhotite in black shale. f. Diagenetic pyrite nodule in siltstone composed of py_1 and py_2; the pyrite in the nodule is partly recrystallized with development of a quartz pressure shadow. g. Pyrite nodule composed dominantly of diagenetic and metamorphic euhedral py_3 and py_4.

predate or formed in the earliest stages of the folding of their host rocks. In the fold limbs, the veinlets are variably boudinaged, consistent with their progressive rotation toward the cleavage plane during folding and pressure solution deformation (Figs 5a lower left, b upper right).

The continuity of pyrite-quartz veinlets along bedding planes is highly variable but rarely exceeds 1 m (Fig. 5a, c). Part of this discontinuous character predates the folding and is likely a primary attribute of this style of mineralization, which shows a range from isolated aggregates (Fig. 5d) to short veinlets (Fig. 5b), to more continuous ones (Fig. 5a). Some of the discontinuous character of these veinlets can also result from overprinting deformation and structural disruption (Fig. 5d, f)

A few pyrite-quartz veinlets are oriented subparallel to cleavage and appear to occupy discrete planes at high angles to the bedding (Fig. 5a, c, d). These veinlets have the same composition as the bedding-parallel veinlets and consist of isolated pyrite euhedra separated by longer segments of fibrous quartz parallel to the veinlet (Fig. 5f). They also have similar grades as the bedding-parallel veinlets (Barrick Gold, unpub. data). These veinlets are best interpreted as discordant veinlets, similar in age to the bedding-parallel veinlets but originally at high angles to bedding. This interpretation would account for their significant boudinage and their common coincidence with slip surfaces (Fig. 5a, arrow). Although, the possibility that some of these cleavage-parallel veinlets represent a later stage of quartz-pyrite veining cannot be entirely ruled out, it seems inconsistent with the high degree of strain they display.

Disseminated fine-grained stratiform pyrite

This style of sulfide mineralization occurs as euhedral to subhedral pyrite crystals from <0.1 to 2 mm across and makes up 1 to 5 vol percent of the rock (Fig. 6b). Disseminated pyrite is more abundant in the calcareous sandstone and siltstone beds compared to argillaceous shale beds. Euhedral pyrite grains typically occur in bands parallel to bedding (Fig. 6b) and are preferentially concentrated in thin siltstone beds and commonly along the contact with adjacent shale beds. The fine-grained pyrite euhedra rarely develop quartz strain fringes. Very fine grained stratiform semimassive pyrite (10–40 vol % pyrite) is developed in some black shale beds (Fig. 6c). This particular style of semimassive stratiform pyrite is not common but is well developed in DDH C1 on section line +1.

Limited analyses (eight samples) of the stratiform disseminated pyrite style of mineralization indicate a gold content from 0.1 to 0.7 ppm. Buryak and Khmelevskaya (1997) reported a variation from 0.01 to 1 ppm Au, significantly exceeding background values but not reaching economic concentrations.

Disseminated arsenopyrite is also locally present and is best developed in siltstone and sandstone facies (Fig. 6d) at the margins of the orebody, where it varies in abundance from 1 to 4 vol percent. Disseminated, fine-grained pyrrhotite has also been observed in black shale facies, where it varies from 1 to 10 vol percent in abundance (Fig. 6e) but is commonly lacking significant gold (0.01–0.1 ppm Au in six samples)

Pyrite nodules

Rounded nodules of pyrite that vary from 0.5 to 10 cm across are also present within the deposit. Some nodules are composed of massive fine-grained pyrite and show well-developed quartz strain fringes (Fig. 6f), suggesting a pretectonic, possibly diagenetic, origin; others are composed of aggregates of coarse euhedral crystals (Fig. 6g) and may result from metamorphic recrystallization of diagenetic nodules or segregations of metamorphic pyrite. Buryak and Khmelevskaya (1997) reported that pyrite lenses, concretions, and concretion-like accumulations contain from 0.1 to 350 ppm Au with a mean of 60 ppm. Wood and Popov (2005) discussed similar tectonized pyrite nodules with a gold content from 22 to 113 ppm.

Coarse euhedral pyrite

Isolated, large pyrite euhedra from 0.5 to 4 cm across are also commonly developed in the shaly beds toward the margin and outside the orebody (Fig. 7a). This euhedral pyrite typically displays narrow quartz strain fringes, with a pyrite/quartz ratio of about 6/1. Gold content in this style of sulfide mineralisation varies from 0.01 to 5 ppm, with a mean of 0.4 ppm Au (Buryak and Khmelevskaya, 1997).

Quartz veins

Moderately to steeply dipping milky white quartz veins, up to 20 cm thick, are also present in the deposit. These veins clearly cut the folded turbidite beds and the bedding-parallel pyrite-quartz veinlets (Figs. 4c, 5c). These late, postore veins only contain minor amounts of pyrite and much lower levels of gold than the folded pyrite-quartz veinlets (mean 1.9 ppm, compared with 65 ppm Au for the latter: Buryak and Khmelevskaya, 1997)

Hydrothermal alteration

Distler et al. (2004) reported that the carbonaceous shale host rocks are similar in composition to the North American Shale Composite (Taylor and McLennan, 1985), except that they contain elevated S (up to 20 wt %), organic carbon (0.2–2.7 wt %), and Na_2O (0.6–2.2 wt %). The dominant minerals are quartz (30–50 vol %), sericite (35–50 vol %), and carbonate (5–30 vol %). The most obvious alteration, which appears to be related to gold mineralization, is abundant Fe-Mg carbonate and siderite porphyroblasts (Figs. 5b, 7b). Sandstone beds show uniform fine-grained siderite replacement of the matrix (Fig. 7c), whereas shale and siltstone beds develop siderite porphyroblasts (Fig. 7b) from 2 to 7 mm aligned parallel to the main cleavage. The siderite porphyroblasts may occur throughout the ore zone but are particularly well developed in a halo zone within both the hanging-wall and footwall sediments.

Summary of key structure-mineralization relations and implications

Two aspects of the auriferous bedding-parallel pyrite-quartz veinlets have particularly important implications for the origin and timing of mineralization. First, as indicated above, these pyrite-quartz veinlets have clearly been overprinted by the folding of the host rocks and the related pressure-solution processes. Second, the fibrous quartz within the

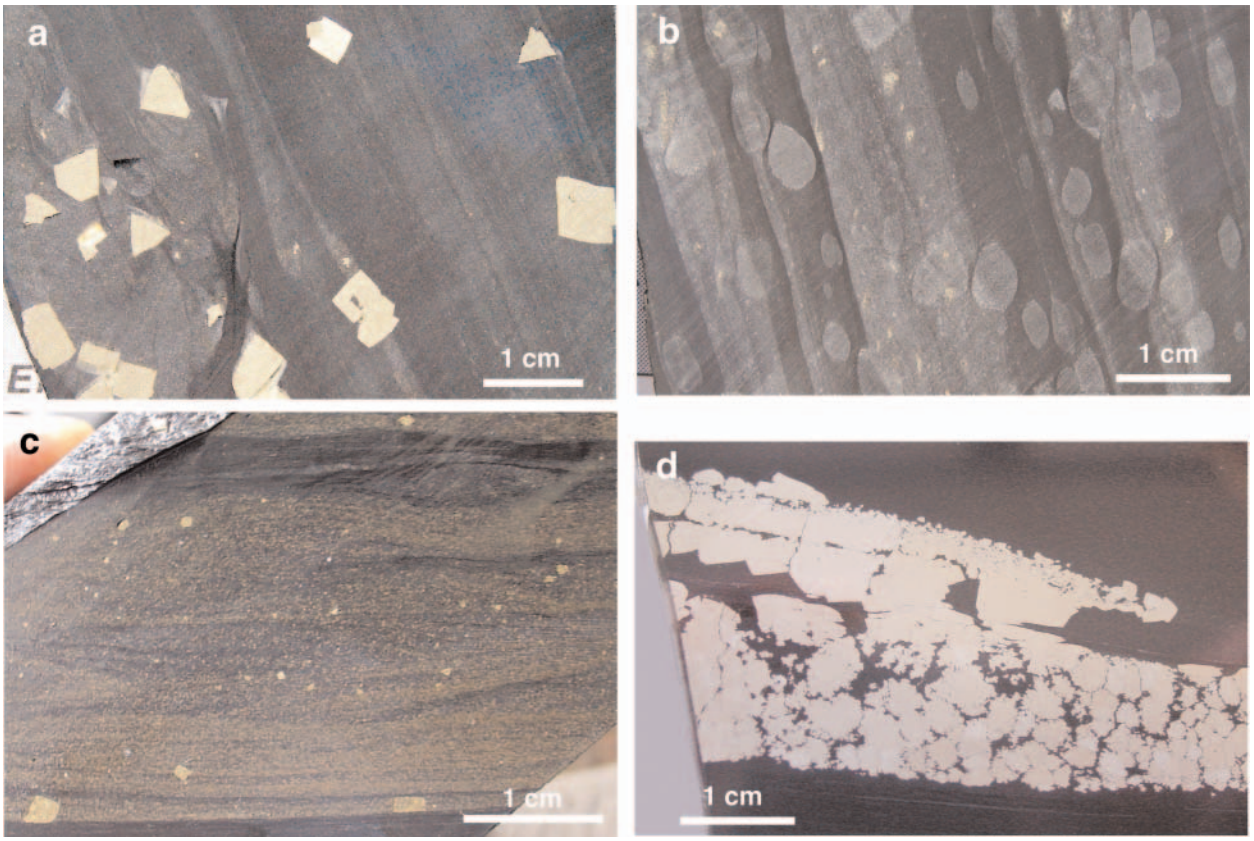

FIG. 7. a. Coarse-grained pyrite euhedra (py_4) within laminated mudstone-siltstone. b. Iron-carbonate metamorphic spots, or porphyroblasts, in laminated gray shale-siltstone. c. Siltstone with minor disseminated pyrite; brown coloration is due to siderite alteration. d. Coarse anhedral pyrite (py_3) developed along bedding in siltstone layer.

quartz-pyrite veinlets and isolated segregations clearly represents strain fringes developed on preexisting pyrite (Fig. 5d-f). This interpretation is reinforced by the observation that there is no fibrous quartz developed in the absence of pyrite, which also rules out the possibility that the fibrous quartz represents recrystallized or foliated veinlets. The orientation of the quartz fibers is systematically parallel to cleavage, irrespective of the high angle (Figs. 5e, 6a) or low angle (Fig. 5f, see upper right) of the veinlets relative to the cleavage plane. These relationships indicate that the quartz fibers accompanied the development of the axial planar cleavage and associated pressure-solution processes during the folding and are syntectonic in origin. The common presence of pressure solution seams (Fig. 5e, 6a) supports this concept that much of this quartz is secondary in origin. Thus, the bedding-parallel veinlets were originally most likely devoid of fibrous quartz and consisted only of disseminated pyrite layers parallel to bedding, to which fibrous quartz was added during folding and cleavage development.

The development of the pyrite-quartz veinlets can thus best be explained by a two-stage process: development of discontinuous pyrite layers along bedding prior to, or during, the earliest stages of folding of the sedimentary strata, followed by syntectonic additions of secondary fibrous quartz during subsequent folding and associated development of pressure-solution cleavage. Thus, prior to, or at the onset of, folding, Sukhoi Log mineralization probably consisted of discontinuous pyrite-dominated bedding-parallel layers and isolated pyrite aggregates and nodules largely devoid of quartz. However, despite the mesoscopic strata-bound character of the pyrite layers, the overall envelopes of mineralization indicate that the deposit was originally discordant to lithologic units, as argued above (Fig. 4b).

Sampling and Analytical Techniques

Samples for the textural and geochemical study where collected from nine core drill holes. Drill Holes C1, C2, C156A, C481, C176, and C524 all pass through the central high-grade resource. The positions of drill holes C1, C156A and C481 are shown in Figure 4b. Drill hole C660 intersected lower grade mineralization from the downdip extension of the main zone 500 m to the north of the main resource. Drill hole C59 intersected very weak gold mineralization 1 km along strike to the east, and drill hole C97A intersected similar weak mineralization 2 km to the west of Sukhoi Log. Although the complete drill holes were not available for sampling, a suite of 174 samples were collected from the mineralized and nonmineralized sediments in the holes to provide a complete spectrum of the various mineralization styles at Sukhoi Log. An additional seven surface samples of gold-bearing pyrite-quartz veinlets were collected from the Zapadnoe open cut on the western continutation of Sukhoi Log (Fig. 4a). Mineralogical

and textural studies were conducted on 130 thin sections and polished mounts of which 44 were analyzed by LA-ICPMS for pyrite geochemistry.

LA-ICPMS analyses

Concentrations of trace elements in pyrite, pyrrhotite, and arsenopyrite were determined by laser-ablation inductively coupled plasma mass spectrometry (LA-ICPMS) at CODES, University of Tasmania. The instrumentation employs a 213-nm New Wave UP213 solid state Nd-YAG laser microprobe coupled with an Agilent 4500 quadrupole mass spectrometer. The laser microscope is equipped with an 8× lens. Analyses were performed in an atmosphere of pure He.

Most analyses were performed in spot mode using a laser beam of 25 to 40 μm, a repetition rate of 5 Hz and laser energy of ~6 J/cm^2. Smaller spot sizes (down to 10 μm) were used on particularly fine grained pyrite. Data were collected in the time-resolved mode. Each analysis time was 90 s, including a 30-s preablation background measurement. This allowed for a 45- to 50-s interval of useful data acquisition with the laser on, resulting in ~70 sweeps with 20-ms dwell time on each mass. Chemical compositions along several profiles across pyrite grains were also measured. The data were acquired when the sample was moving with a constant rate of 3 μm/s under a fixed beam. The length of profiles was 300 to 500 μm.

All analyses were quantified against STDGL2b2 standard (Danyushevsky et al., 2003), following the procedure of Longerich et al. (1996) and using Fe as the internal standard. The standard is an XRF-style glass disk prepared by fusing a doped mixture of Zn concentrate and pyrrhotite with lithium borate flux and LiNO3. The standard was analyzed two times every 1 to 2 h. All results were linear drift corrected. Mass-spectrometer drift was <5 percent between each standard measurement.

Two hundred and sixty-four LA-ICPMS spot analyses of pyrite were measured on 30 samples from the ore zone and barren host rocks selected from seven of the nine drill holes sampled at Sukhoi Log. An additional 153 LA-ICPMS analyses of pyrite within bedding-parallel quartz veinlets were measured from 14 samples collected from the underground development at Sukhoi Log and the Zapadnoe open cut at the western end of the deposit. An additional 24 analyses of pyrrhotite and 56 analyses of arsenopyrite were measured. A selection of the data for 48 typical sediment-hosted pyrite, pyrrhotite, and arsenopyrite analyses is given in Table 1, and 18 typical pyrite and arsenopyrite analyses from the bedding-parallel pyrite-quartz veinlets are given in Table 2.

Textures of Pyrite and Other Sulfides

From our detailed studies, pyrite from the different styles of mineralization distinguished above has been grouped into six types; pyrite 1 (py_1) to pyrite 6 (py_6) based on grain size, texture, and interpreted paragenesis (Table 3). Note that these are not the same groups (Pyrite I, II, and III) described by Wood and Popov (2006). Pyrites 1 to 6 represent different textural and/or paragenetic forms of pyrite within the disseminated stratiform pyrite, pyrite nodules, coarse euhedral pyrite, and the pyrite-quartz veinlet styles of mineralization described above. However there is not a one-to-one relationship between textural and/or paragenetic types of pyrite and styles of mineralization, as most styles of mineralization contain two or more paragenetic types of pyrite. The individual pyrite types are discussed in the order of their interpreted paragenetic sequence. This is followed by a description of the more complex pyrite-quartz veinlets, which contain several generations of pyrite.

Pyrite 1

Py_1 consists of fine-grained layered or banded concentrations of pyrite parallel to bedding in carbonaceous black shale (Figs. 6c, 8a). This type is most common in the disseminated stratiform style of pyrite mineralization described above. The pyrite occurs as euhedral microcrystals, from 1 to 3 μm across, that form irregularly shaped clusters from 50 to 150 μm across (Fig. 8b). The py_1 clusters are distributed along the bedding in the shale. Minor bands of py_1 are present in most of the drill holes sampled in this study, but by far the best development of py_1 is in drill hole C1, which intersects the updip part of the gold zone toward the southern margin of the deposit (Fig. 4b). Two other textural styles of py_1 have been recorded: framboidal py_1, which displays typical framboid textures of pyrite microcrystals in spheres from 10 to 20 μm across (Fig. 8c, d), and "sooty" py_1, which is composed of very fine grained poorly crystalline needle-, rod- and cube-shaped intergrowths interspersed with black amorphous material (Fig. 8e, f). This stratiform, framboidal, and sooty pyrite is texturally similar to syngenetic or syndiagenetic pyrite that is common in SEDEX Zn-Pb-Ag deposits (e.g., Croxford and Jephcott, 1972; Large et al., 2005).

Pyrite 2

Py_2 forms coarser grained euhedral to subhedral clusters that commonly surround and overgrow py_1 (Fig. 8d) or develop from recrystallization of py_1. They are commonly developed in the disseminated stratiform pyrite style. Py_2 euhedra vary from 20 to 50 μm across, compared with py_1 microcrystals, which are 1 to 3 μm across (Fig. 8d, e). Many py_2 crystals have inclusion-rich pyrite cores composed of partially recrystallized py_1, black amorphous material, and original wall rock (Fig. 8f). Py_2 is interpreted as diagenetic in origin as it overgrows the earliest py_1 and is overgrown by late diagenetic and metamorphic py_3 and py_4.

Pyrite 3

Py_3 is coarser grained than py_2 and forms anhedral to euhedral crystals, commonly confined to calcareous sandstone and siltstone layers within the black shales (Fig. 7d, 9a). Py_3 may occur in either the disseminated stratiform style or the coarse euhedral style of pyrite mineralization. Py_3 crystals vary from 2 to 5 mm across and contain abundant inclusions of silicate and carbonate minerals, along with pyrrhotite, sphalerite, and chalcopyrite (Fig. 9b, c). Within the ore zone, native gold is also present as inclusions in py_3 (Fig. 9c). Etching with nitric acid reveals that py_3 has formed by overgrowing and replacing detrital quartz and other minerals in the sedimentary rock (Fig. 9d). The abundance of unoriented inclusions of sedimentary matrix material within py_3 (Fig. 9b, c) suggests initial growth of the pyrite prior to cleavage development, most likely during late diagenesis. However some examples show a clear preferential alignment of detrital quartz

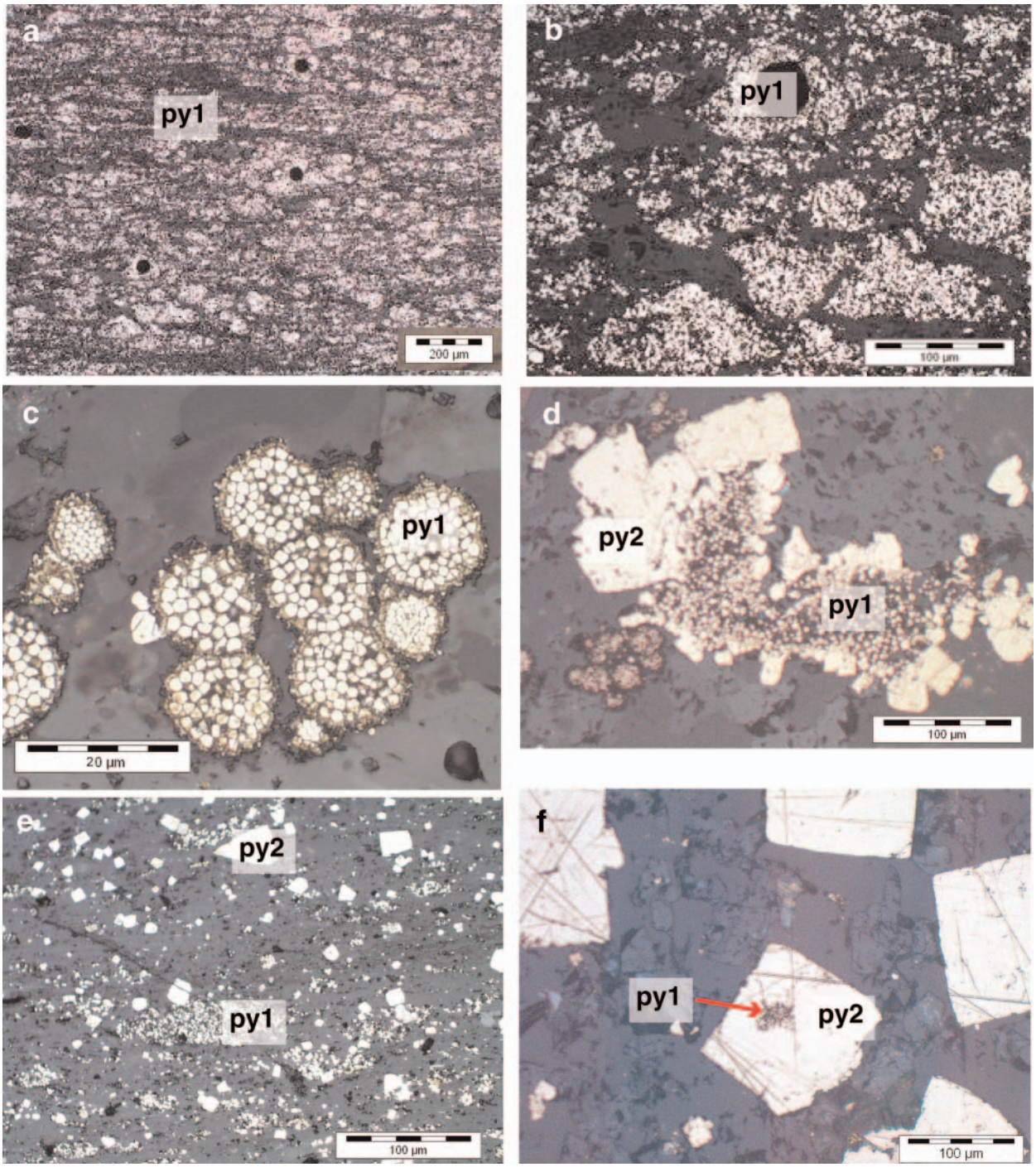

FIG. 8. Textures of py_1 and py_2 types. a. Clusters of py_1 microcrystals in laminated semimassive sulfide. b. Py_1 clusters in black shale. c. Py_1 framboids in gray siltstone. d. Cluster of py_1 microcrystals surrounded by larger py_2 euhedra. e. Typical textural arrangement of fine py_1 clusters and coarser disseminated euhedral py_2 in black shale. f. Coarse euhedral py_2 surrounding and overgrowing a cluster of sooty py_1.

grains parallel to cleavage, preserved in the internal texture of py_3 (Fig. 9d), indicating that the pyrite continued to form during the early stages of deformation.

Pyrite 4

Py_4 occurs as large, isolated euhedral crystals from 3 to 40 mm across within black and gray shale beds (Figs. 7a, 10a) and is typical of the coarse euhedral pyrite style of sulfide mineralization. Py_4 euhedra commonly show quartz strain fringes, which become more pronounced in the strongly deformed zones in the core of the Sukhoi Log anticline. Visually, this is the dominant pyrite type in the outer parts and halo of the ore deposit. Etching with nitric acid reveals a well-developed tectonic fabric within the pyrite (Fig. 10a-c), which

TABLE 1. Selected LA-ICPMS Analyses of Pyrite, Pyrrhotite, and Arsenopyrite Hosted

Sample no.	Analysis no.	Sulfide type	Au (ppm)	Al (ppm)	Ti (ppm)	V (ppm)	Cr (ppm)	Mn (ppm)	Fe (ppm)	Co (ppm)	Ni (ppm)	Cu (ppm)	Zn (ppm)
SL-1-91a	FE09A09	Py_1	0.65	3852.48	13.10	3.70	6.92	77.59	457000	117.37	88.52	23.05	86.77
SL-1-91a	FE09A07	Py_1	0.75	7699.32	91.35	13.09	11.03	78.77	452000	173.15	175.43	43.37	107.65
156/286.5-4	MA23A71	Py_1	1.54	2588.26	135.36	2.47	6.06	3.67	465000	71.76	118.07	191.48	14.34
176/300-13	MA23A43	Py_1	2.50	109.35	7.33	1.43	6.00	24.67	465000	11.39	85.09	241.42	14.35
156/225-C2-2	MA14A14	Py_1	3.91	458.32	27.41	0.73	6.00	1954.48	465000	243.63	876.00	134.47	24.60
524/70.9-3-1C	AP04A77	Py_1 core to py_3	4.16	285.83	3401.98	3.40	10.16	13.06	465000	70.18	154.15	68.69	6.45
156/225-C2-3	MA14A15	Py_1 framb	6.96	10678.39	94.56	14.57	17.81	1630.32	465000	208.04	1259.63	459.03	32.36
524/68.5-NC-2	AP04A94	Py_1 sooty	5.02	29315.18	174.63	45.80	44.04	256.14	465000	2016.51	1023.10	302.24	36.10
176/300-5	MA23A35	Py_1 sooty	12.14	9698.67	159.63	27.83	23.62	47.60	465000	138.49	488.23	305.34	9.50
Py_1 mean composition for n = 66		mean py_1	3.32	10852.38	190.09	19.07	25.50	329.78	standard	223.09	431.07	155.45	57.44
156A/331.3-9	MA23A26	Py_2	0.17	<0.29	6.04	<0.11	<2.0	<1.0	465000	12.85	200.47	9.26	2.20
524/68.5-NC-3	AP04A95	Py_2	0.32	15.31	1.25	<0.11	<2.0	<1.0	465000	157.91	230.28	23.62	2.20
524/81-C2-1	MA14A63	Py_2	1.03	40.92	535.05	<0.11	<2.0	138.86	465000	1019.05	2179.66	142.73	24.88
156/526-5	MA23A79	Py_2	2.24	189.31	319.24	0.86	<2.0	2.13	465000	71.54	961.98	111.50	2.20
156/299-C2-1	MA23A54	Py_2 cluster	0.05	<0.91	6.94	<0.11	<2.0	<1.0	465000	7.95	4.78	4.87	2.20
176/300-2	MA23A32	Py_2 core	0.10	5.32	9.72	<0.11	<2.0	<1.0	465000	56.79	879.95	38.92	1.63
524/85.5-C3-1	MA23A14	Py_2 core	2.41	238.15	264.27	0.40	<2.0	3.28	465000	1317.02	1254.99	604.59	77.51
156/286-4	MA23A66	Py_2 nodule	0.61	163.56	771.85	1.71	<2.0	<1.0	465000	14.28	58.59	105.37	2.20
Py_2 mean composition for n = 67			1.02	541.40	253.44	1.17	<2.0	18.26	standard	205.80	661.10	111.00	42.67
660-316.5	FE09A47	Py_3	0.05	13.16	459.91	0.66	2.74	<1.0	465000	1.10	27.42	8.58	0.46
156/135.5-C1-1	MA14A52	Py_3	0.17	<0.38	11.48	<0.1	2.30	<1.0	465000	1.99	624.64	2.86	2.20
C59/240-2-1	AP04A36	Py_3	0.05	1.42	5.07	<0.1	2.30	<1.0	465000	9.89	2371.21	1.80	1.04
C97/390.5-1a	AP04A81	Py_3	0.05	<0.55	3.15	<0.1	2.30	<1.0	465000	40.28	1256.67	1.80	2.20
524/70.9-1-1C	AP04A71	Py_3 core	0.11	93.62	113.15	0.29	2.30	<1.0	465000	203.31	2753.58	6.79	0.92
524/27-C1-1	MA14A39	Py_3 core	0.45	730.71	2834.92	4.09	3.68	<1.0	465000	251.27	1841.98	1972.69	50.10
156/225-C2-7	MA14A19	Py_3 core	0.05	1.01	18.21	<0.1	2.30	<1.0	465000	42.40	90.44	214.98	2.20
156/299-C3-2	MA23A59	Py_3 rim	0.21	0.55	6.86	<0.1	2.30	4.01	465000	8.21	379.12	2.72	2.20
156/490-C1-3	MA14A68	Py_3 core	47.37	<0.25	10.64	<0.1	2.30	<1.0	465000	25.66	242.99	504.73	980.81
Py_3 mean composition for n = 63			0.16	1246.46	610.67	3.22	6.42	11.43	standard	136.73	953.57	295.26	78.87
C97/390.5-5	AP04A85	Py_4	0.15	3568.46	1083.93	9.55	12.45	1.56	465000	35.77	108.35	9.50	4.93
SL-1-99.5a	FE09A33	Py_4	0.17	3545.73	1541.62	9.93	56.26	1.76	465000	2.64	4.78	20.07	4.21
156/55.5-1-1C	AP04A55	Py_4	0.28	1840.14	2649.34	5.44	6.64	26.84	465000	29.15	1516.17	55.33	13.28
524/22.5-C2-2	MA14A33	Py_4	0.39	1053.57	1446.01	3.07	5.23	1.16	465000	18.00	585.12	35.50	2.20
156/135.5-C2-2	MA14A57	Py_4 rim	0.05	2.47	412.52	0.37	2.99	1.00	465000	1.05	18.06	2.17	2.20
Py_4 mean composition for n = 44			0.25	1240.22	1472.38	3.97	13.74	3.43	standard	140.20	293.71	81.74	3.75
SL-1-99.5a	FE09A35	Py_5	<0.01	2.87	91.21	0.19	0.77	1.00	465000	494.57	193.07	0.49	0.34
660-541.5	FE09A56	Py_5	0.05	0.78	92.59	0.11	2.30	1.00	458000	359.86	1198.40	0.34	0.71
156/55.5-2-2R	AP04A60	Py_5	0.05	0.96	8.80	0.10	2.30	1.00	465000	0.11	489.55	1.80	2.20
156/490-C1-2	MA14A67	Py_5 rim to py_3	0.05	<0.30	8.78	0.10	2.30	1.00	465000	36.73	518.23	1.80	2.20
Py_5 mean composition for n = 13			0.07	132.68	50.54	0.36	2.82	9.04	standard	130.70	550.48	2.57	2.84
SL-1-90.6	FE21A83	Py_6	0.11	41.00	6.00	0.11	<0.01	32.43	465000	0.06	470.21	4.00	46.00
SL-1-90.6	FE21A88	Py_6	<0.04	14.00	3.00	<0.03	<0.02	89.73	465000	0.02	383.13	8.00	11.00
Py_6 mean composition for n = 6			0.10	183.17	14.00	0.10	0.11	92.56	standard	0.21	404.32	9.67	110.00
SL-1/99.6a-1-2	SE11A06	Pyrrhotite	<0.001	0.10	5.80	<0.1	0.20	0.00	635000	199.10	491.00	<0.1	1.00
SL-1/98.5c-3-1	SE11A11	Pyrrhotite	<0.001	569.00	53.90	0.50	0.10	1.30	635000	<0.01	516.80	17.60	2.80
C2/137-3-2	SE11A22	Pyrrhotite	0.01	318.60	74.50	0.40	1.00	0.70	635000	35.00	1603.40	0.10	1.10
1/90.6+92.5-2-1	SE11A23	Pyrrhotite	0.01	357.70	29.80	0.70	0.50	2.70	635000	<0.01	374.20	1.30	1.70
Pyrrhotite mean composition for n = 24			<0.001	226.91	58.21	0.44	0.35	0.75	standard	41.33	593.95	4.64	1.28
524/225_3	SE25A38	Arsenopyrite	2.52	619.49	1607.64	2.42	12.50	17.65	343000	44.03	103.33	1381.12	<2.14
524/225_5	SE25A40	Arsenopyrite	16.32	2178.63	1451.82	4.31	<6.59	75.89	343000	83.62	196.07	1201.60	9.06
156/299_3	SE25A20	Arsenopyrite	<0.10	100.94	47.74	<0.23	<7.66	<2.49	343000	<0.40	68.38	<4.53	<3.29
156/299_11	SE25A28	Arsenopyrite	1.45	<1.03	39.70	<0.24	<6.69	<3.08	343000	<0.53	24.67	<4.10	<4.48
1/87_#15_2b	JA24A94	Arsenopyrite	0.18	18.54	957.85	0.86	2.41	0.00	343000	20.33	548.85	0.40	1.56
176/77.5_2a	JA24A109	Arsenopyrite	1.98	103.99	584.55	0.40	1.07	1.48	343000	17.88	309.65	3.72	1.26
524/26.5_2a	JA24A137	Arsenopyrite	70.51	0.10	92.71	0.05	-0.96	-0.51	343000	0.20	12.57	2.43	0.47
Arsenopyrite mean composition for n = 43			5.12	795.58	259.11	0.94	8.44	16.12	standard	79.99	412.07	406	13.63
SL-1/95a-2	SE11A34	Matrix	<0.01	140000	2874.57	295.37	68.83	119.45	17028	0.72	5.46	1.95	26.59
SL-1/95a-4	SE11A36	Matrix	<0.01	140000	2924.19	314.45	83.94	101.12	18620	0.63	5.59	1.68	25.28
SL-1/102.2-1	SE07E05	Matrix	<0.01	57400	1256.35	113.67	88.75	6871.99	88905	6.04	33.68	90.58	512.64
SL-1/102.2-4	SE07E08	Matrix	<0.01	57400	1275.09	121.55	64.74	24.68	8019	2.34	37.26	8.05	29.78
Sediment matrix mean composition for n = 10			<0.01	standard	2000.00	200.00	72.00	830.00	21200	2.40	23.00	10.00	98.00

by Sediments from Within and Outside the Ore Zone of the Sukhoi Log Deposit

As (ppm)	Se (ppm)	Zr (ppm)	Mo (ppm)	Ag (ppm)	Sn (ppm)	Sb (ppm)	Te (ppm)	Ba (ppm)	La (ppm)	W (ppm)	Pt (ppm)	Tl (ppm)	Pb (ppm)	Bi (ppm)	Th (ppm)	U (ppm)
841.76	5.06	0.02	0.97	3.48	0.58	50.49	0.76	0.71	0.00	0.04	<0.022	0.05	134.29	2.94	<0.02	0.01
654.13	3.22	13.21	0.98	6.27	1.16	83.79	1.65	37.58	0.02	0.40	0.01	0.28	287.69	4.92	0.50	1.36
375.66	4.00	1.35	0.50	3.69	1.31	25.60	<1.18	18.58	0.07	0.13	<0.08	1.89	133.46	1.23	0.03	0.05
336.24	45.43	8.09	12.03	2.48	0.45	10.75	4.11	46.77	0.17	<0.23	<0.34	0.18	154.00	1.43	0.45	0.42
2136.30	4.00	3.41	36.62	7.08	1.37	30.13	<2.45	11.63	<0.03	<0.14	<0.07	0.13	261.57	3.83	0.09	0.16
13985.02	28.65	28.73	0.50	1.79	0.65	20.30	<0.35	3.55	0.11	13.41	<0.02	0.02	80.85	1.88	0.71	0.76
2419.62	27.58	4.20	6.88	21.17	1.92	74.23	2.87	118.26	0.03	0.67	<0.11	0.42	640.61	10.02	<0.01	0.05
3043.60	4.00	7.22	0.50	14.02	0.45	73.83	<16.44	668.63	4.50	<1.14	<1.01	0.64	590.65	20.08	0.21	0.47
1584.72	61.06	5.85	27.53	13.55	0.45	40.49	<3.64	594.92	0.31	0.48	<0.27	0.58	476.54	6.85	0.08	3.62
1902.85	12.46	13.59	14.80	9.26	1.32	53.42	1.52	157.78	0.27	1.40	<0.20	0.56	298.11	5.04	0.51	1.19
4292.90	16.71	<0.04	0.50	0.16	0.63	0.37	0.77	0.12	<0.01	<0.08	<0.06	0.02	1.20	0.02	<0.01	0.01
159.04	4.00	<0.32	0.50	0.16	0.45	2.82	<4.01	0.80	<0.05	<0.40	<0.23	0.02	32.48	0.82	0.11	0.10
5274.43	4.00	7.24	0.50	2.15	0.45	28.11	<8.04	2.98	0.23	1.15	<0.22	0.25	73.20	0.30	0.28	0.24
7534.10	28.10	6.09	111.31	0.35	0.92	4.53	<2.05	3.06	0.25	0.42	0.04	0.23	16.51	0.14	0.30	0.22
703.63	10.12	<0.12	0.50	0.72	0.45	0.14	<0.90	<0.10	<0.07	<0.14	<0.13	0.02	17.82	0.22	<0.04	0.01
1933.55	50.87	0.27	0.22	0.16	0.75	1.94	<0.51	1.00	<0.01	<0.03	<0.05	0.02	4.90	0.05	0.01	0.02
1491.40	27.50	276.75	9.32	9.45	1.24	176.81	<2.01	4.94	10.69	0.73	<0.21	0.58	210.14	1.64	3.12	4.15
3357.66	16.95	7.61	0.50	1.00	0.74	4.13	<1.81	13.48	0.56	0.24	<0.01	0.25	13.98	0.22	0.23	0.23
4263.72	25.76	11.72	10.14	1.37	0.88	8.72	0.51	7.30	1.00	1.76	<0.20	0.73	113.99	0.53	0.39	0.20
63.90	3.81	9.89	0.04	0.17	0.78	0.41	1.02	0.11	0.01	0.86	0.00	<0.02	5.54	1.56	0.08	0.17
4672.51	38.78	<0.02	1.81	0.58	0.76	0.98	<0.90	<0.12	<0.01	0.05	<0.04	<0.02	6.35	0.08	<0.01	0.01
2491.44	50.03	0.14	<0.5	0.16	0.45	0.14	<0.90	<0.12	<0.01	<0.03	<0.03	<0.02	0.04	0.02	<0.01	0.01
3397.21	8.82	<0.06	<0.5	0.46	0.86	0.43	<0.90	<0.12	<0.02	0.04	<0.09	<0.02	2.82	0.53	<0.02	0.01
5014.29	13.04	2.78	<0.5	0.26	0.20	3.61	<0.90	1.02	<0.00	0.40	<0.01	<0.02	13.50	0.30	0.07	0.07
4165.34	19.56	16.60	<0.5	2.19	1.40	14.22	<0.90	11.56	0.18	10.95	0.01	<0.02	70.73	0.65	0.45	0.41
73.44	4.00	<0.03	<0.5	0.16	0.98	0.14	1.36	<0.12	0.02	<0.10	<0.08	<0.02	1.76	0.03	<0.01	0.01
3908.35	15.49	0.05	<0.5	0.19	0.93	0.98	<0.90	<0.12	<0.02	<0.07	<0.07	<0.02	4.43	0.02	<0.01	0.02
17743.46	72.71	<0.02	<0.5	5.82	1.02	27.32	<0.54	<0.12	<0.01	<0.02	<0.02	<0.02	97.22	0.85	<0.01	0.01
2891.63	17.42	16.68	5.22	1.32	1.07	5.72	1.16	6.90	1.23	1.60	<0.1	<0.02	130.81	2.22	0.02	0.33
2354.86	11.61	17.11	0.50	3.18	1.89	18.37	6.32	21.58	0.03	0.80	<0.03	0.17	80.09	9.28	0.29	0.39
1363.61	3.74	68.22	6.83	2.32	1.03	62.17	1.32	18.18	0.09	4.12	<0.028	0.09	167.66	4.49	0.36	1.40
3649.00	16.90	38.45	0.29	1.20	0.64	27.92	<0.90	10.66	4.86	5.82	<0.02	<0.02	92.94	2.44	1.28	1.04
2262.91	5.79	5.62	0.50	0.37	1.60	8.73	<0.90	16.97	<0.02	4.38	<0.03	<0.02	46.51	0.47	1.16	1.00
2756.27	31.69	3.76	0.50	0.16	1.08	0.53	<0.90	0.08	<0.01	0.76	<0.03	0.02	3.05	0.02	0.03	0.06
2268.01	17.97	55.64	1.06	1.40	0.93	18.22	2.35	10.37	0.67	2.26	<0.03	0.06	164.49	8.82	2.22	1.20
2941.72	6.74	1.02	0.07	0.16	0.82	0.27	<0.50	0.12	0.01	0.52	0.01	<0.02	1.02	<0.02	0.05	0.07
5083.88	17.64	1.27	0.01	0.05	1.01	0.11	<0.17	<0.12	<0.01	0.07	<0.05	<0.02	1.86	0.19	0.02	0.01
1849.08	26.75	0.04	0.50	0.16	0.47	0.14	<0.55	<0.12	<0.10	<0.05	<0.05	<0.02	0.11	<0.02	<0.01	0.01
4315.65	58.98	<0.04	0.50	0.16	0.85	0.14	<0.65	<0.12	<0.01	<0.06	<0.04	<0.02	0.17	<0.02	<0.00	0.01
2897.14	16.30	4.01	0.40	0.29	0.63	4.33	0.49	1.14	0.01	0.28	<0.05	<0.02	13.06	0.42	0.04	0.08
7.00	9.55	8.83	1.27	0.61	0.88	13.91	<0.04	2.13	0.03	2.19	<0.05	0.01	62.00	<0.10	0.23	2.16
3.00	10.82	6.15	0.29	0.34	1.14	1.60	0.05	2.12	0.02	0.81	0.01	0.03	4.00	<0.10	0.02	0.72
8.83	8.37	7.06	1.44	0.85	0.86	13.90	0.01	2.85	0.06	2.19	<0.05	0.03	43.17	<0.10	0.16	1.91
0.30	8.50	0.00	<0.1	0.70	0.80	0.00	0.20	<0.12	<0.10	<0.10	<0.05	<0.02	0.30	<0.10	<0.01	<0.10
0.20	5.70	1.40	<0.1	1.10	0.60	0.10	<0.1	0.90	0.10	0.10	<0.05	<0.02	3.50	<0.10	<0.01	0.10
0.50	7.50	35.50	<0.1	0.60	1.60	1.90	0.40	4.80	4.20	0.30	<0.05	<0.02	3.70	0.10	0.90	0.90
0.60	8.10	1.60	<0.1	1.90	1.40	2.40	0.20	4.00	<0.10	0.10	<0.05	<0.02	29.60	0.10	<0.01	0.10
0.18	7.48	3.75	<0.1	1.21	1.09	0.90	0.13	1.80	0.25	0.10	<0.05	<0.02	32.86	0.10	<0.01	0.18
nd	127.85	13.81	<5.61	<0.67	<2.44	278.75	<7.79	8.44	<0.07	7.93	<0.34	<0.13	122.40	3.63	0.38	0.24
nd	73.75	29.35	<4.14	<0.67	<3.02	101.27	<11.23	33.58	<0.07	8.78	<0.24	<0.10	110.50	1.75	0.55	0.48
nd	117.37	<0.19	<4.38	<0.42	<1.88	89.21	<5.48	<0.55	<0.08	<0.37	<0.60	<0.11	11.20	<0.10	<0.06	<0.05
nd	<10.67	0.52	<5.34	<0.80	<3.00	91.63	<11.91	1.54	<0.09	0.87	<0.52	<0.09	1.13	<0.17	0.28	<0.05
nd	9.43	93.86	2.90	0.41	0.41	65.43	2.35	0.12	0.04	1.74	0.05	0.00	14.88	3.32	1.01	3.00
nd	169.51	2.67	0.08	0.99	0.26	111.56	0.41	0.14	0.03	0.81	0.05	0.02	13.54	0.66	0.05	0.05
nd	198.67	3.49	0.37	0.07	0.19	103.93	2.80	0.01	0.01	0.52	0.02	<0.01	1.12	0.05	0.11	0.02
nd	114.45	9.45	9.15	2.17	1.94	130.54	8.12	4.28	0.27	1.36	0.28	0.12	32.18	1.13	0.14	0.26
8.87	0.57	209.58	<0.05	0.11	5.39	2.61	<0.1	1097.17	1.82	12.31	<0.05	2.96	5.55	0.05	14.69	25.56
8.78	0.50	377.68	0.07	0.12	6.19	2.71	<0.1	1200.54	1.92	13.01	<0.05	2.96	6.67	0.04	24.39	39.56
6.29	2.04	70.35	9.18	0.85	3.50	5.66	<0.1	381.27	71.60	5.84	<0.05	0.99	14.64	1.02	10.36	37.56
1.30	1.43	35.14	7.95	0.49	3.20	2.82	<0.1	397.47	0.43	5.56	<0.05	0.98	92.89	0.74	0.68	1.42
5.90	0.90	140.00	2.40	0.33	4.20	3.20	<0.90	725.00	7.80	8.50	<0.05	1.90	19.00	0.40	13.40	18.00

TABLE 2. Selected LA-ICPMS Analyses of Pyrite and Arsenopyrite from Bedding-Parallel Pyrite-Quartz Veinlets in the Ore Zone of the Sukhoi Log Deposit

Sample no.	Analysis no.	Py type	Au (ppm)	Al (ppm)	Ti (ppm)	V (ppm)	Cr (ppm)	Mn (ppm)	Fe (ppm)	Co (ppm)	Ni (ppm)	Cu (ppm)	Zn (ppm)	As (ppm)
SLK1-2	OC17A16	Py_3 core	2.30	593.90	871.48	2.28	3.96	<0.30	465000	73.63	5067.69	171.07	405.40	16127.40
SLK1-3	OC17A17	Py_3 core	0.24	48.01	163.97	0.28	1.36	<0.29	465000	7.68	3051.76	2141.91	198.67	11918.59
SLK1-4	OC17A18	Py_5 rim	0.09	17.82	123.93	0.21	<0.71	<0.36	465000	1161.26	770.34	1.76	0.81	3046.54
SLK1-5	OC17A19	Py_5 rim	0.13	0.12	8.03	<0.03	<0.47	<0.33	465000	9.84	219.28	<0.59	1.18	4413.86
SLK1C	SE25A10	Aspy in core	0.08	457.83	254.19	0.96	<1.85	<0.64	343000	3960.47	6911.61	31.07	47.96	nd
SLW1-16	OC17A60	Py_3 inner core	0.19	49.52	84.27	0.18	0.85	<0.37	465000	191.78	98.38	2.51	0.73	4367.02
SLW1-17	OC17A61	Py_4 outer core	0.85	94.30	955.55	1.03	2.19	<0.34	465000	32.71	159.07	9.60	1.26	7379.55
SLW1-20	OC17A64	Py_5 rim	<0.03	0.43	6.56	<0.03	<0.74	<0.39	465000	177.30	64.07	<1.09	0.89	411.81
SLW1D	SE25A14	Aspy in core	0.36	37.18	42.64	<0.20	<7.87	<2.19	343000	17711.97	11712.90	<5.61	1883.00	nd
SLW3-5	OC17A08	Py_3 inner core	0.32	54.84	334.49	0.37	2.60	<0.27	465000	7.73	2112.79	1739.21	138.64	10346.93
SLW3-7	OC17A10	Py_4 outer core	0.84	220.11	3367.77	3.62	9.44	<0.29	465000	12.55	264.12	13.48	1.69	7776.05
SLW3-10	OC17A13	Py_5 rim	0.12	0.41	144.73	0.15	0.65	<0.35	465000	12.38	148.55	<0.71	0.82	4560.35
SLW5-10	OC17A35	Py_3 core	0.58	237.25	235.15	0.75	1.19	0.36	465000	124.25	3033.72	48.87	43.34	11488.98
SLW5-8	OC17A33	Py_5 rim	<0.03	0.67	810.60	0.83	2.34	<0.34	465000	0.84	147.20	0.83	0.68	2217.35
SLW5	SE25A06	Aspy in core	<0.11	<0.80	<2.48	<0.18	<7.04	<1.83	343000	2279.45	7130.49	<3.82	<3.28	nd
1-4-2 C	FE09A04	Py_4 core	77.15	nd	6642.78	nd	26.83	0.84	465000	346.00	1217.39	21.69	2.30	2095.45
1-4-3 C	FE09A05	Py_4 core	231.10	nd	2962.42	nd	14.34	0.50	465000	678.60	1026.78	196.87	1.15	2080.27
1-4-4 R	FE09A06	Py_5 rim	0.83	nd	39.15	nd	<1.03	0.88	465000	4.28	56.30	<0.85	<0.60	321.97
1-4-5 R	FE09A07	Py_5 rim	<0.05	nd	10.57	nd	<1.11	<0.54	465000	57.30	258.53	<0.81	0.63	544.74
1-4-6 C	FE09A08	Py_4 core	289.03	nd	3428.19	nd	14.29	<0.43	465000	1016.39	954.02	31.90	1.78	1777.20
1-4-7 C	FE09A09	Py_4 core	348.64	nd	7260.47	nd	28.61	1.48	465000	572.92	990.97	184.87	2.53	1771.73
1-4-8 C	FE09A10	Py_4 core	223.02	nd	5787.39	nd	22.32	<0.45	465000	443.97	1079.89	116.64	2.22	1690.16
1-4-9 C	FE09A11	Py_4 core	5.66	nd	2540.71	nd	10.70	<0.49	465000	90.70	796.00	13.93	2.01	1528.69
1-4-10 R	FE09A12	Py_5 rim	<0.05	nd	10.51	nd	<0.99	<0.55	465000	102.47	73.40	<0.86	1.02	515.83

TABLE 2. *(Cont.)*

Sample no.	Se (ppm)	Zr (ppm)	Mo (ppm)	Ag (ppm)	Sn (ppm)	Sb (ppm)	Te (ppm)	Ba (ppm)	La (ppm)	W (ppm)	Pt (ppm)	Tl (ppm)	Pb (ppm)	Bi (ppm)	Th (ppm)	U (ppm)
SLK1-2	34.63	52.23	<0.17	123.40	1.01	4.19	5.12	3.19	0.20	0.86	<0.02	0.02	13872.09	248.76	1.74	3.29
SLK1-3	18.11	18.09	<0.14	51.79	1.18	2.26	1.10	0.28	0.22	0.21	<0.03	<0.02	7903.16	99.76	0.11	0.18
SLK1-4	17.00	0.92	0.17	0.25	0.97	0.41	1.06	0.09	<0.01	0.26	<0.02	<0.02	6.82	0.69	0.03	0.03
SLK1-5	32.75	0.02	<0.19	<0.06	0.95	<0.05	<0.60	0.03	<0.00	<0.03	<0.02	<0.02	0.42	0.08	<0.00	<0.00
SLK1C	31.91	10.19	<0.93	0.63	<0.58	22.61	<1.08	2.87	<0.02	<0.10	<0.06	<0.02	34.75	4.26	0.50	0.85
SLW1-16	13.22	1.69	<0.21	0.45	0.91	0.64	<0.78	0.42	0.01	0.12	<0.02	<0.02	15.48	2.44	0.04	0.05
SLW1-17	14.99	16.94	<0.19	0.64	0.76	3.76	1.49	0.17	0.09	1.01	<0.03	<0.02	45.31	12.75	0.48	0.36
SLW1-20	5.87	<0.02	<0.24	0.08	0.74	<0.08	<0.64	<0.05	<0.00	<0.03	<0.05	<0.02	0.03	<0.01	<0.00	<0.01
SLW1D	42.28	35.01	<6.41	<0.51	<1.57	68.04	<11.14	<0.69	<0.11	<0.55	<0.86	<0.12	28.90	23.82	0.92	0.72
SLW3-5	18.88	2.30	<0.17	57.53	0.80	2.30	<0.31	0.30	0.01	0.63	<0.02	<0.02	8557.70	119.53	0.06	0.05
SLW3-7	22.58	58.72	<0.19	0.68	0.83	3.67	<0.52	0.71	0.14	2.84	<0.03	<0.02	73.21	15.92	1.05	1.15
SLW3-10	27.19	23.91	<0.17	<0.07	0.62	0.07	<0.44	<0.04	<0.01	0.24	<0.02	<0.02	1.87	0.26	0.09	0.24
SLW5-10	14.72	1.95	<0.20	51.01	0.75	6.22	6.12	0.71	0.02	0.26	<0.02	0.02	9678.67	109.78	0.06	0.11
SLW5-8	27.22	88.68	<0.15	0.09	0.55	0.27	<0.52	<0.06	0.02	0.68	<0.02	<0.02	5.76	0.43	0.67	1.25
SLW5	66.62	0.62	<5.71	<0.61	<2.64	107.66	<7.89	<0.51	<0.05	<0.28	<0.39	<0.16	9.05	6.65	<0.06	<0.06
1-4-2 C	9.21	nd	<0.19	102.36	nd	16.32	154.42	nd	nd	9.80	<0.04	0.14	125.58	23.64	nd	nd
1-4-3 C	9.16	nd	<0.22	421.33	nd	32.02	481.66	nd	nd	2.42	<0.04	0.29	302.19	51.21	nd	nd
1-4-4 R	7.51	nd	<0.26	1.06	nd	0.12	1.29	nd	nd	<0.04	<0.06	0.11	0.75	0.13	nd	nd
1-4-5 R	5.14	nd	<0.28	<0.07	nd	<0.05	<0.36	nd	nd	<0.04	<0.03	<0.01	0.19	<0.01	nd	nd
1-4-6 C	7.72	nd	<0.18	465.95	nd	20.20	494.74	nd	nd	2.42	<0.05	0.21	523.07	38.40	nd	nd
1-4-7 C	9.07	nd	<0.19	656.71	nd	24.06	671.24	nd	nd	7.15	<0.04	0.16	711.94	43.32	nd	nd
1-4-8 C	7.70	nd	<0.22	409.90	nd	26.87	439.10	nd	nd	4.50	<0.03	0.25	378.59	43.33	nd	nd
1-4-9 C	9.29	nd	<0.31	9.70	nd	35.54	74.10	nd	nd	1.85	<0.05	0.31	72.40	35.29	nd	nd
1-4-10 R	6.03	nd	<0.26	<0.08	nd	<0.04	<0.43	nd	nd	<0.04	<0.05	<0.01	<0.02	<0.01	nd	nd

Note: nd = not determined

TABLE 3. Summary of Common Textures, Gold Content, and Timing for Main Sulfide Types at Sukhoi Log

Sulfide type	Texture	Gold content	Interpretation of timing	Evidence for timing
Py_1	Fine-grained stratiform, microeuhedral, framboidal and sooty	Invisible gold Range: 0.44–12.10 ppm Mean: 3.32 ppm Free gold: none	Synsedimentary	Overgrown by all later pyrite types; py_1 layers folded by main deformation; stratiform texture similar to syngenetic pyrite in SEDEX Zn-Pb-Ag deposits
Py_2	Bedding-parallel fine-grained euhedral cubes	Invisible gold Range: 0.02–13.00 ppm Mean: 1.02 ppm Free gold: none	Syndiagenetic	Intimately related to py_1; bedding parallel; overgrows py_1 and is overgrown by arsenopyrite, py_3, py_4, and siderite porphyroblasts
Arsenopyrite	Corroded subhedral	Invisible gold Range: <0.1–70.5 ppm Mean: 5.12 ppm Free gold: none	Syndiagenetic	Overgrows py_1 and py_2 and is overgrown and corroded by py_3, py_4, and py_5
Py_3	Coarse-grained anhedral to subhedral; abundant unaligned sediment matrix inclusions	Invisible gold Range: 0.05–0.80 ppm Mean: 0.16 ppm Free gold: common as inclusions	Late-diagenetic and/or synearliest deformation; dominantly pre-main cleavage	Randomly oriented sediment matrix inclusions; overgrows weak compaction or early tectonic fabric; overgrows py_2 and arsenopyrite and is overgrown by py_4 and py_5
Py_4	Coarse-grained euhedral; aligned inclusions define an internal fabric	Invisible gold Range: 0.02–1.30 ppm Mean: 0.25 ppm Free gold: may be present as inclusions	Syndeformation but post-main cleavage	Overprints main tectonic fabric in the shale; overgrows py_3 and is overgrown by py_5
Py_5	Coarse-grained euhedral; clear and inclusion-free	Invisible gold Range: <0.01–0.22 ppm Mean: 0.07 ppm Free gold; uncommon	Syn-late deformation; syn-main stage folding but post-main cleavage	Overgrows py_4, which overgrows the main tectonic fabric; overgrown by fibrous quartz in py_5 pressure shadows
Py_6	Porous and colloform with a "birds-eye" texture	Invisible gold Range: <0.04–0.15 ppm Mean: 0.10 ppm Free gold; none	Post-deformation	Replaces pyrrhotite adjacent to postdeformation late-stage milky-white quartz veins

indicates that py_4 has overgrown the main cleavage and has a syndeformation timing. Folding of the main fabric has been preserved within some py_4 crystals, suggesting a locally complex deformation history (Fig. 10c). Minor pyrrhotite, sphalerite, chalcopyrite, and native gold occur as inclusions in py_4.

Pyrite 5

Py_5 is a homogeneous, featureless type of pyrite, with few inclusions, that overgrows py_3 and py_4 (Fig. 10c, d). It is the dominant pyrite type in the pyrite-quartz veinlets (Fig. 11), as discussed in more detail below. The fact that py_5 overgrows the syndeformation py_4, but shows no internal tectonic fabric itself, suggests that it formed during later stages of deformation, possibly by recrystallization of earlier types of pyrite.

Pyrite 6

Py_6 is a porous and colloform style that replaces pyrrhotite along fractures and late stage milky-white quartz veins or along the margins of pyrrhotite grains (Fig. 10e). It is rare compared to the other types of pyrite and is interpreted to be related to oxidation of pyrrhotite during the late-stage development of barren milky-white quartz veins.

Pyrite nodules

Three types of pyrite-bearing nodules are present in the sedimentary rocks at Sukhoi Log. The first type consists of spherical massive pyrite nodules from 5 to 20 mm across with fibrous quartz strain fringes (Fig. 6f). These are typically composed of py_2, with minor py_1, and contain abundant silicate inclusions. Many of the py_2 grains that make up the nodules show porous cores of recrystallized py_1. These nodules probably formed during diagenesis and underwent partial recrystallization during deformation.

The second type consists of large rounded to oval-shaped aggregates of py_3 and py_4 which measure up to 50 to 100 mm across (Fig. 6g; Wood and Popov, 2006, fig. 8). These may have initially formed as early diagenetic pyrite nodules but are now commonly composed of aggregates of late diagenetic and metamorphic pyrite (py_3 and py_4). Finally, the third style of nodule is small oval-shaped siliceous bodies (0.4–0.6 mm long) consisting of a pyrite core, surrounded by quartz, with inclusions of pyrrhotite, and a narrow outer rim of rutile (Fig. 10f). These nodules are aligned (flattened?) parallel to cleavage and are interpreted to be a diagenetic feature modified by deformation.

Pyrite in pyrite-quartz veinlets and aggregates

Pyrite within these veinlets tends to occur as a central band fringed by fibrous quartz, (Fig. 5e) and commonly forms zoned euhedral aggregates, 3 to 20 mm across (Figs. 5b, e, 6a), with a core of inclusion-rich py_3 surrounded by clear py_5. Observed variations in internal textures of the pyrite aggregates

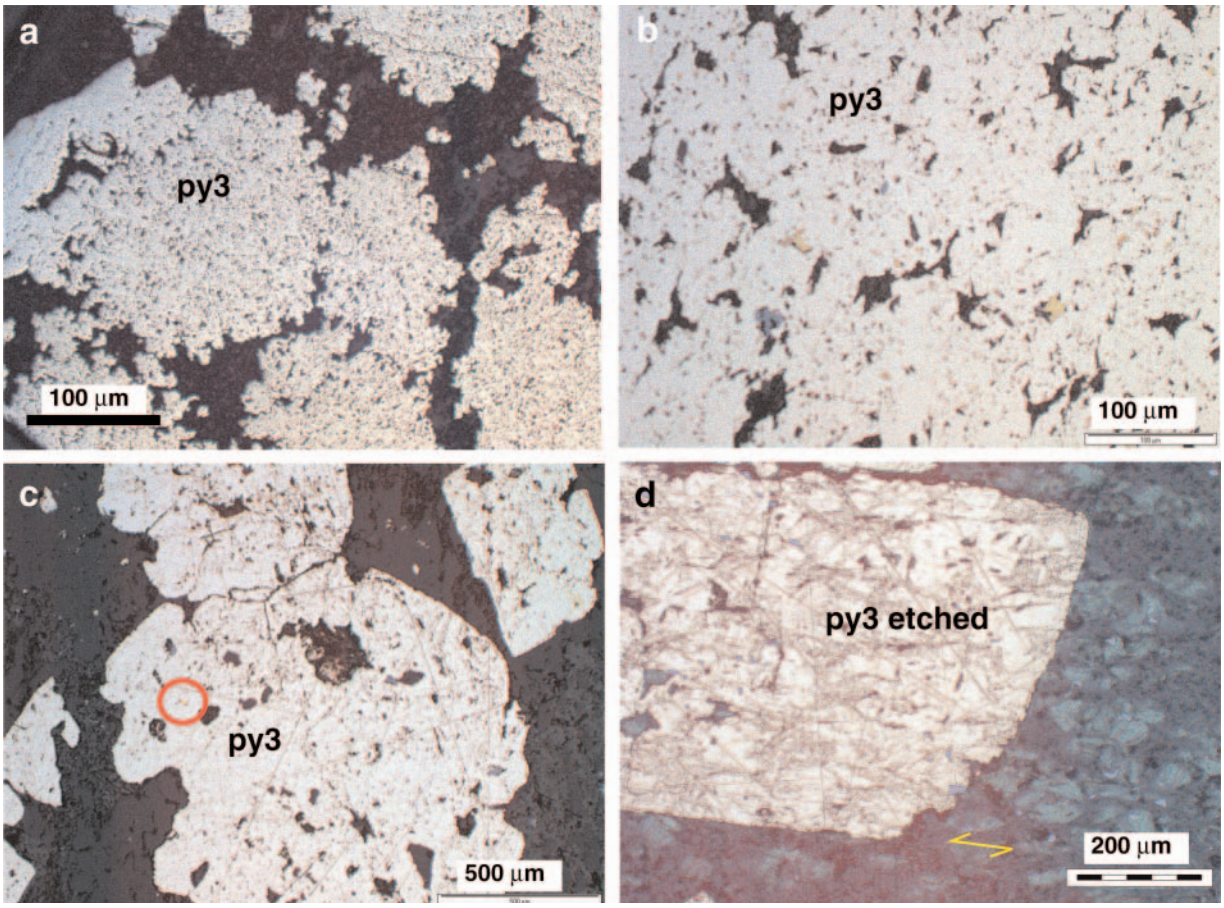

FIG. 9. Textures of py_3. a. Anhedral py_3 aggregates within sandstone layer. b. Py_3 with randomly oriented inclusions of silicate minerals (black), chalcopyrite (yellow), and sphalerite (gray). c. Py_3 with inclusions of native gold (in red circle), silicates (black), sphalerite (gray), and pyrrhotite (brown). d. Py_3 etched with nitric acid, showing the internal texture of the pyrite which is preserving the quartz grain shapes in the host sandstone. This demonstrates that py_3 is overgrowing and replacing the sandstone fabric.

include a core of broken and corroded crystals of arsenopyrite surrounded by py_3 with a rim of py_5 (Fig. 11a-c, e), a core of py_3 surrounded by py_4, itself rimmed by inclusion-free py_5 (Fig. 11d), and commonly a core of inclusion-rich py_4 surrounded by py_5 (Fig. 11f). In all cases the same paragenetic sequence is observed from core to rim: arsenopyrite → py_3 → py_4 → py_5, although not all sulfide types are necessarily present within any given euhedral aggregate. In addition, in most folded pyrite-quartz veinlets the zoned pyrite euhedra are fractured or brecciated. Quartz fibers are observed to overgrow py_3, py_4, and py_5.

The ubiquitous presence of syndiagenetic to mainly precleavage py_3 and syncleavage py_4 in the cores of the pyrite aggegates within these veinlets, as well as textures indicative of host sedimentary rock replacement, suggests that the pyrite grew along favorable compositional bands in the black shale host rocks. These sulfides were subsequently overgrown by py_5 and by quartz fibers during ongoing folding and cleavage development to produce the bedding-parallel pyrite-quartz veinlets. These textural and paragenetic relationships between pyrite and quartz fibers support the previous conclusions about the formation of the veinlets based on the underground mapping. The cores of some of the pyrite aggregates have textures indicative of diagenetic nodules (Fig. 11e), suggesting that the metamorphic pyrite may have nucleated on, or recrystallized from, preexisting nodular diagenetic pyrite. Native gold, along with pyrrhotite, galena, sphalerite, and chalcopyrite, commonly occurs as inclusions, in py_3 cores, or less commonly along cracks or growth zones within py_5 (Fig. 12).

Pyrrhotite

Minor amounts of pyrrhotite occur throughout the orebody (0–2 vol %), mainly as inclusions within the late diagenetic and metamorphic pyrite generations, py_3 and py_4 (Fig. 9b-c). Pyrrhotite is commonly associated with minor sphalerite, chalcopyrite, and in some cases, arsenopyrite. Banded disseminated pyrrhotite, up to 10 vol percent (Fig. 5e), is common in drill holes C1 and C2 where, based on similarities in texture, grain size, and distribution, it is interpreted to have formed by the replacement of stratiform py_1 (Fig. 10d).

Arsenopyrite

Arsenopyrite is not common at Sukhoi Log but was observed as disseminated acicular crystals, 2 to 10 mm long, within siltstone and sandstone beds in some drill holes. Based

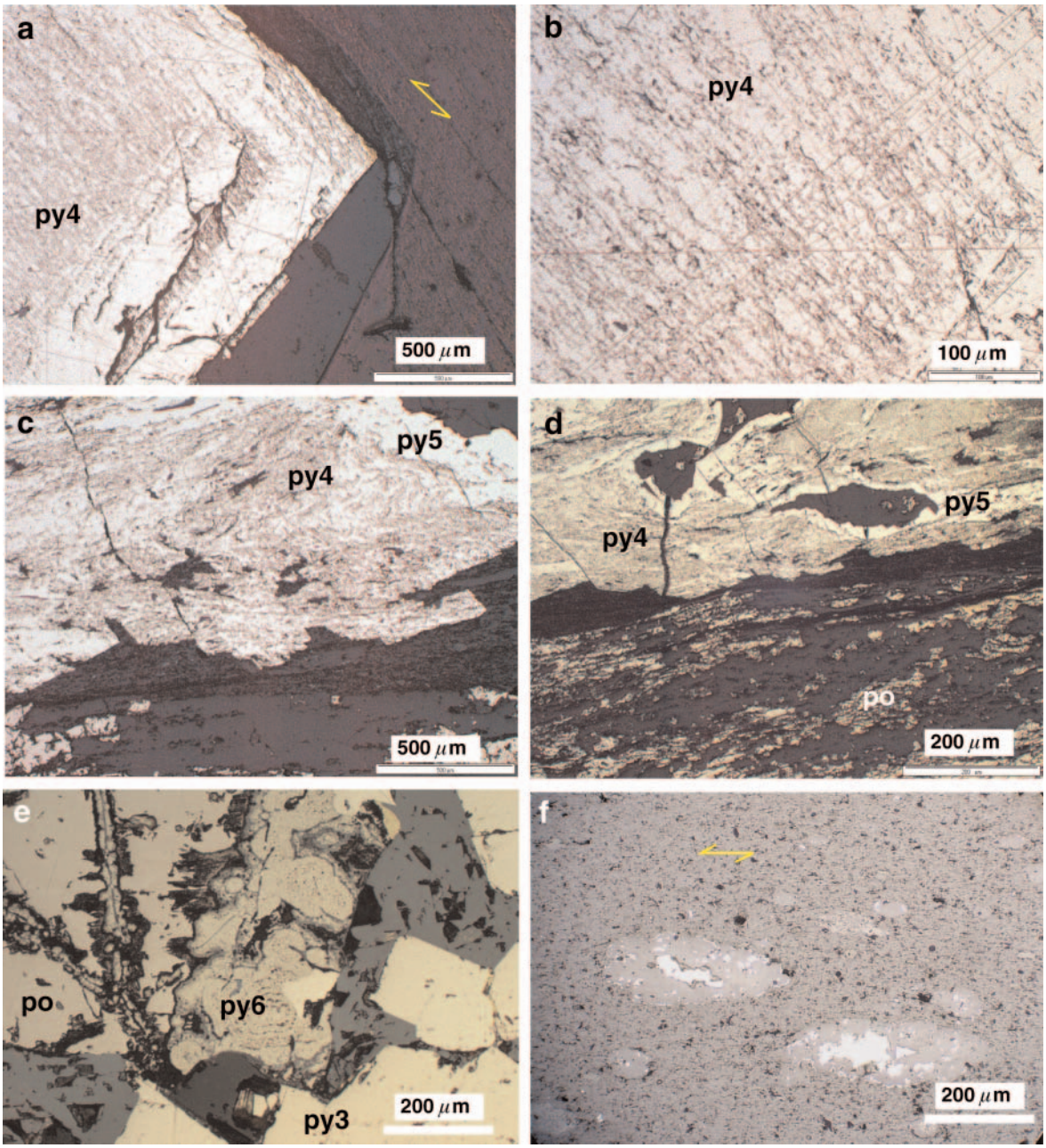

FIG. 10. Textures of py_4, py_5, py_6 and nodules. a. Euhedral py4 in shale, etched with nitric acid, showing internal fabric and growth zoning. b. Close-up of internal fabric in py_4, demonstrating that py_4 overgrows the metamorphic fabric in the host shale. c. Etched py_4 showing folded internal metamorphic shale fabric replaced by pyrite. Clear py_5 overgrows py_4. d. Py_4 with internal texture preserved and rimmed by clear py_5. Fine pyrrhotite replacing py_1 occurs in the sediment matrix. e. Birds-eye texture in py_6 indicative of late-stage pyrite replacing pyrrhotite. f. Deformed siliceous nodules in shale, with cores of pyrite and narrow rims of rutile.

on observations in drill holes C1 and C2, the arsenopyrite shows maximum concentration (up to 2 vol %) in siderite-altered sandstones on the margins of the pyritic mineralized zones. Corroded and broken crystals of arsenopyrite are also present in the py_3 cores of pyrite aggregates within the bedding-parallel pyrite-quartz veinlets (Fig. 11b, e). Two generations of arsenopyrite were identified in polished section—an early form ($aspy_1$) that overgrows py_1 and py_2 and is, in turn, corroded and overgrown by py_3 and py_4 (Fig. 11b, g, h), and a later, less common, form of acicular euhedral crystals ($aspy_2$) that appear to overprint the main cleavage.

Sulfide and Gold Paragenesis

Overprinting and overgrowing relationships define a clear paragenetic succession for the various styles and stages of pyrite (Fig. 13, Table 3) and for their relationship to quartz fibers, arsenopyrite, siderite, and pyrrhotite. This paragenetic sequence can be divided into three main stages of

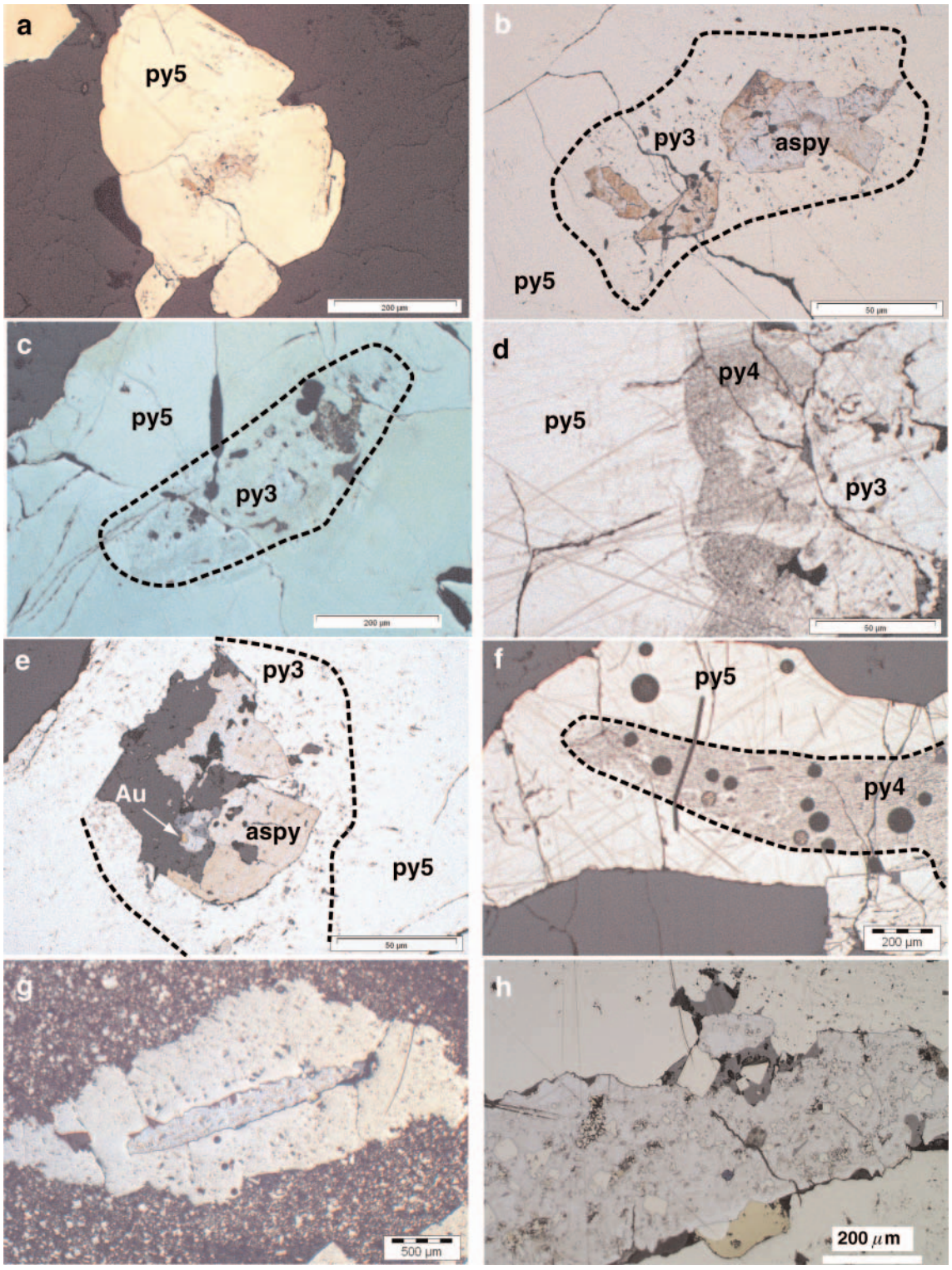

FIG. 11. Textures of pyrite and arsenopyrite in bedding-parallel pyrite-quartz veinlets (a-f). a. Euhedral py_5 with core of py_3 and arsenopyrite. b. Close-up on py_5 core, etched with nitric acid, shows corroded crystals of arsenopyrite (aspy) surrounded by inclusion-rich py_3, surrounded by clear py_5. c. Clear py_5 euhedra with inclusion-rich core of py_3. d. Zonation from core (RHS) to rim (LHS) in large euhedral pyrite, showing the textural variation in py_3 (core), py_4, and py_5 (rim). e. Subhedral py_5 with a composite core of corroded arsenopyrite (aspy), silicate (dark gray), sphalerite (light gray), and native gold surrounded by inclusion-rich py_3. f. Py_5 in quartz vein, with core of py_4 showing well-developed internal metamorphic fabric inherited from shale host rocks; the round black spots are laser burns. g. Corroded acicular crystal of arsenopyrite (white) overgrown and surrounded by py_3 within black shale host rock containing fine-grained py_2 and py_1. h. Close-up of corroded arsenopyrite crystal, showing that it has overgrown fine-grained sooty py_1 and euhedral py_2 within the shale.

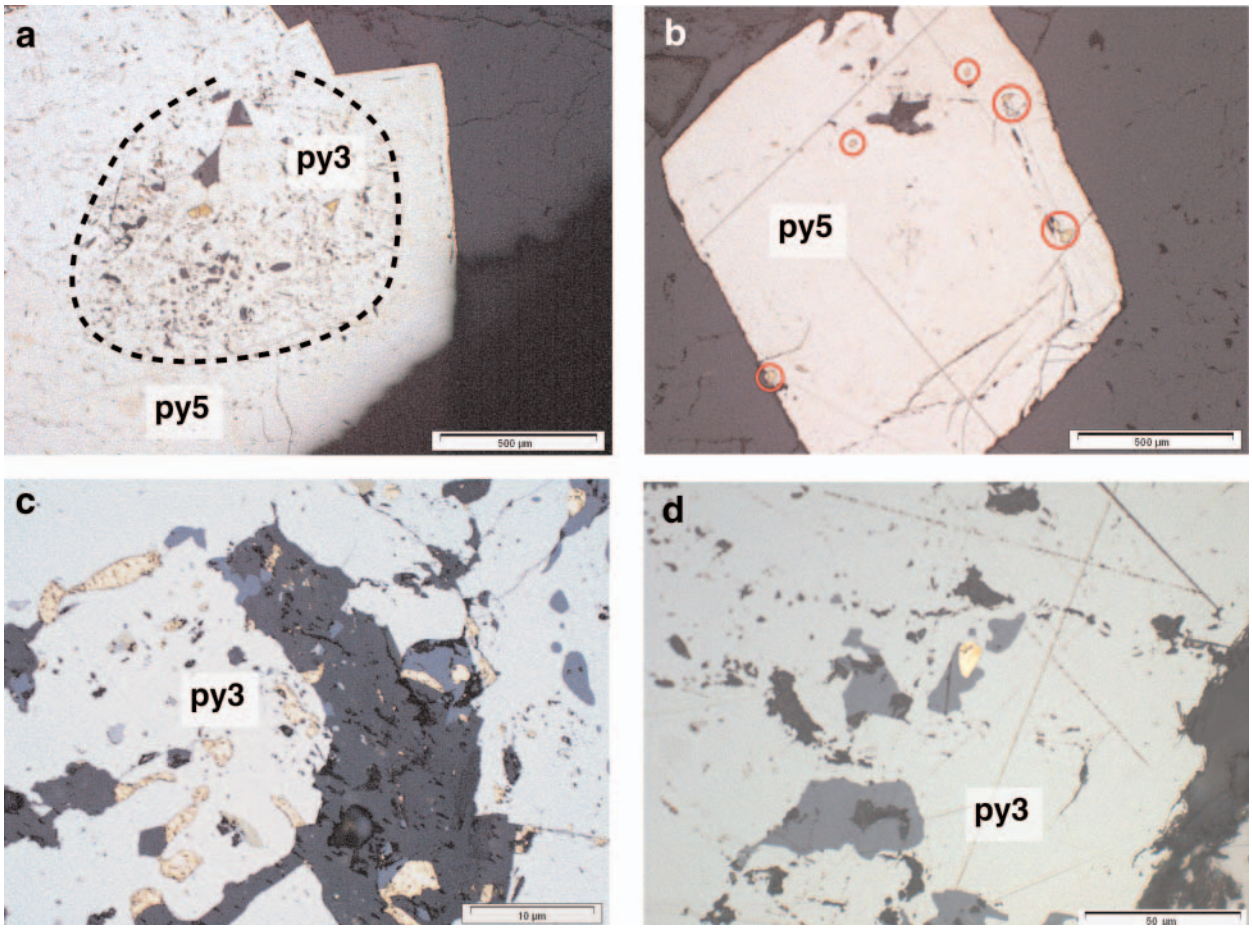

FIG. 12. Textural associations of native gold. a. Euhedral py_5 with core of py_3 containing inclusions of native gold (yellow) and silicates (black). b. Euhedral py_5 with inclusions of native gold (in red circles). c. Abundant native gold inclusions (10–50 μm across) in py_3. d. Native gold and sphalerite inclusions in py_3.

development: sedimentation and diagenesis, metamorphism and deformation, and postdeformation (Fig. 14).

Sulfides formed during sedimentation and diagenesis

Fine grained py_1 (stratiform, framboidal, and sooty pyrite) is the earliest generation of pyrite and most probably developed during early sedimentation. It is also possible that py_1 developed during early diagenesis but clear supporting evidence is lacking. Py_2 surrounds, overgrows and, in some cases, replaces py_1 (Figs. 8d, f, 13a, b). Py_2 may have porous cores, which are crystallized forms of either framboidal or sooty py_1 (Fig. 8f). The fine-grained nature of py_2, its intimate relationship to py_1 (Fig. 8d, e), and its concentration in the finer black shale beds, suggests that it formed during diagenesis (Table 3).

Py_3 overgrows py_1 and py_2 (Fig. 13a, b). It also contains abundant unoriented inclusions of the host rock (Fig. 9a-c) and overgrows and preserves the texture of the siltstone host (Fig. 9d), indicating py_3 formed by replacement of the sedimentary rock. These features are observed in py_3 hosted by siltstone and in the cores of pyrite aggregates in the pyrite-quartz veinlets. In most cases, the sedimentary texture preserved by py_3 does not show a preferred mineral orientation, indicating that py_3 grew before the main cleavage development, probably during late diagenesis. However, in other cases (Fig. 9d), a weak fabric is revealed by etching, indicating that some py_3 grew during early cleavage development. Py_3 within the pyrite-quartz veinlets, and some py_3 within the sedimentary rocks, contains relict corroded crystals of arsenopyrite (Fig. 11a-b, e, g). The fact that the arsenopyrite overgrows py_1 and py_2 but is, in turn, overgrown by py_3 indicates that the arsenopyrite formed prior to cleavage development, possibly during late diagenesis.

Sulfides formed during deformation

The coarse euhedral py_4 overgrows and preserves the main cleavage in the sedimentary rocks (Fig. 10a-c), indicating syndeformation growth, consistent with the local presence of incipient pressure shadows. Py_4 also overgrows late diagenetic py_3 in the zoned pyrite euhedra within the bedding parallel pyrite-quartz veinlets (Fig. 11d). Siderite porphyroblasts overgrow py_1 and py_2 but not py_3 or py_4. They probably formed contemporaneously with py_4 during the main metamorphic event. Some siderite porphyroblasts have poorly defined cores that may indicate an earlier diagenetic siderite has been overgrown by metamorphic siderite. Clear,

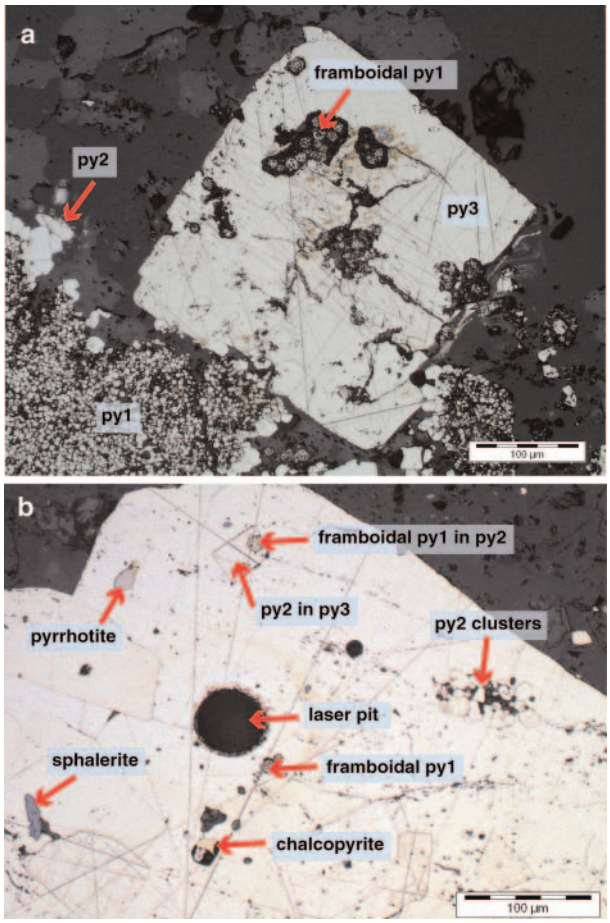

FIG. 13. Examples of pyrite paragenesis. a. Framboidal py_1 is overgrown by later large euhedral py_3. Patches of microcrystals of py_1 are surrounded by small euhedral crystals of py_2, which in places are overgrown by large euhedral py_3. b. A large euhedral crystal of py_3 has overgrown and included framboidal py_1, small euhedral py_2, sphalerite, pyrrhotite, and chalcopyrite inclusions.

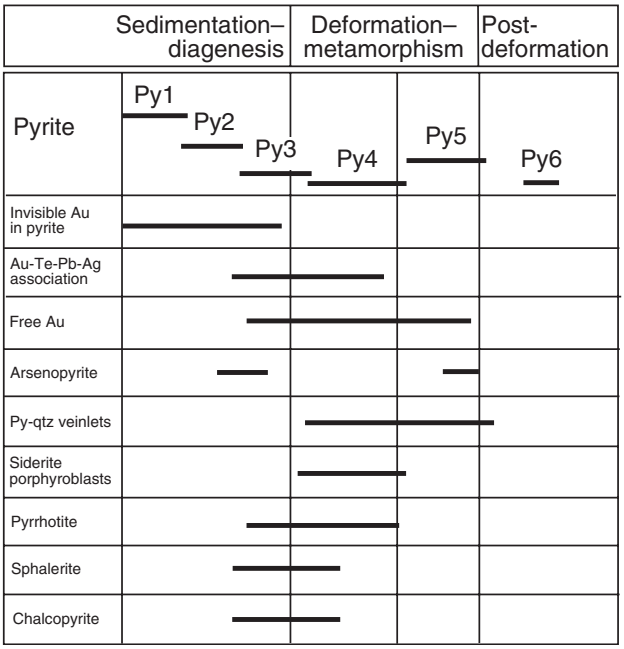

FIG. 14. Paragenetic sequence of Sukhoi Log mineralization interpreted from textures and pyrite geochemistry.

inclusion-free py_5 overgrows both diagenetic py_3 and metamorphic py_4 (Fig. 10c-d, 11b-f). Py_5 is best developed in the folded pyrite-quartz veinlets where it is surrounded by pressure solution quartz fibers (Fig. 5e), indicating that it grew during the folding. Pyrrhotite, sphalerite, and chalcopyrite occur as minor inclusions within both py_3 and py_4 (Figs. 9b-c, 13b). However, these sulfides are rarely present in samples containing only py_1 and py_2. This indicates that sphalerite, chalcopyrite, and some pyrrhotite precipitated during late diagenesis and metamorphism related to the growth of py_3 and py_4.

Sulfides formed postdeformation

Py_6 formed from the alteration of pyrrhotite after deformation (Fig. 10e). There is no clear relationship between py_5 and py_6; however, py_6 is interpreted as a very late stage event possibly related to the late-stage barren milky white quartz veining.

Native gold paragenesis

Native gold is present as inclusions in py_3, py_4, and py_5 (Fig. 12). It is most abundant in the pyrite-quartz veinlets and aggregates but is also present in disseminated bedding-parallel py_3 and in the coarse euhedral py_4 styles of mineralization. In the pyrite-quartz veinlets, native gold occurs in the py_3 and py_4 cores, in py_5 rims, and less commonly intergrown with quartz in the pressure shadows of py_5. No native gold was found associated with py_1 and py_2. The interpretation of the timing of native gold emplacement at Sukhoi Log will be discussed in a subsequent section after presentation of the LA-ICPMS gold data on pyrite.

LA-ICPMS Trace Element Geochemistry of Pyrite

The trace element composition of pyrite types py_1 to py_6, pyrrhotite, and arsenopyrite was determined by LA-ICPMS on a suite of 44 representative samples through the mineralized zone and adjacent sedimentary host rock. Tables 1 and 2 give representative analyses of each pyrite type, as well as means and ranges for all analyses for py_1 to py_6. Some statistical data on the gold content of each pyrite type is presented in Table 4. The data include 66 analyses of py_1, 67 of py_2, 68 of py_3, 52 of py_4, 21 of py_5, 6 of py_6, 24 of pyrrhotite, and 56 of arsenopyrite. Figure 15 shows selected laser spot analyses for gold in typical types of pyrite, and Figure 16 shows the LA-ICPMS analyses of gold in py_1 to py_5 and pyrrhotite. The chemistry of pyrite hosted by the sedimentary rocks is discussed first, followed by the more complex chemical relationships found in the zoned pyrite aggregates in the pyrite-quartz veinlets.

Py_1 composition

Py_1 contains a wide range of trace elements, the most abundant of which are As, Ni, Pb, Co, Ti, Ba, Cu, and Sb. The invisible gold content varies from 0.44 to 12.10 ppm (mean = 3.32 ppm Au, Fig. 16), whereas arsenic varies from 180 to 14,000 ppm (mean = 1,900 ppm As). Due to the fine-grained

TABLE 4. Some Statistics for LA-ICPMS Analyses of Gold in Sediment-Hosted Pyrite from Sukhoi Log

Pyrite type	Number	Mean Au (ppm)	Median Au (ppm)	SD (ppm)	Variance (ppm)	Min. (ppm)	Max. (ppm)
Py_1	67	3.32	2.47	2.97	8.81	0.44	12.14
Py_2	68	1.02	0.42	2.09	4.38	0.02	12.49
Py_{3a}[1]	62	0.12	0.06	0.15	0.02	0.01	0.8
Py_{3b}[1]	7	26.6	20.09	29.1	846.9	2.22	82.22
Py_4	45	0.25	0.16	0.26	0.07	0.02	1.3
Py_5	14	0.07	0.05	0.07	0.005	0.01	0.22

[1] Py_{3a} = without visible gold inclusions; py_{3b} = with gold inclusions

nature of py_1, and intergrowth with the matrix of the sedimentary rocks, it was not possible to obtain a pure py_1 analysis. A laser beam diameter of 10 to 40 μm was commonly used to analyze aggregates of py_1 microcrystals and matrix. The aggregates generally contained more than 80 vol percent of py_1. Analysis of the sedimentary rock matrix (Table 1) indicates that it is relatively enriched compared to py_1 in the following suite of trace elements: V, W, Cr, Tl, Sn, Ba, Ti, U, Th, Zr, Zn, Mn, and La. Except for Ti, Mn, and Ba, these elements are commonly not present in significant amounts in the analyses of py_1. A typical LA-ICPMS output trace for py_1 is shown in Figure 17a. The fairly flat pattern for the counts of all the elements listed (Pb, Co, Ni, As, Sb, Bi, Ag, Te, and Au) and their similar pattern to the Fe counts suggest that these elements are most probably contained within the structure of the pyrite. Spikes in the LA-ICPMS trace for a particular element indicate the presence of microinclusions of a mineral containing that element. An example is given in Figure 17a for the Pb trace, where the arrow indicates a microinclusion of galena within py_1. The range and mean of the most

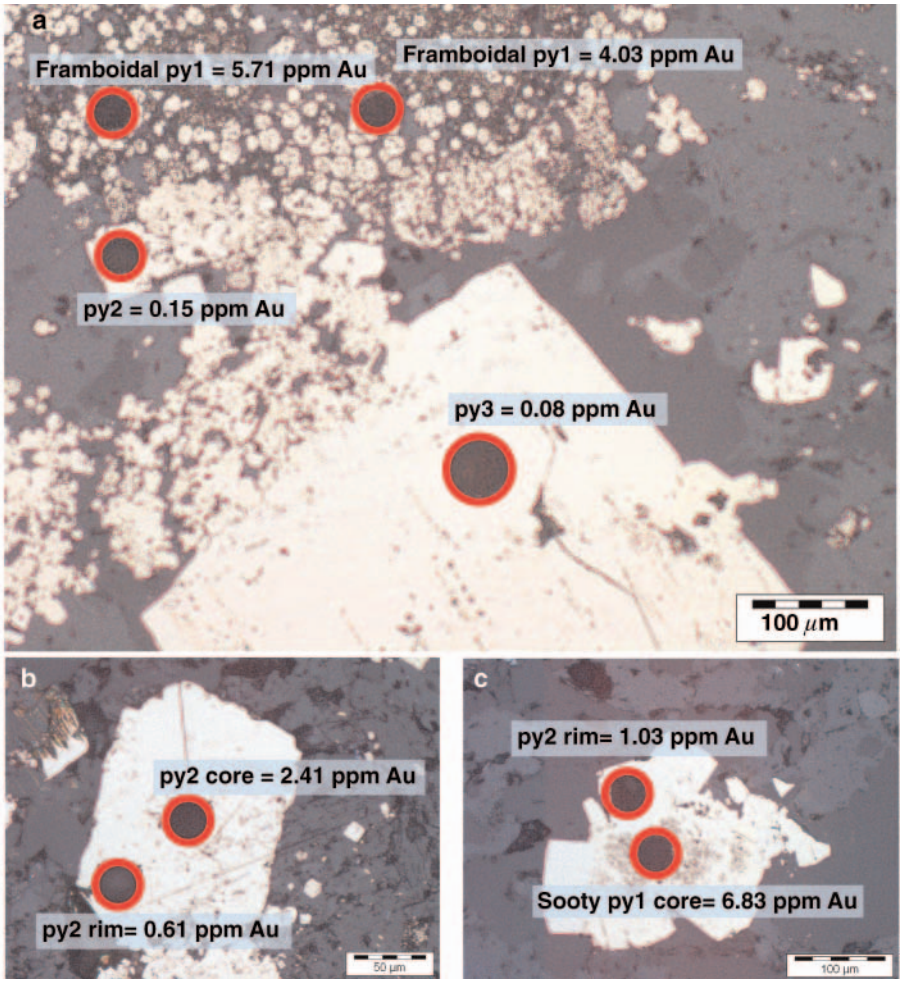

FIG. 15. Some examples of LA-ICPMS spot analyses of gold (in ppm) on different pyrite generations. Note the highest gold values are in py_1 and the recrystallized cores to py_2.

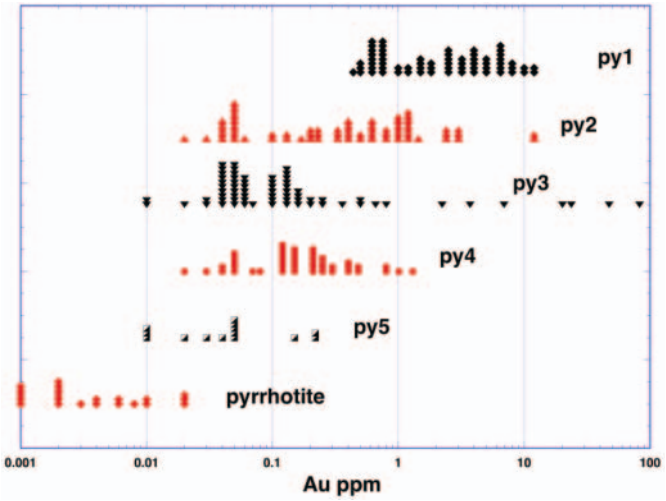

FIG. 16. Histograms of LA-ICPMS gold analyses for all sediment-hosted pyrite types (py_1–py_5) and pyrrhotite (data summarized in Table 4). Note the general decrease in the gold content of pyrite from py_1, with the highest values, to py_5 with the lowest values. Pyrrhotite contains less gold than all pyrite generations.

significant elements analyzed in py_1 are shown in Figure 18a. Broad positive correlations between Au-Pb, Au-Ag, Au-Cu, Au-As, and Au-Ni are evident in the py_1 data (Fig. 19).

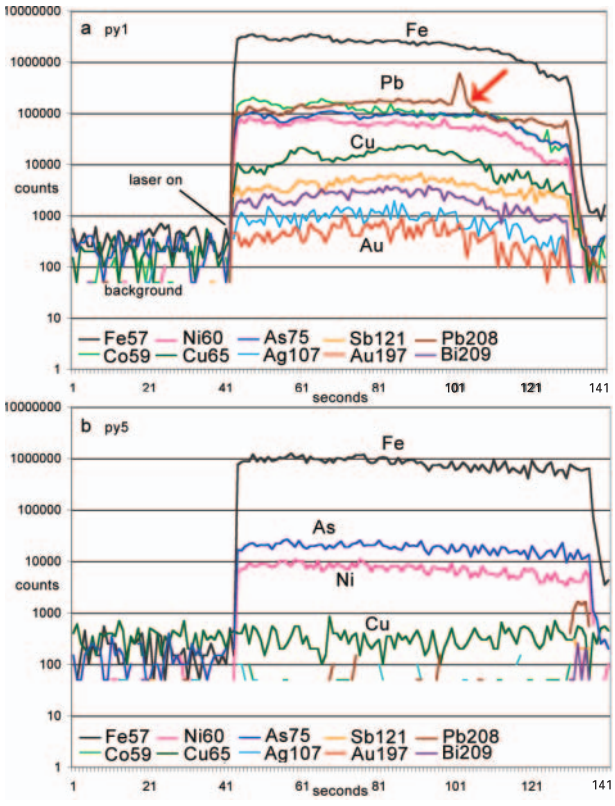

FIG. 17. Typical ICPMS counts output for pyrite analysis by laser ablation. a. Py_1; note the relative high counts of Pb, As, Co, Ni, Cu, Sb, Ag, and Au. The spike in the Pb trace indicates a microinclusion of galena in the pyrite. b. Py_5; note the lack of most trace elements except As, Ni, and Cu.

Py_2 composition

Compared with py_1, py_2 contains less Au, Ag, Mn, Ba, Cu, Pb, Te, Zn, Sb, V, and U (Figs. 18b, 19a-c). The invisible gold content of py_2 varies from 0.02 to 13.00 ppm (Fig. 16, mean = 1.02 ppm Au), and arsenic varies from 2 to 18,550 ppm (mean = 4260 ppm As). The different, but overlapping, gold contents of py_1 and py_2 are shown in Figure 16. It is evident that only 28 percent of the py_2 analyses are greater than 1 ppm Au, compared with 68 percent of the py_1 analyses. The larger size of py_2 euhedra (20–50 μm) enabled pure py_2 analyses to be obtained with laser spot sizes from 15 to 40 μm (Fig. 15a). The marked depletion of Au, Pb, Ag, and Cu in py_2 compared with py_1 is displayed in Figure 19a-c. In contrast, As and Se are not depleted but exhibit a slight enrichment, in py_2 compared with py_1 (Fig. 19d, e). Ni shows a more complex pattern, with two trends evident in Figure 19f.

Py_3 composition

Py_3 in the sedimentary rocks is depleted in most trace elements compared to py_1 and py_2 (Fig. 18c). Gold in py_3 exhibits two compositional populations (Fig. 16). About 80 percent of the py_3 analyzed has a very low invisible gold content from 0.05 to 0.8 ppm (mean = 0.16 ppm Au). However in a small number of analyses, py_3 returned a high gold content from 2.2 to 82 ppm (mean = 30 ppm Au, Table 4). These high gold analyses are most likely due to inclusions of free gold within the pyrite that have been sampled by the laser (Fig. 20). Py_3 in the bedding-parallel pyrite-quartz veinlets is commonly enriched in native gold and gold-telluride inclusions compared with py_3 disseminated in the sedimentary rock and will be discussed further below. Arsenic concentrations in py_3 overlap with the ranges in py_1 and py_2, with a mean of 2,900 ppm. The large range of values for Cu and Zn in py_3 is likely due the abundant microinclusion of sphalerite and chalcopyrite (Fig. 18c). The marked contrast in trace element content between py_1 and py_3 is shown in Figure 21, which represents a laser traverse across a py_3 euhedra containing inclusions of framboidal py_1. As the laser burns through py_3, counts for Ni and As are elevated, but those of other elements are below background. In marked contrast, as the laser penetrates the framboidal py_1 inclusions, counts for Au, Pb, Sb, Cu, and V show a marked increase, whereas As and Ni show a marginal decrease (Fig. 21). Fe counts remain at the same level across both varieties of pyrite.

Py_4 composition

Although the syndeformation py_4 euhedra may contain inclusions of native gold, the pyrite itself is strongly depleted in invisible gold and most other trace elements, except As, Ni, Ti, and Se, relative to the earlier generations of pyrite. Invisible gold content of py_4 varies from 0.02 to 1.30 ppm (Fig. 16, mean = 0.25 ppm Au, Table 4), and arsenic content varies from 400 to 5,560 ppm (mean = 2,270 ppm As). Ninety-five percent of the py_4 analyzed contains less than 1 ppm Au (Fig. 16). Py_4 has a significantly higher Ti content (mean = 1472 ppm Ti) than the other types of pyrite, which have mean values from 50 to 610 ppm (Table 1). The irregular pattern of Ti counts in the LA-ICPMS output suggests that the Ti is present in py_4 as microinclusions of a Ti mineral (e.g., ilmenite).

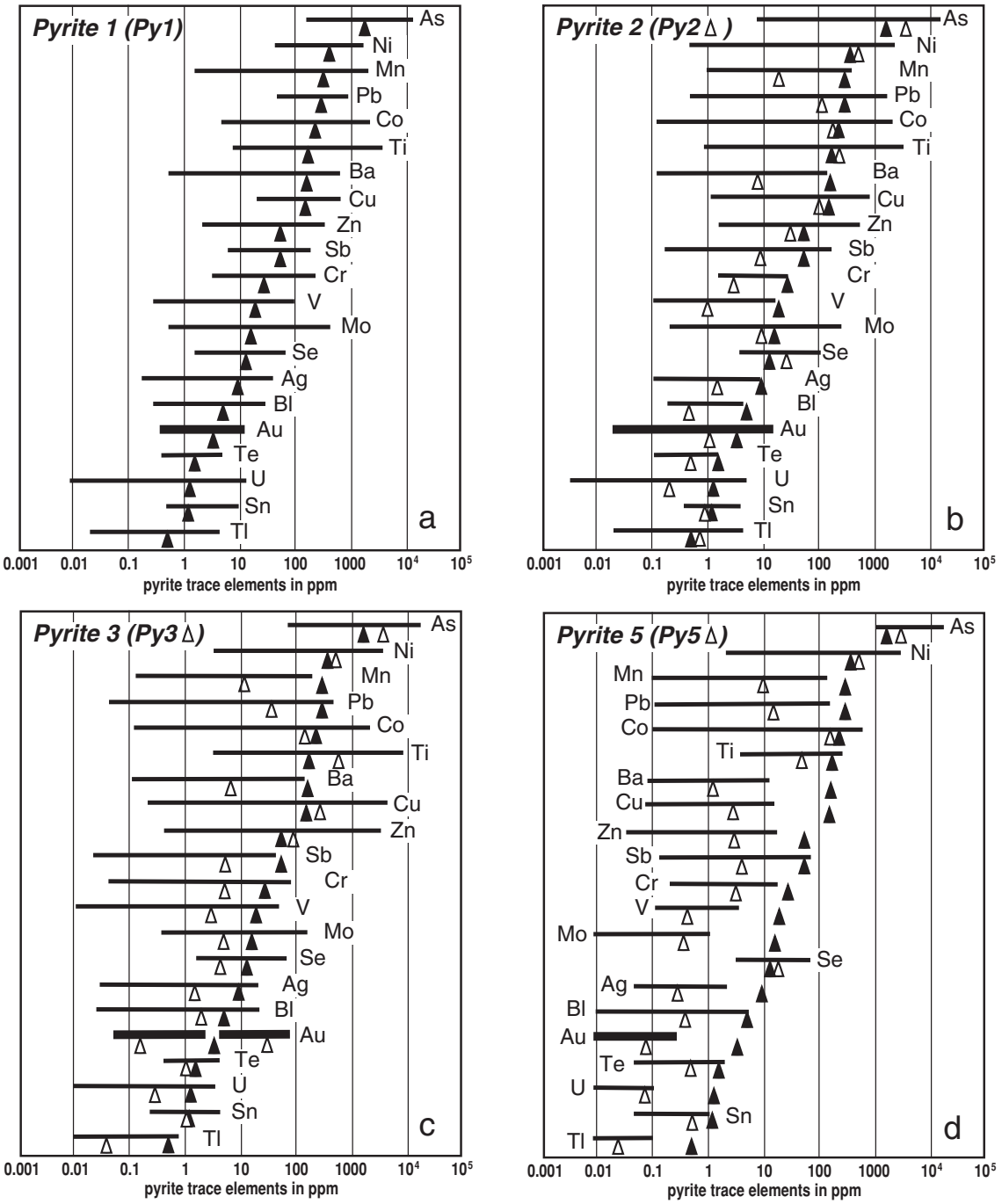

FIG. 18. Range and mean trace element contents for the different pyrite generations hosted in sediments at Sukhoi Log. a. Py_1, the bar shows the range and the black triangle is the mean value for each element. b. Ranges and means for py_2 compared with the means for py_1 in black triangles. c. Ranges and means for py_3 compared with the means for py_1 in black triangles. d. Ranges and means for py_5 compared with the means for py_1 in black triangles.

These Ti-rich inclusions outline the cleavage revealed by etching the py_4 (Fig. 10a-c).

Py_5 and Py_6 compositions

Py_5, which commonly forms clear inclusion-free rims on py_3 and py_4, has the lowest levels of trace elements of all the pyrite types (Figs. 16, 18d). The concentration of invisible gold varies from <0.01 to 0.22 ppm (mean = 0.07 ppm Au, Table 4) and arsenic varies from 980 to 10,500 ppm (mean = 2,900 ppm As).

The late-stage colloform ("birds eye") py_6, which forms by the replacement of pyrrhotite, is generally depleted in all trace elements except Ni (Table 1). The very low As, Se, and Co concentrations in py_6 are significantly lower than in other

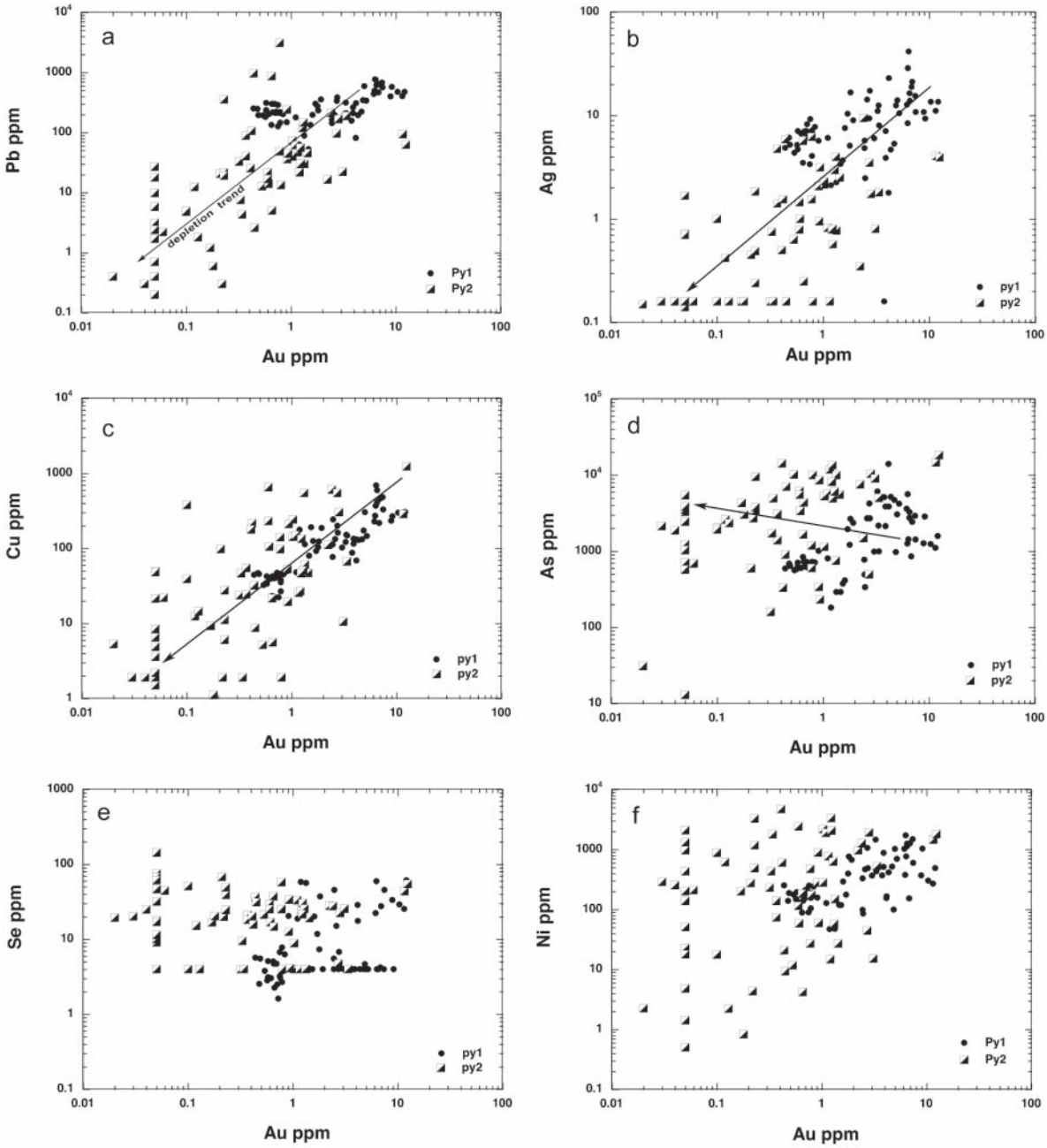

FIG. 19. Interelement correlations in py_1 and py_2. a. Au-Pb. b. Au-Ag. c. Au-Cu. d. Au-As. e. Au-Se. f. Au-Ni. Note the depletion trends from py_1 to py_2 for Au, Pb, Ag, and Cu. In contrast py_2 shows similar or increased levels of As and Se compared to py_1. Some py_2 shows Ni depletion, but most py_2 has an Ni content in the same range as py_1.

types of pyrite but similar to the values in pyrrhotite from Sukhoi Log (Table 1), supporting the interpretation that py_6 forms from the replacement of pyrrhotite.

Pyrite composition in sedimentary pyrite nodules

Detailed LA-ICPMS analyses on py_1 and py_2 in two spherical, 5- to 10-mm, diagenetic pyrite nodules indicate that the nodules contain above background gold and other trace elements. The nodules are composed of approximately 80 vol percent py_2 and 20 vol percent py_1. The py_1, which commonly forms the cores of py_2 aggregates, consists of amorphous spongy forms of anhedral pyrite about 10 to 40 μm across with abundant sediment inclusions (Fig. 15c). In contrast the py_2 consists of inclusion-free anhedral to subhedral pyrite grains with few inclusions. Analysis indicates that the spongy py_1 averages 1.7 ppm gold, with elevated trace elements concentrations similar to other forms of py_1 at Sukhoi Log (Fig. 18a). The recrystallized py_2, which constitutes most of the nodules, averages 0.07 ppm Au, with a low-level trace element signature similar to other py_2 and py_3 analyses.

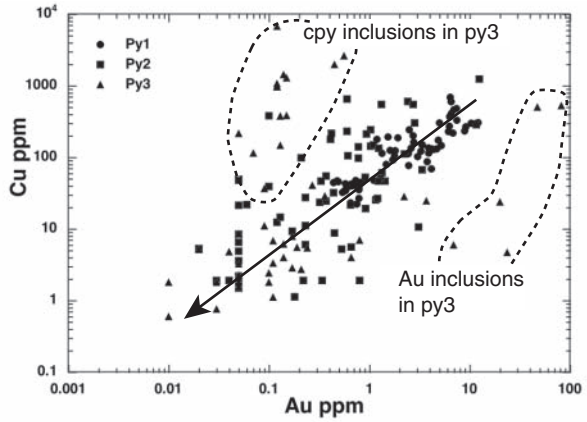

FIG. 20. Correlation between Au and Cu in LA-ICPMS analyses of py_1, py_2, and py_3 hosted in sediments. Note the general depletion trend in both Au and Cu from py_1 to py_3. Py_3 shows some outlier analyses due to microinclusions of native gold and chalcopyrite.

Pyrite composition in bedding-parallel pyrite-quartz veinlets

Pyrite from the gold-bearing, bedding-parallel, pyrite-quartz veinlets has been analyzed by LA-ICPMS to compare with disseminated pyrite within the sedimentary host rocks. One hundred and thirty-eight analyses of pyrite from 14 samples of pyrite-quartz veinlets were recorded. Representative analyses are given in Table 2. Py_3 and py_4, which form the cores of zoned pyrite euhedra (Fig. 11), commonly contain microscopic inclusions of galena, sphalerite, chalcopyrite, arsenopyrite, and pyrrhotite, which contribute to the complexity of the trace element patterns of the pyrite cores. Typically, the cores of veinlet-hosted py_3 and py_4 are enriched in Pb, Bi, Ag, Te, and Au compared to the surrounding py_5 rims (Fig. 22) and also compared to disseminated py_3, py_4, and py_5 hosted within the sedimentary rocks. Detailed SEM and LA-ICPMS analysis of the cores of pyrite euhedra in the veinlets indicates that gold is present in at least three different forms: (1) inclusions of free gold and electrum that vary from 50 to less than 1 μm across (Fig. 12a, c-d); (2) submicroscopic inclusions of galena that are strongly enriched in Ag, Bi, Te, and Au (Fig. 23a); and (3) submicroscopic inclusions of Ag-Au tellurides (Fig. 23b). A combination of SEM and LA-ICPMS indicates that galena inclusions in cores of py_3 contain up to 1.9 wt percent Bi, 1.1 wt percent Ag, 257 ppm Au, and 423 ppm Te. Cores of py_4 in one of the pyrite-quartz veinlet samples (UG1, Table 2, Figs. 11f, 23b) have gold contents of 5.6 to 349 ppm, present as submicroscopic inclusions of petzite (Ag_3AuTe_2). Inclusion-free py_5 that surrounds the py_3 and/or py_4 cores, and makes up about 70 vol percent of the pyrite within the veinlets, contains low levels of invisible Au, Te and most other trace elements (Fig. 22), thus having a similar composition to py_5 within the sedimentary rocks (Fig. 18d).

Pyrrhotite composition

Pyrrhotite, which is commonly present in the most deformed parts of the deposit, and interpreted to result from replacement of pyrite during metamorphism, has a very low content of all trace elements compared with all forms of pyrite (Fig. 16, Table 1). The concentration of invisible gold in pyrrhotite varies from <0.001 to 0.023 ppm with a mean of 0.002 ppm, and the arsenic content is <0.1 to 0.7 ppm. Ni (mean = 590 ppm) is the only trace element found in pyrrhotite at levels consistently above 100 ppm.

Arsenopyrite composition

Arsenopyrite, which is not common at Sukhoi Log, is best developed in siltstone and sandstone facies at the margins of the main gold zone (Fig. 6d), and as corroded crystals in the cores of zoned pyrite in the gold-rich pyrite-quartz veinlets (Fig. 11 a-c). Fifty-six LA-ICPMS analyses of arsenopyrite in nine samples indicate invisible gold contents from <0.1 to 70.5 ppm, with a mean of 3.84 ppm Au (see Tables 1, 2 for selected analyses). Other trace elements in arsenopyrite, with values commonly exceeding 100 ppm, include Co, Ni, Cu, Se, Ti, and Sb (Table 1). Our data suggest two compositional varieties of arsenopyrite: an Ni-Co–rich type (549 ppm to 1.7 wt % Ni; mean 6270 ppm Ni), which has low gold (0.06–1.08 ppm Au; mean 0.31 ppm Au), and an Ni-Co–poor type (13–486 ppm Ni; mean 149 ppm Ni), which has low to high gold (0.02–70.5 ppm Au; mean 6.04 ppm Au). Disseminated arsenopyrite hosted in sediments at the margins of the gold zone is principally the Ni-Co–poor, Au-bearing type (Table 1), whereas arsenopyrite in the cores of pyrite in the gold-rich pyrite-quartz veinlets is exclusively the Ni-Co–rich, gold-poor type (Table 2).

Discussion

Summary of key aspects of the deposit

Underground and detailed drill core observations coupled with the petrographic and LA-ICPMS analyses of pyrite reported in this paper highlight a number of distinct features of the Sukhoi Log deposit. Auriferous bedding-parallel pyrite-quartz veinlets and isolated pyrite-quartz aggregates are the most gold rich components of the orebody, containing several 10s of ppm Au . Our observations indicate that (1) these veinlets and aggregates have been folded, (2) much of the quartz observed within the orebody is secondary in nature and forms strain fringes developed on preexisting pyrite during folding and cleavage development, and (3) some of the gold currently occurs as invisible gold contained in the structure of early, precleavage arsenian pyrite, interpreted as synsedimentary or possibly syndiagenetic; however, most of the gold currently occurs as native gold or telluride inclusions in later pyrite generations.

Prior to folding, the deposit was mainly sulfidic, composed of py_1, py_2, and the bulk of py_3, without much quartz. Invisible Au was present in significant concentration in synsedimentary to syndiagenetic arsenian py_1 and py_2, indicating that gold was introduced into the sedimentary host rocks at an early stage in their geologic history, prior to their folding. Later pyrite overgrowths and associated quartz fibers were added to preexisting auriferous bedding-parallel pyrite layers during folding.

Textural and chemical evolution of pyrite

Previous studies of metamorphosed syngenetic ore deposits, in particular volcanic-hosted Cu-Pb-Zn-Au-Ag massive sulfide deposits (VHMS) and stratiform sediment-hosted

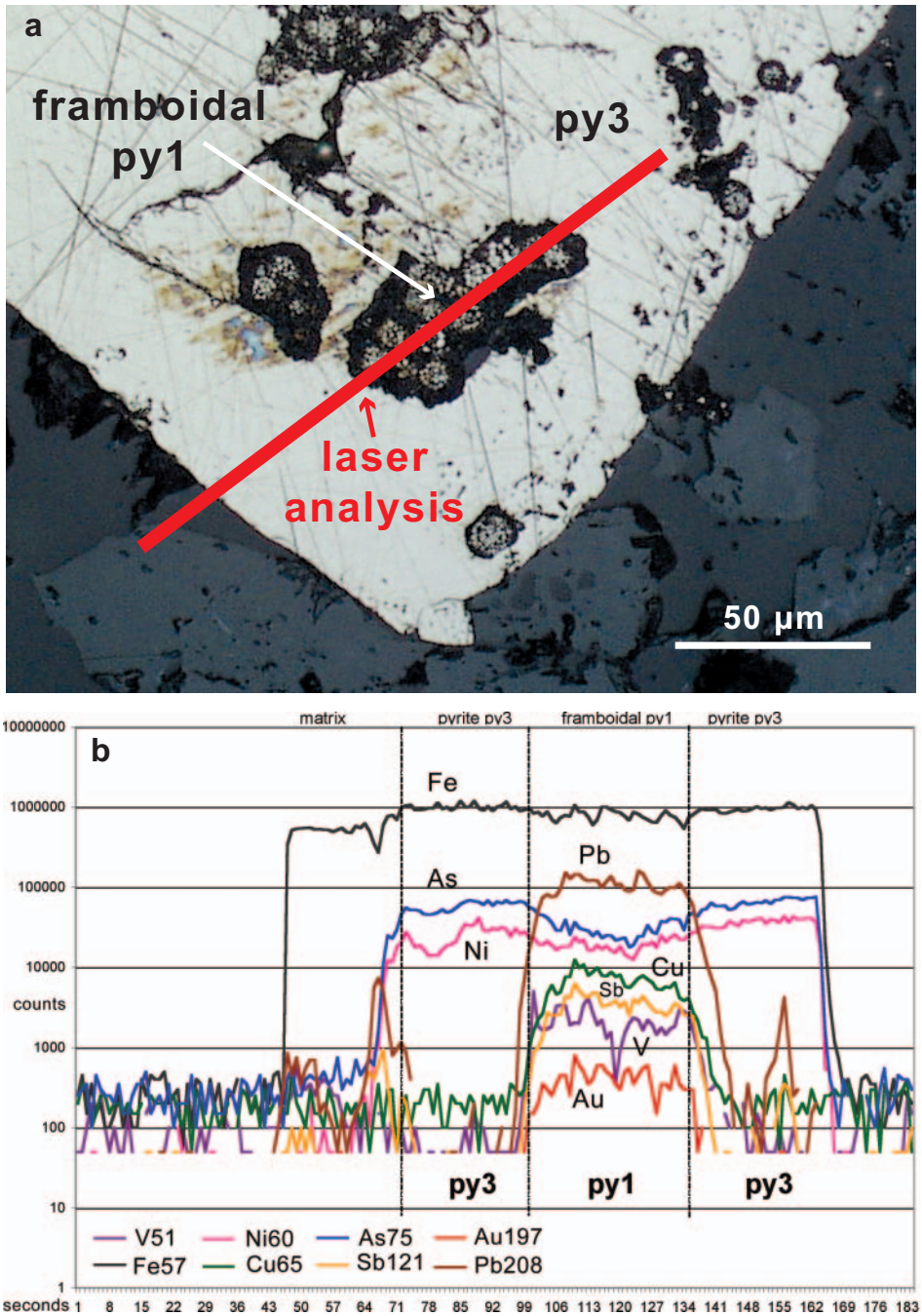

FIG. 21. Laser ablation traverse across a composite of py_1-py_3. a. Path of the laser analysis in red crossing the euhedral py_3, which has overgrown a cluster of framboidal py_1. b. ICPMS counts along the laser traverse shown in (a). Note that the framboidal py_1 is enriched in Au, Pb, Cu, V, and Sb, compared with the surrounding py_3, which is depleted in these elements but contains relatively elevated As and Ni.

Zn-Pb-Ag deposits (SEDEX), have revealed a systematic change in the textures of pyrite and other sulfides accompanying metamorphism (e.g., McClay, 1983a, b; Large, 1992; Marshall et al., 2000). Although the content of pyrite is much lower at Sukhoi Log compared to base metal VHMS and SEDEX deposits, the change in the pyrite textures related to progressive deformation and recrystallization is very similar. Studies by McClay (1983b), Huston et al. (1992), Large (1992), and Marshall et al. (2000) have shown that the earliest pyrite in SEDEX and VHMS systems is fine-grained stratiform, framboidal, and colloform. These types of pyrite are commonly overprinted by coarser grained anhedral to euhedral pyrite of diagenetic or hydrothermal origin. With increasing metamorphism, or hydrothermal overprinting, the pyrite is commonly recrystallized to even coarser grained euhedral forms. There is a general increase in the grain size of

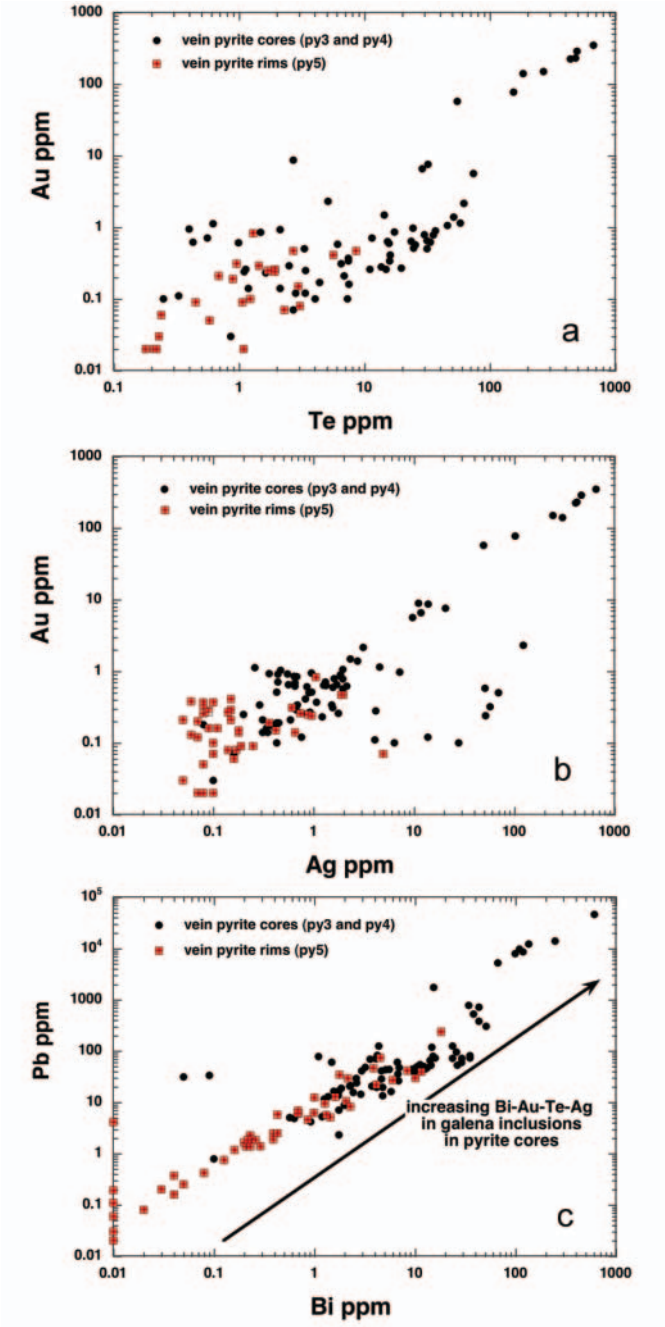

FIG. 22. Some interelement correlations for pyrite in the bedding-parallel pyrite-quartz veinlets. Note the positive correlations between Au-Te, Au-Ag, and Pb-Bi in the py_3 and py_4 cores. In contrast the overgrowth py_5 is relatively depleted in Au, Te, Ag, Pb, and Bi.

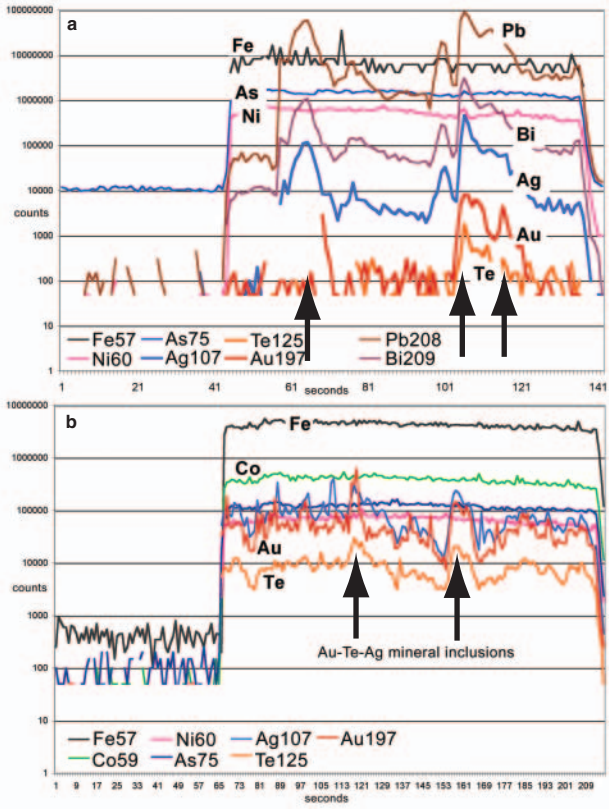

FIG. 23. LA-ICPMS output for analyses of pyrite cores in the bedding-parallel pyrite-quartz veinlets, indicating the presence of Au-Ag-Te–bearing mineral microinclusions within the pyrite cores. a. The pattern of this analysis of a py_3 core indicates microinclusion of galena which contains dissolved Bi, Ag, Au, and Te. b. The pattern of this analysis of a py_4 core indicates microinclusions of a Ag-Au telluride, probably petzite (Ag_3AuTe_2).

pyrite and other base metal sulfides with increasing metamorphism (Marshall et al.; 2000). At Sukhoi Log the change in textural form and grain size from py_1 to py_5 is likewise best interpreted as progressive recrystallization of preexisting synsedimentary and syndiagenetic forms of pyrite during subsequent deformation and metamorphism, involving pyrite dissolution and reprecipitation in a closed system.

One of the key pieces of evidence in support of this interpretation is the relationship between pyrite paragenesis and the invisible gold content of pyrite. The textural evolution of pyrite at Sukhoi Log, from early synsedimentary to syndiagenetic py_1 and py_2, followed by late diagenetic and/or early-folding py_3, and by syn- to late-folding py_4 and py_5, is paralleled by systematic changes in the gold and trace element concentrations of the pyrite. Py_1 contains a suite of elevated trace elements, most of which progressively decrease in concentration through the paragenesis to py_5. In particular, invisible gold is on average most enriched in the structure of py_1 (mean = 3.2 ppm Au), and its concentration decreases progressively through py_2, py_3, py_4 to py_5 (mean = 0.07 ppm Au) and pyrrhotite (mean = 0.002 ppm Au), as shown in Figure 16. Although the amount of gold dissolved in the structure of arsenian pyrite decreases through the paragenesis, the amount of free gold present as inclusions in the pyrite increases. Thus free gold is only apparent as microscopic inclusions in py_3 to py_5. This suggests that diagenesis, deformation-metamorphism, and related pressure-solution processes have led to the redistribution of gold originally contained in the structure of py_1 and py_2, to free gold which now occurs as inclusions and along fractures in the late diagenetic to early deformation py_3, and syndeformation py_4 and py_5.

A similar process has been described by Huston et al. (1992) and Larocque et al. (1993) for liberation of gold from the crystal structure of pyrite during deformation and metamorphism

of a number of volcanic-hosted massive sulfide deposits in Australia and Canada. Huston et al. (1992) found at the Rosebery and Que River VHMS deposits that, as the early syngenetic types of pyrite recrystallize during deformation and metamorphism, gold and silver, held originally within the pyrite, migrate along fractures and grain boundaries via solution-precipitation creep mechanisms, to form discrete grains of microscopic electrum within and adjacent to euhedral pyrite. These processes at Sukhoi Log would have been facilitated by the pressure solution that accompanied the deformation of the deposit, as evidenced by the well-developed slaty cleavage and fibrous quartz in pyrite strain fringes.

The textural and geochemical relationships described above for the pyrite nodules (Fig. 6f) indicate that they were probably initially composed of py_1 and contained an average of about 1 to 2 ppm Au. During diagenesis most of the py_1 was converted to py_2 and py_3, with a consequent loss of gold dissolved in the pyrite, which was reprecipitated as free gold. As noted by Buryak (1982), the replacement of gold-bearing pyrite (py_1) by gold-depleted pyrrhotite in the more intensely sheared parts of the sedimentary sequence at Sukhoi Log was probably another effective way of releasing gold dissolved in pyrite to be subsequently reprecipitated as free gold in the ore zone.

Not only is there a progressive decline in lattice-held gold in pyrite through the paragenesis at Sukhoi Log, but there is also a decrease in the concentrations of a specific suite of other trace elements, in particular, Ag, Cu, Pb, Zn, Mn, Ba, Cr, V, Mo, and Sb (Figs 18–20). Figure 24 shows these trends for Cu, Ag, Pb, and V compared with Au for all pyrite types. However, As, Ni, Co, and Se concentrations in pyrite remain relatively constant or exhibit slightly increasing trends from py_1 to py_5 (Table 1, Fig. 18). A possible explanation for these contrasting trends may relate to how strongly held certain trace elements are within the pyrite structure. Gold, and the loosely held elements (e.g., Ag, Cu, Pb, Zn, Mn, Ba, Cr, V, Mo, and Sb), which are probably present within the pyrite structure, or in some cases as submicroscopic mineral inclusions in the pyrite, may be easily liberated from pyrite accompanying recrystallization and locally redistributed during diagenesis, pressure-solution processes, and metamorphism, as discrete microscopic sulfide phases. In contrast, the strongly held elements (e.g., As, Ni, Co, and Se), which occur as either nonstoichiometric (As) or stoichiometric (Ni, Co, Se) substitutions in the pyrite lattice, may be retained and even enriched during diagenetic and metamorphic pyrite recrystallization and growth.

This process of pyrite cleaning, or purifying, during recrystallization at Sukhoi Log is very similar to that described by Huston et al. (1995) for syngenetic pyrite in many metamorphosed Australian sea-floor massive sulfide deposits. The

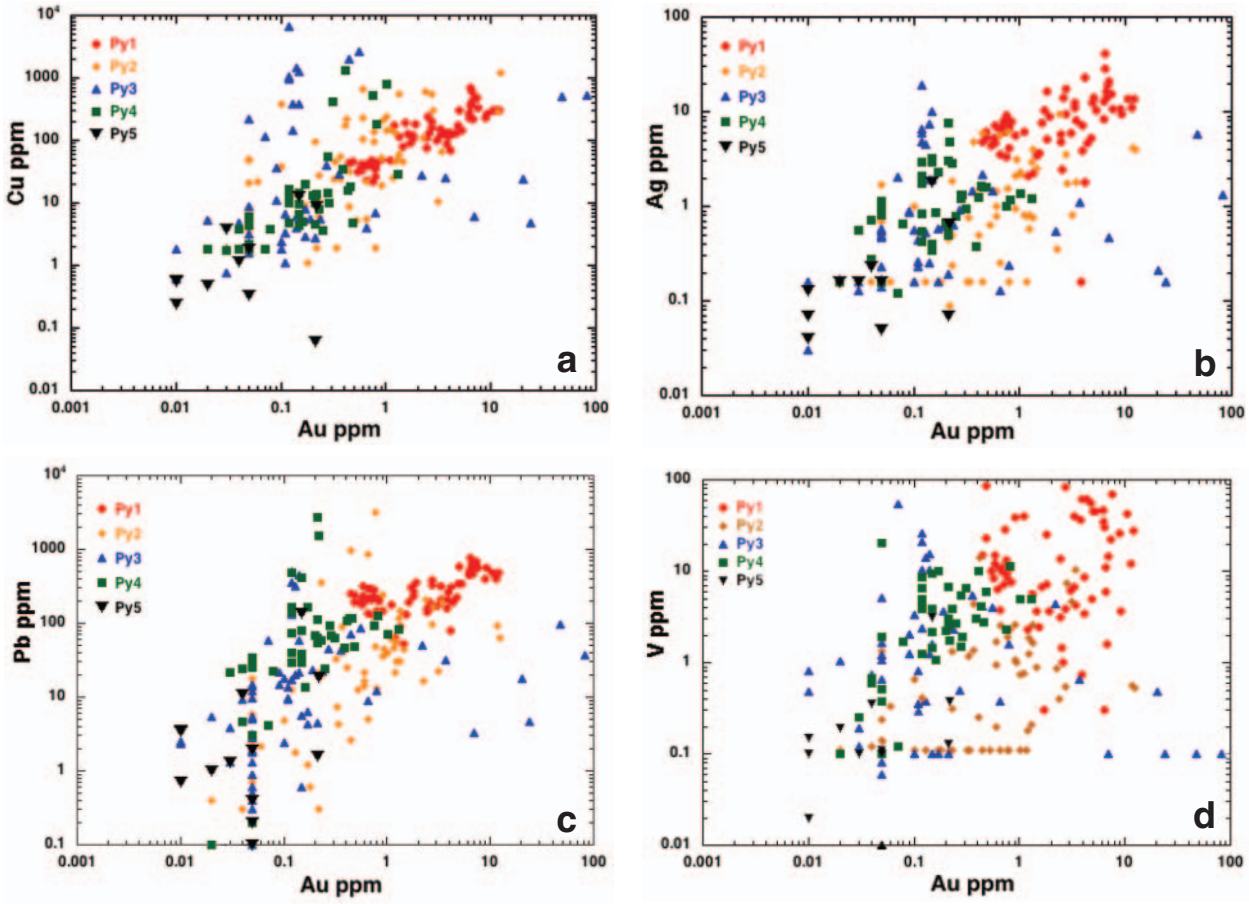

FIG. 24. Correlation between Cu-Au, Ag-Au, Pb-Au, and V-Au for pyrite hosted in the sedimentary host rocks. Note the general trends of decreasing Au, Cu, Ag, Pb, and V from py_1 to py_5. Data plotting off the depletion trends is commonly due to microinclusion of other minerals in the pyrite (e.g., chalcopyrite, native gold, galena, and vanadiferous mica).

common observation of inclusions of sphalerite and chalcopyrite in late diagenetic and metamorphic py_3 and py_4 at Sukhoi Log may be also related to this process. In the same way that gold is released from py_1 and py_2 during recrystallization to form native gold inclusions in py_3 and py_4, Cu and Zn may also be liberated from the structure of py_1 and py_2 to form chalcopyrite and sphalerite inclusions, associated with pyrrhotite and native gold, in py_3 and py_4. A similar process may account for the concentration of Au-Ag telluride and Au-Ag-Bi-Te–rich galena inclusions in the early-formed cores of pyrite in the folded pyrite-quartz veins in the high-grade parts of the deposit. Our data on py_1 and py_2 suggests that these elements (Au, Te, Pb, Bi, Ag) were concentrated in the early-formed synsedimentary to syndiagenetic bedding-parallel layers of arsenian pyrite and arsenopyrite. During late diagenesis and metamorphism, these elements were released from the pyrite structure to form inclusions of free gold, Au-Ag tellurides, and galena enriched in Bi-Ag-Te-Au in the late diagenetic py_3 and overgrowth py_4 in the veinlets. Ongoing folding of the veinlets was accompanied by the growth of gold-poor py_5 and overgrowth fibers of secondary quartz to finally produce the folded pyrite-quartz veinlets that grew within the gold-rich core of the deposit along the axis of the host anticline.

The observation at Sukhoi Log of free gold within syntectonic pyrite would conventionally be interpreted to indicate that the gold was introduced during or after deformation. However, the recognition that early synsedimentary and syndiagenetic forms of arsenian pyrite at Sukhoi Log contain invisible lattice-bound gold, revealed by the LA-ICP-MS analysis, provides clear evidence that some gold was introduced to the host sediments prior to deformation and metamorphism. The question of whether Au and pyrite were also introduced during deformation (as opposed to simply redistributed) remains open and is further discussed below.

Gold-arsenic relationships in pyrite

A correlation between gold and arsenic dissolved in pyrite has been recognized for some time in a range of gold deposit types, including Carlin, epithermal, and orogenic types (e.g., Cook and Chryssoulis, 1990; Savage et al., 2000; Cline, 2001; Reich et al., 2005). The Au-As relationship for pyrite at Sukhoi Log is compared to data for pyrite from Carlin deposits in Figure 25. Also shown in this diagram is the line representing the inferred solubility limit of invisible gold in pyrite determined by Reich et al. (2005). This shows that all Sukhoi Log sediment-hosted pyrite plots well below the solubility maximum, indicating that the gold is most probably held within the structure of the arsenian pyrite, as determined by the LA-ICP-MS analyses (Fig. 17a). By comparison a high proportion of Carlin pyrite plots close to the gold saturation line, with a higher Au/As ratio in pyrite. For the Sukhoi Log data, py_1 plots closest to the gold saturation line (Fig. 25b), with later pyrite generations plotting at progressively greater distance from the line. Py_2 to py_5 contains one to three orders of magnitude less invisible gold than the maximum possible at saturation. The other significant feature of the plot in Figure 25 is that unlike Carlin-type deposits, very few of the pyrite analyses from Sukhoi Log are strongly enriched in both As and Au. There are few Sukhoi Log pyrites in our dataset with greater than both 1 wt percent As and 10 ppm invisible Au, compared with Carlin pyrite where over 30 percent of the data has these characteristics.

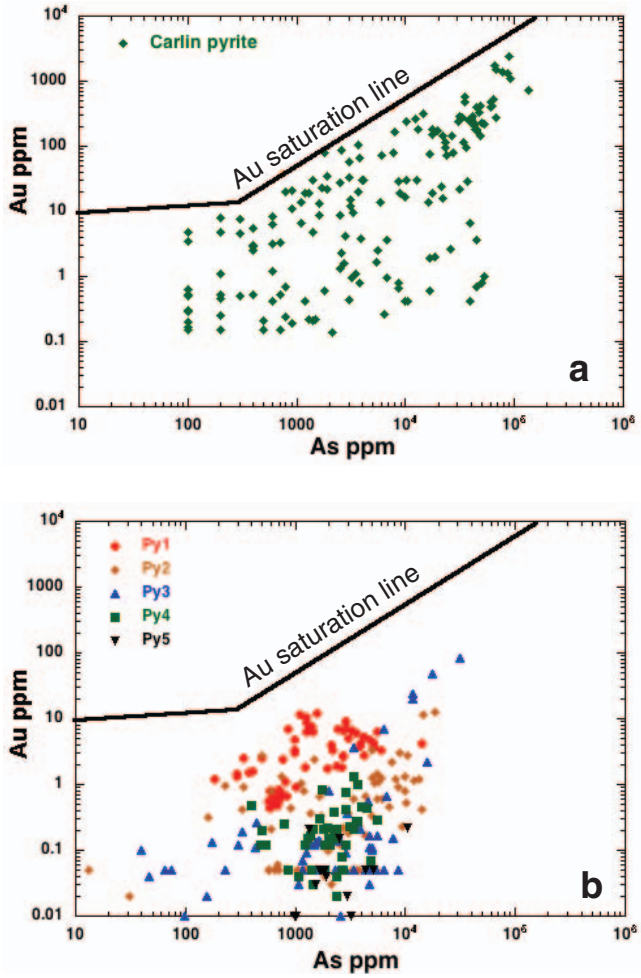

FIG. 25. a. Correlation between Au and As for pyrite from Carlin-type deposits (data from Reich et al., 2005). b. Correlation between Au and As in the five main pyrite types at Sukhoi Log. The gold saturation line is from Reich et al. (2005) and marks the limit of gold dissolved in arsenian pyrite.

Gold-tellurium relationships in pyrite

There is a marked contrast in Au-Te relationships between the sediment-hosted pyrite and bedding-parallel veinlet-hosted pyrite at Sukhoi Log. Pyrite in the bedding-parallel veinlet-hosted pyrite shows a strong positive Au-Te correlation (Fig. 22a), whereas the sediment-hosted pyrite exhibits no obvious correlation. In the sedimentary rocks, the gold is either dissolved in arsenian py_1 and py_2 or occurs as free gold inclusions in py_3, py_4, and py_5. In the pyrite-quartz veinlets, gold is present as inclusions of electrum, gold tellurides, or Au-Ag-Bi-Au-Te–rich galena inclusions within py_3 and py_4 cores within zoned py_5 aggregates. These distinct geochemical relationships between py_1 and/or py_2 and py_3, suggest that py_3 and associated gold formed from a different mineralizing fluid compared to invisible gold-bearing py_1 and py_2.

The organic association of elements

The carbonaceous host rocks at Sukhoi Log average about 0.5 wt percent organic carbon, with a range from 0.15 to 1.1 wt percent (Distler et al, 2004). Razvozzhaeva et al. (2002) found anomalous levels of gold within organic matter from the sediments of the Khomolkho Formation, with soluble carbon compounds (pyrobitumens) containing up to 10 ppm Au. Many of the trace elements concentrated in the early synsedimentary py_1, particularly Cu, Zn, V, Mo, Ni, Co, As, Pb, Cr, Se, Te, U, and Tl are the same elements that are typically concentrated by organic processes in organic-rich black shales (Coveney and Martin, 1983; Patterson et al., 1986; Wood, 1996; Coveney, 2000; Alegro and Maynard, 2004; Rimmer, 2004). These metals are commonly absorbed onto organic matter during sedimentation in strongly anoxic environments and subsequently partitioned into pyrite that grows during diagenesis of the organic-rich sediments. The correlation between Au and these organophile elements in py_1 (Figs. 19, 24) opens the intriguing possibility that gold was present in anomalous amounts in the seawater and was initially concentrated in the anoxic sediments by organic processes and subsequently partitioned into arsenian pyrite during diagenesis.

Is all the gold early?

Gold is observed in two main modes of occurrences and stages of the paragenesis at Sukhoi Log (Fig. 14); early invisible gold held in the lattice of sedimentary and diagenetic py_1, py_2, and minor arsenopyrite, and later free gold and gold tellurides present as inclusions in late diagenetic to syndeformation and vein-hosted py_3, py_4 and py_5. The timing of the free gold present in py_3, in bedding-parallel pyrite-quartz veinlets, is problematic but important, as py_3 hosts the majority of the Au in the deposit. Given the diagenetic to early-folding timing of py_3 described previously, the same timing must also apply to the gold contained in py_3, irrespective of its internal or external origin. Whether or not gold in py_3 comes from completely recrystallized layers rich in early invisible gold-bearing py_1 and py_2 or from involvement of a fluid of different composition remains unresolved. However, the distinct Au-Te correlation recorded in veinlet py_3, compared to py_1 and py_2, suggests the latter is most plausible. The timing of free gold inclusions in py_4 and py_5 is also uncertain, and two possibilities exist: recrystallization of preexisting gold-bearing arsenian py_1, py_2, and py_3, with local-scale redistribution of free gold in a closed system, or addition of sulfides and gold during deformation and metamorphism (open system).

The abundance of quartz pressure shadows on pyrite and associated pressure-solution seams at Sukhoi Log indicate that there have been significant mass transfers at the very local scale during the deformation of the deposit (Durney, 1972; Ramsay, 1980, Cox and Etheridge, 1989). In this context, the closed system scenario is definitely plausible. Because of the significant syndeformation modifications that have taken place within the pyrite-quartz veinlets, py_1 and py_2 are not preserved, and it is not possible to use the presence of early auriferous pyrite to support a synsedimentary introduction of all the gold. However, the fact that significant amounts of free gold and gold tellurides are found in the cores of late diagenetic to early-folding py_3 in the folded bedding-parallel pyrite-quartz veinlet, strongly suggests that much of the gold at Sukhoi Log was introduced to the deposit prior to the main deformation and folding event. The subsequent deformation and metamorphism caused remobilization and further concentration of gold in the high-grade anticlinal core of the deposit. This may have involved recrystallization and dissolution of gold-bearing py_1, py_2, and py_3 from fold limbs to be concentrated in fold hinges as synmetamorphic generations of py_4 and py_5 containing free gold and gold tellurides.

There are a number of other documented examples of closed-system crystallization and remobilization of sulfides during deformation. A notable example is at the Howard's Pass SEDEX deposit (Jonasson and Goodfellow, 1986), where extensive diagenetic to syntectonic pressure-solution processes have resulted in high concentrations of specific sulfide minerals in pressure-solution bands, as well as the remobilization of others, at the hand sample and mine scale, into fold hinges. Excellent examples of galena-sphalerite concentration in mine-scale fold hinges are also recorded in massive sulfide deposits at Broken Hill (Webster, 2006) and Que River (Large et al., 1988). A recent study by Wagner et al. (2007) employed LA-ICPMS analyses of sulfides at the Boliden VHMS deposit to demonstrate gold upgrading during closed-system metamorphism by a similar process as that suggested above for Sukhoi Log. They showed that early fine-grained, gold-enriched, arsenopyrite in the massive sulfide ores was recrystallized during metamorphism with release of gold to become concentrated as free gold in crosscutting veins and fracture zones.

The textural and geochemical data presented here does not entirely preclude the possibility that some additional gold was added to the Sukhoi Log deposit from other sources during later events—say by a metamorphic fluid or a magmatic fluid. Distler et al. (2004) proposed that the intrusion of syntectonic granites over the period 460 to 320 Ma was the main source of the gold mineralization. However, the closest granite is a small body which crops out 6 km southwest of Sukhoi Log and is unlikely to have been responsible for additions of significant gold to the distant deposit. Distler et al. (2004) also refers to Pb isotope data on galena at Sukhoi Log, which they interpret to indicate a Pb-Pb model age for the gold mineralization of 400 to 380 Ma (Stacey-Kramers model). However, Pb isotope data on Sukhoi Log presented in Larin et al. (1997, fig. 148), measured on gold, pyrite, and auriferous pyrite, gives a spread of values indicating a model age from 600 to 350 Ma based on the Zartman and Doe (1981) orogen model.

The geologic, textural, and pyrite compositional data presented here provide evidence for early introduction of the gold during or very shortly after sedimentation, during diagenesis, and possibly in the earliest stages of deformation and/or folding. This suggests a prolonged history of gold introduction during sedimentation, diagenesis and possibly early folding, followed by a period of gold remobilization during the main deformation. Geochronological studies, accompanied by sulfur and lead isotope analyses of the various types of pyrite, are being carried out to verify the above interpretations.

What was the scale of the closed-system gold remobilization event?

The percentage of gold-bearing syngenetic py_1 in the host sediments within and surrounding the deposit varies from

about 1 to 30 wt percent with an average of less than 5 wt percent. This pyrite has a mean invisible gold content of about 3 ppm. Even if much of the py_1 is now replaced by later generations of pyrite (py_2–py_5) or by pyrrhotite, there are insufficient sulfides in the immediate vicinity of Sukhoi Log to account for all the free gold in the deposit, if it was originally sourced from py_1. However the bulk of the free gold in the Sukhoi Log resource occurs in the cores of py_3 in the pyrite-quartz veinlets, which formed during late diagenesis and early folding. The distinct geochemistry of the py_3 cores suggests that this gold was introduced by an external Au-Te-Pb-Ag–rich fluid during late diagenesis and early folding and was unlikely to have been sourced from the recrystallization of earlier py_1 and py_2. Free gold within the later post-cleavage py_4 and py_5 is the only gold that definitely formed during the deformation and may not have been present in the deposit prior to deformation. This gold may account for up to 20 percent of the resource; however, detailed analyses are not available to verify this estimate. The origin of this late-stage gold may be from recrystallization of earlier gold-bearing py_1, py_2, and py_3 within the deposit or by leaching of gold from sediments below or adjacent to the deposit.

Buryak (1982) maintains that unmineralized black shales in the Lena gold province may have contained elevated levels of gold, over hundreds of square kilometers. Kuz'min et al (2006) reports work of Razvozzhaeva et al. (2002) who state that the gold content of the regional carbonaceous shales of the Khomolkho Formation (host to Sukhoi Log deposit) and the Aunakit Formation (host to Pervenets-Venensky deposits) is commonly three to five times higher than the mean for black shales generally, even well beyond the limits of the ore deposits. They report values of 1 to 2 ppm Au in insoluble carbonaceous matter extracted from the regional Khomolkho Formation. Based on our average LA-ICPMS gold content of py_1 of 3 ppm, and assuming the black shales of the Khomolkho Formation prior to diagenesis and metamorphism averaged a conservative 1 wt percent py_1, then the average gold content of the regional black shales may have originally been at least 30 ppb Au. If about 80 percent of the gold was leached and remobilized from the shales during late diagenesis and metamorphism, then 24 ppb Au would have been leached and 6 ppb Au would remain behind in the shales following deformation and metamorphism. This value compares favorably with data from Buryak and Khmelevskaya (1997) who reported mean values of 3 to 8 ppb Au in carbonaceous shales in the district. Considering that Sukhoi Log has a total resource of about 30 Moz of gold, and that about 20 percent of this is contained in the later stage syndeformation pyrite, mass-balance calculations suggest that approximately 3 km^3 of gold-bearing carbonaceous sediments would need to be leached during diagenesis and metamorphism to account for all the gold contained in the syndeformation pyrite (py_4 and py_5).

Further work is required to test this hypothesis of gold leaching from the Khomolkho Formation and concentration in the Sukhoi Log anticline during deformation. The alternative possibility that the late-stage free gold in py_4 and py_5 formed by recrystallization and redistribution of earlier syndiagenetic gold from the py_3 cores remains an equally viable alternative.

Preferred genetic model for Sukhoi Log

Based on the data and discussion presented above, our preferred genetic model for Sukhoi Log is outlined in Figure 26 and described next.

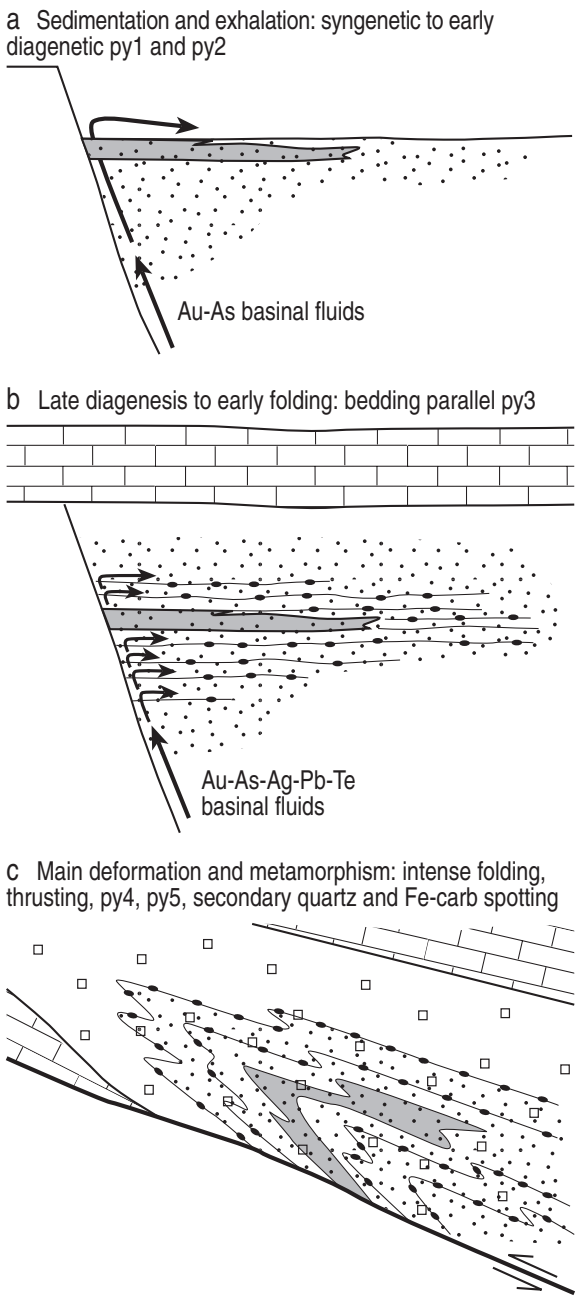

FIG. 26. Diagrammatic model for the evolution of pyrite and gold at Sukhoi Log. a. Deposition of gold-bearing syngenetic and diagenetic arsenian pyrite related to regional exhalation of hydrothermal Au-As fluids into the euxinic black shales of the Khomolkho Formation. b. Growth of bedding-parallel late diagenetic to early folding gold-bearing arsenopyrite and py_3 due to lateral flow of hydrothermal fluids through porous siltstone beds of the Khomolkho Formation. c. Intense deformation and metamorphism causes folding and growth of bedding-parallel pyrite-quartz veinlets. Gold, originally dissolved in earlier stages of arsenian pyrite (py_1, py_2) in the carbonaceous sediments regionally, is remobilized and concentrated as free gold and gold tellurides in syndeformation pyrites (py_4, py_5), which develop preferentially in the fold hinge of the Sukhoi Log anticline.

1. During sedimentation of organic-rich shales and siltstones of the Khomolkho Formation (Fig. 26a), reduced deep basinal H_2S-rich fluids carrying gold and arsenic were exhaled along east-west–trending synsedimentary rift faults. Gold and arsenic, along with other trace elements (Sb, Ni, Co, Se, Te, Ag, Cu, Pb, Zn, Mo, Mn), were trapped in the sea-floor organic-rich muds and partitioned into the associated syngenetic and early diagenetic arsenian pyrite (py_1 and py_2). This was a regional event that led to concentration of gold throughout the Khomolkho Formation but with higher grades close to sites of exhalation.

2. During late diagenesis and possibly early folding (Fig. 26b), and following deposition of the carbonates of the overlying Imnyakh Formation, Au-As-Te-Pb–bearing basinal fluid continued to be pumped laterally through the organic-rich sediments adjacent to the proposed feeder faults, below the impermeable cap of overlying carbonates. The fluids flowed through the more permeable narrow siltstone layers in the turbiditic sediments, with growth of late diagenetic arsenopyrite and py_3 aggregates in bands parallel to bedding. Gold became enriched along with Pb, Ag, Bi, and Te in the cores of the growing diagenetic arsenian pyrite.

3. During deformation and metamorphism (Fig. 26c), the sedimentary rocks at Sukhoi Log were folded into a tight overturned anticline, and it is possible that the original synsedimentary feeder fault was reactivated as a thrust fault, as originally suggested by Buryak and Khmelevskaya (1997). Flow of metamorphic fluids through the Khomolkho Formation may have led to dissolution of early gold-bearing py_1 from the regional fold limbs and further gold concentration in syndeformational pyrite in fold axes overprinting the earlier stages of pyrite and gold deposition. In the core of the deposit, py_4 overgrew the earlier py_1, py_2, and py_3. The layers of gold-rich py_3 were folded, accompanied by pressure-solution and redeposition processes that led to their overgrowth by metamorphic py_4 and py_5 and by secondary quartz fibers developed in pressure shadows, resulting in the folded pyrite-quartz veinlets. During deformation, lattice-bound gold in py_1, py_2, arsenopyrite, and py_3 was released to form inclusions of free gold, gold tellurides, and galena, with dissolved Ag-Bi-Te, in the later pyrite generations.

Are the processes that formed Sukhoi Log unique?

The proposal for an early stage of syngenetic gold deposition in major sediment- and/or volcanic-hosted orogenic gold provinces is not new. Hutchinson (1975, 1993) proposed a multistage hypothesis for greenstone-hosted gold deposits, commencing with exhalative deposition over broad areas of the sea floor, leading to gold concentration in interflow sediments, followed by gold remobilization and concentration in lodes and stockworks related to metamorphism and deformation. Emsbo (2000) recognized an early Devonian syngenetic concentration of gold in organic-rich mudstones of the Popovich Formation in the Carlin district, Nevada, which were later overprinted in the Tertiary to produce high-grade strata-bound and structurally controlled Au-As deposits of the Carlin main stage. Recently Wood and Large (2007) have provided geochemical evidence to support an early syngenetic gold event in the Ordovician turbidites of the western Victorian goldfield, followed by emplacement of gold in quartz reef structures during metamorphism and deformation in the Devonian.

It appears, from our research at Sukhoi Log, that there were a number of processes that contributed to the formation of the deposit, however two process were crucial: synsedimentary to early diagenetic concentration of invisible gold within pyrite in organic-rich shales, and release of invisible gold during late diagenesis and metamorphism and reconcentration as free gold and gold tellurides in later generations of pyrite. The latter process was probably instrumental in converting what was originally an uneconomic low-grade refractory gold deposit into an upgraded, likely economic, deposit containing free gold and gold tellurides. Similar processes have affected the economics of gold-rich sea-floor VHMS deposits (Laroque et al., 1993; Huston et al., 1995; Wagner et al., 2007). Buryak (1982) and Kribek (1991) suggested that the conjunction of these key processes is not unique to Sukhoi Log but may have contributed to the formation of a number of sediment-hosted "orogenic-style" gold deposits, including Muruntau in Kazakhstan and Macraes in New Zealand. Kribek (1991) refers to these deposits as metamorphogenic gold deposits. They typically form in anoxic to euxinic sediments of active continental margins, where initial rifting and hydrothermal exhalation concentrates gold in arsenian pyrite in black shales of the continental slope facies, followed by basin closure and collision producing a protracted period of metamorphism capable of releasing and redistributing the gold into structural traps.

Remaining questions and issues regarding the origin of Sukhoi Log

There are a number of issues that need to be resolved in order to develop a more robust model for the origin of all the gold at Sukhoi Log. Some of the more important questions are (1) how extensive is the semimassive stratiform SEDEX-type pyrite zone intersected in drill hole C1 (delineation of this zone will help to define the main exhalative center at Sukhoi Log); (2) can the synsedimentary feeder faults be recognized and how do they relate to the mapped thrust faults; (3) what are the regional background values of gold in the Kholmolkho Formation (this will help to resolve the potential source of gold during deformation); and (4) can Pb and S isotopes help in defining potential sources of fluids that deposited pyrite and gold and inform interpretations of sulfide and gold paragenesis?

Conclusions

The results from this research on pyrite paragenesis, vein formation, and trace element geochemistry at Sukhoi Log support the previous model by Buryak (1982) and Buryak and Khemelevskaya (1997) that gold was initially concentrated in the organic-rich shales and siltstones during sedimentation and diagenesis and later remobilized during metamorphism. We have clearly shown, based on the textures and LA-ICPMS analyses of pyrite, that gold was initially trapped in the structure of fine-grained sedimentary and early diagenetic forms of arsenian pyrite (py_1 and py_2). The gold-rich pyrite-quartz veinlets in the core of the deposit had a more protracted history of formation, which commenced with the growth of bedding-parallel, gold-bearing, diagenetic pyrite (py_3), followed

by syndeformation overgrowth pyrite (py_4). Ongoing folding was accompanied by the growth of gold-poor py_5 over the py_3 and/or py_4 cores, with contemporaneous development of secondary quartz fibers to form the folded bedding-parallel pyrite-quartz veinlets. During late diagenesis and metamorphism, pressure-solution processes also led to the release of Au, Te, Zn, Cu, and Pb previously locked in the fine-grained sedimentary and early diagenetic arsenian pyrite (py_1, py_2) to form inclusions of free gold, gold tellurides, galena, sphalerite, and chalcopyrite within the later coarse-grained generations of py_3, py_4, and py_5. Although we conclude that most of the gold was introduced early at Sukhoi Log, later deformation may have played a key role increasing the gold grade toward economic levels and improving the ratio of free gold to refractory gold in the deposit.

This multistage process of syndiagenetic pyrite and gold deposition, with later deformation-related pyrite recrystallization, gold liberation, and reconcentration, are key to the formation of Sukhoi Log but may also apply to the genesis of other black shale-hosted disseminated and veinlet gold deposits formed in active continental margin settings, which have undergone rifting followed by collision.

Acknowledgments

This research was supported by funding from the Australian Research Council by way of an ARC Centre of Excellence grant to RRL. FR acknowledges Barrick Gold Corporation for permission to share his underground observations at Sukhoi Log. Rob Scott is thanked for his critical comments and discussion which have significantly improved the manuscript. Thanks to the Lena Gold Mining Company, in particular Chief Geologist Vladimir Martynyuk and Deputy Valery Benedyk, for providing valuable assistance and access to the drill core from Sukhoi Log, and to Ekaterina Evlapova, Chief Geologist of the Sukhoi Log Mining Company, for access to the Zapadnoe open-cut mine. Thanks also to Eugene Sklyarov, Director of the Institute of Earth and Tectonics in Irkutsk, and to the late Adrianne Sintsov, Vladimir Simonov, and Oktyabrin Sadyrov for providing assistance in sampling the deposit. The LA-ICPMS analyses at UTAS would not have been possible without the excellent guidance and help of Sarah Gilbert. Bryce Wood first alerted RRL to the potential syngenetic origin of gold at Sukhoi Log, for which the senior author is most grateful. Special thanks to Alexander Yakubchuk who provided an English translation of V.A. Buryak's book on the Sukhoi Log deposit, which has provided invaluable background for the authors. Two *Economic Geology* reviewers, Craig Hart and Ross Sherlock, as well as Howard Poulsen, provided valuable comments that have substantially improved the manuscript.

March 9, November 20, 2007

REFERENCES

Alegro, T.J., and Maynard, J.B., 2004, Trace-element behaviour and redox facies in core shales of Upper Pennsylvanian Kansas-type cyclothems: Chemical Geology, v. 206, p. 289–318.

Benevolskiy, B.I., 2002, Gold of Russia: Moscow, OOO Geoinformmark, 462 p. (in Russian).

Buryak, V.A., 1964, The process of regional metamorphism influencing development of gold-sulfide mineralization in the central part of the Lena goldfield: Physical-Chemical Conditions of Magmatism and Metasomatism, All-Union Petrographic Symposium, 3rd, Moscow, Collected Papers, p. 184–189

——1967, Genesis of sulphide mineralization of Lena gold-bearing region: Geologiya i Geofizika, v. 1, p. 113–118.

——1982, Metamorphism and ore formation: Moscow, Nedra Press, 256 p. (in Russian).

Buryak, V.A., and Khmelevskaya, N.M., 1997, Sukhoy Log, one of the greatest gold deposits in the world: Genesis, distribution patterns, prospecting criteria Vladivostok: Dalnauka, 156 p. (in Russian).

Cline, J.S., 2001, Timing of gold and arsenic sulfide mineral deposition at the Getchell Carlin-type gold deposit, north-central Nevada: Economic Geology, v. 96, p. 75–89.

Cook, N.J., and Chryssouilis, S.L., 1990, Concentrations of invisible gold in the common sulfides: Canadian Mineralogist, v. 28, p. 1–16.

Coveney, R.M., 2000, Metalliferous shales and the role of organic matter, with examples from China, Poland, and the United States: Reviews in Economic Geology, v. 9, p. 251–280.

Coveney, R.M., and Martin, S.P., 1983, Molybdenum and other heavy metals of the Mecca Quarry and Logan Quarry shales: Economic Geology, v. 78, p. 132–149.

Cox, S.F., and Etheridge, M.A., 1989, Coupled grain-scale dilatancy and mass transfer during deformation at high fluid pressures: examples from Mount Lyell, Tasmania: Journal of Structural Geology, v. 11, p. 147–162.

Croxford, N.J.W., and Jephcott, S.J., 1972, The McArthur lead-zinc-silver deposit, N.T.: Australasian Institute of Mining and Metallurgy Proceedings 243, p. 1–26.

Danyushevsky, L.V., Robinson, P., McGoldrick, P., Large, R.R., and Gilbert, S., 2003, LA-ICPMS of sulphides: Evaluation of an XRF glass disc standard for analysis of different sulphide matrixes [abs.]: 2003 Goldschmidt Conference, Japan: Geochimica et Cosmochimica Acta, v. 67, p. 23.

Distanov, E.G., Kovalev, K.R., and Tarasoav, R.S., 1982, Kholodninskoe pyrite-polymetallic deposit in Precambrian rocks of Transbaikal, Russia: Novosibirsk, Nauka, 208 p.

Distler, V.V., Yudovskaya, M.A., Mitrofanov, G.L., Prokof'ev, V.Y., and Lishnevskiy, E.N., 2004, Geology, composition and genesis of the Sukhoi Log noble metals deposit, Russia: Ore Geology Reviews, v. 24, p. 7–44.

Durney, D.W., 1972, Solution-transfer, an important geological deformation mechanism: Nature, v. 235, p. 315–317.

Emsbo, P., 2000, Gold in SEDEX deposits: Reviews in Economic Geology, v. 13, p. 427–438.

Goldfarb, R., Groves, D.I., and Gardoll, S., 2001, Orogenic gold and geologic time: A global synthesis: Ore Geology Reviews, v. 18, p. 1–75.

Huston, D.L., Bottrill, R.S., Creelman, R.A., Khin, Z., Ramsden, T.R., Rand, S.W., Gemmell, J.B., Jablonski, W., Sie, S.H., and Large, R.R., 1992, Geologic and geochemical controls on the mineralogy and grain size of gold-bearing phases, eastern Australian volcanic-hosted massive sulfide deposits: Economic Geology, v. 87, p. 542–586.

Huston, D.L., Sie, S.H., Suter, G.F., Cooke, D.C., and Both, R.A., 1995, Trace elements in sulfide minerals from eastern Australian volcanic-hosted massive sulfide deposits: Pt. 1. Proton microprobe analyses of pyrite, chalcopyrite and sphalerite: Economic Geology, v. 90, p. 1167–1196.

Hutchinson, R.W., 1975, Lode gold deposits: the case for volcanogenic derivation: Gold and Money Session and Gold Technical Session, 5th, Pacific Northwest Metals and Minerals Conference, Portland, Oregon, Oregon Department of Geology and Minerals Publication, Proceedings, p. 64–105.

——1993, A multi-stage, multi-process genetic hypothesis for greenstone-hosted gold lodes: Ore Geology Review, v. 8, p. 349–382.

Jonasson, I.R., and Goodfellow, W.D., 1986, Sedimentary and diagenetic textures, and deformation structures within the sulfide zone of the Howards Pass (XY) Zn-Pb deposit, Yukon and Northwest Territories: Canadian Institute of Mining and Metallurgy Special Volume 37, p. 51–70.

Kazakevich, Y.P., 1971, Lena gold-bearing region, stratigraphy, tectonics, magmatism and occurrences of hard rock gold: Moscow, Nedra Press,164 p. (in Russian).

Konnikov, E.G., 1986, Precambrian layered mafic-ultramafic complexes of the Baikal region: Novosibirsk, Nauka Press, 127 p.

Kuz'min, M.I., Yarmolyuk, V.V., Spiridonov, A.I., Nemerov, V.K., Ivanov, A.I., and Mitrofanov, G.L., 2006, Geodynamic setting of gold ore deposits of the Neoproterozoic Bodaibo trough: Doklady Earth Sciences, v. 407A, p. 397–400.

Kribek, B., 1991, Metallogeny, structural, lithological and time controls of ore deposition in anoxic environments: Mineralium Deposita, v. 26, p. 122–131.

Large, R.R., 1992, Australian volcanic-hosted massive sulfide deposits: Features, styles, and genetic models: Economic Geology, v. 87, p. 471–510.

Large, R.R., McGoldrick, P.J., Berry, R.F., and Young, C.H., 1988, A folded, gold-rich massive sulfide deposit: Que River mine, Tasmania. Economic Geology, v. 83, p. 681–693.

Large, R.R., Bull S.W., McGoldrick, P.J., Derrick, G., Carr, G., and Walters, S., 2005, Stratiform and stratabound Zn-Pb-Ag+Cu deposits of the Proterozoic sedimentary basins of northern Australia: Economic Geology 100th Anniversary Volume, p. 931–963.

Larin, A.M., Rytsk, Y.Y., and Sokolov, Y.M., 1997, Baikal-Patom fold belt: Developments in Economic Geology, v. 30, p. 317–362.

Larocque, A.C.L., Hodgson, C.J. and Lafleur, P.J., 1993, Gold distribution in the Mobrun volcanic-associated massive sulfide deposit, Noranda, Quebec: A preliminary evaluation of the role of metamorphic remobilization: Economic Geology, v. 88, p. 1443–1459.

Laverov, N.P., Lishnevskii, E.N., Distler, V.V., and Tchernov, A.A., 2000, Model rudno-magmaticheskoi sistemy zoloto- platinovo-go mestorojdeniya Sukhoi Log, Vostochnaya Sibir, Rossia: Doklady Earth Science, v. 375, p. 652–656 (in Russian).

Laverov, N.P., Chernyshov, I.V., Distler, V.V., Bairova, E.D., Golzman, Y.V., Golubev, V.N., Chugaev, A.V., and Yudovskaya, M.A., 2000b, Geochronology and possible source of the ore matter in the Sukhoi Log deposit: Results of the isotopic studies. Isotopnoye datirovanie geologicheskikh protsessov: novye metody i rezultaty: Moscow Geological Systems (GEOS), p. 211–214 (in Russian).

Longerich, H.P., Jackson, S.E., and Gunther, D., 1996, Laser ablation inductively coupled plasma mass spectrometric transient signal data acquisition and analyte concentration calculation: Journal of Analytical Atomic Spectrometry, v. 11, p. 899–904.

Marshall, B., Vokes, F.M., and Larocque, A.C.L., 2000, Regional metamorphic remobilization: Upgrading and formation of ore deposits: Reviews in Economic Geology, v. 11, p.19–38.

McClay, K.R., 1983a, Structural evolution of the Sullivan orebody, Kimberley, B.C.: Economic Geology, v. 78, p. 1398–1424

——1983b, Deformation of stratiform lead-zinc deposits: Mineralogical Association of Canada Short Course, Victoria, May 1983, v. 8, p. 283–307.

Neymark, L.A., Rytsk, E.Y., Ovchinnikova, G.V., Sergeeva, N.A., Gorokhovsky, B.M., and Skopintsev, V.G., 1995, Lead isotopes in gold deposits of the eastern Sayan, Russia: Geology of Ore Deposits, v. 37, p. 201–212.

Patterson, J.H., Ramsden, A.R., Dale, L.S., and Fardy, J.J., 1986, Geochemistry and mineralogical residences of trace elements in oil shales from Julia Creek, Queensland, Australia: Chemical Geology, v. 55, p. 1–16.

Ramsay, J.G., 1980, The crack-seal mechanism of rock deformation: Nature, v. 284, p. 135–139.

Razvozzhaeva, E.A., Prokof'ev, V.Yu., Spiridonov, A.M., Martikhaev, D.K., and Prokopchuk, S.I., 2002, Precious metals and carbonaceous substances in ores of the Sukhoi Log deposit, Eastern Siberia, Russia: Geology of Ore Deposits, v. 44, p.103–111.

Reich, M., Kesler, S.E., Utsunomiya, S., Palenik, C.S., Chryssoulis, S.L., and Ewing, R., 2005, Solubility of gold in arsenian pyrite: Geochimica et Cosmochimica Acta, v. 69, p. 2781–2796.

Rimmer, S.M., 2004, Geochemical paleoredox indicators in Devonian-Mississippian black shales, Central Appalachian Basin, USA: Chemical Geology, v. 206, p. 373–391.

Savage, K.S., Tingle, T.N., O'Day, P.A., Waychunas, G.A., and Bird, D.K., 2000, Arsenic speciation in pyrite and secondary weathering phases, Mother lode gold district Tuolumne County California: Applied Geochemistry, v. 15, p. 1219–1244.

Scott, R.J., Large, R.R., Meffre S., and Masslenikov, V.V., 2007, Structural controls on the development of the giant Sukhoi Log gold deposit, Siberia: Deformation in the Desert [abs.]: Geological Society of Australia Specialist Group in Tectonics and Structural Geology Conference, Alice Springs, July 2007, Abstract Volume, p. 55.

Smirnov, V.I., 1997, Ore deposits of the USSR: London-San Francisco-Melbourne: Pitman Publishing, v. 2, 424 p.

Taylor, H.P., and McLennan, S.M., 1985, The continental crust: Its composition and evolution: Oxford, Blackwell Publishing, 328 p.

Wagner, T., Klemd, R., Wenzel, T., and Mattsson, B., 2007, Gold upgrading in metamorphosed massive sulfide deposits: Direct evidence from laser-ablation-inductively coupled plasma-mass spectrometry analysis of invisible gold: Geology, v. 35, p. 775–778.

Webster, A.E., 2006, The geology of the Broken Hill lead-zinc-silver deposit, New South Wales, Australia: University of Tasmania CODES Monograph 1, 278 p.

Wood, B.L., and Large R.R., 2007, Syngenetic gold in western Victoria: Occurrence, age and dimensions: Australian Journal of Earth Sciences, v. 54, p. 711–732.

Wood, B.L., and Popov, N.P., 2006, The giant Sukhoi Log deposit, Siberia: Russian Geology and Geophysics, v. 47, p. 315–341.

Wood, S.A., 1996, The role of humic substances in the transport and fixation of metals of economic interest (Au, Pt, Pd, U, V): Ore Geology Reviews, v. 11, p. 1–33.

Yakubchuk, A.S., Shatov, V.V., Kirwin, D., Edwards, A., Tomurtogoo, O., Badarch, G., and Buryak, V.A., 2005, Gold and base metal metallogeny of the central Asian orogenic supercollage: Economic Geology 100th Anniversary Volume, p. 1035–1068.

Zartman, R.E., and Doe, B.P., 1981, Plumbotectonics: The model: Tectonophysics, v. 75, p. 135–162.